Information Efficacy of a Dynamic Synapse

Mehrdad Salmasi

Graduate School of
Systemic Neurosciences
LMU Munich

Dissertation at the
Graduate School of Systemic Neurosciences
Ludwig-Maximilians-Universität München

28th September 2017

Information Efficacy of a Dynamic Synapse

Mehrdad Salmasi

Graduate School of
Systemic Neurosciences
LMU Munich

Dissertation at the
Graduate School of Systemic Neurosciences
Ludwig-Maximilians-Universität München

28th September 2017

First reviewer (supervisor):
Professor Dr. Stefan Glasauer

Second reviewer:
Professor Dr. Thomas Wachtler

Date of submission:
28th September 2017

Date of defense:
19th April 2018

To my parents,

for their unconditional love and endless support.

Acknowledgements

During my PhD, I studied the functional role of synaptic plasticity and learned about the underlying mechanisms of depression and facilitation in synapses. Similar to synapses, humans are affected temporarily or permanently by the surrounding people and dynamic circumstances. Although the underlying mechanisms of synaptic plasticity have not been fully understood yet, I know for sure the great people who facilitated my PhD and assisted me in all the aspects of life.

First and foremost, I wish to thank my supervisor, Professor Dr. Stefan Glasauer, who guided me with his exceptional ideas and remarkable comments. Stefan gave me the freedom to explore the broad field of neuroscience and investigate my favorite topics. He supported my enthusiasm by permitting me to attend all the courses that I liked, ranging from dissecting and recording from leech in the neurophysiology course to profound discussions about the free will and consciousness in the neurophilosophy lectures. He also approved my participation in all of the conferences and workshops that I requested. His generous support helped me to get involved in scientific interactions with the best minds of the field. Stefan introduced me to computational neuroscience, clinical neuroscience, statistical methods and motor control in humans. Stefan's contributions to me go far beyond neuroscience. I have learned from him not only about the relationship between quantum mechanics and perception but also about the best contemporary museums and art performances. He has supported me in every situation and I am forever grateful to him.

I got familiar with synaptic plasticity through a course which was presented by two great scientists, Dr. Martin Stemmler and Dr. Alex Loebel. This course helped me to choose my field of research and more importantly, to find two great collaborators.

I am indebted to Martin for his brilliant ideas, unique scientific perspective, and continuous support. I have been always impressed by his great personality, patience and wisdom. This thesis owes much to Martin and I express my sincere appreciation to him.

My special thanks go to Alex. He is actually the one who suggested the collaboration and I always appreciate him for his great suggestion. I learned a lot from his in-depth comments, valuable remarks, and thorough revisions of the manuscripts and abstracts.

In the beginning of my PhD, I benefited considerably from the guidance of Professor Dr. Ulrich Büttner. He presented to me the spike recordings from the monkeys and trained me to use spike detection and spike sorting algorithms. This training triggered the first ideas about designing a new spike detection algorithm based on the fractal properties of the extracellular signals. I wish to sincerely thank him for his professional advice and constructive feedback.

In addition to Stefan and Martin, I had the great opportunity to learn from two other distinguished professors in my thesis advisory committee, Professor Dr. Thomas Wachtler and Professor Dr. Hans Straka.

Thomas introduced me to the amazing field of vision and taught me about the computational models of visual system. I would like to deeply thank Thomas for his great lectures, valuable remarks on my research, substantial assistance, and outstanding personality.

In theoretical neuroscience, there is always the risk of being drowned in abstract models and losing connection with the real world. In my thesis advisory committee, Hans helped me to remain connected to the experimental side. His in-depth comments contributed remarkably to developing models that were consistent with real synapses. Moreover, I had the privilege to attend his interesting lectures on the vestibular system. Hans has supported me during different phases of my PhD and I am immensely grateful to him for his scientific advice and personal support.

Particularly, I wish to thank my PhD examination committee, Professor Dr. Stefan Glasauer, Professor Dr. Thomas Wachtler, Professor Dr. Andreas Herz, Professor Dr. Benedikt Grothe, and Professor Dr. Anton Sirota, for their constructive feedback and intellectually stimulating discussions.

In the first year of my PhD, I attended a course on modeling of cellular physiology which was instructed by Professor Dr. Andreas Herz. This course was a unique opportunity for me to learn not only about the neuronal models but also about the exceptional teaching skills. Andreas kindly accepted my request for joining his weekly group meetings. I gained a lot from the scientific talks and lively discussions in these meetings. I had several presentations in his group and could enhance my work based on the valuable feedback that I received from him and the other members of the group. In addition to the scientific comments, I benefited from Andreas's precious remarks on presentation techniques and soft skills. I would like to express my sincere gratitude to Andreas for his immense contributions to me, for his continuous support, and for his magnificent standpoint on the scientific practice which is nicely reflected in his ultimate goals for the Bernstein association and the Bernstein conference.

I wish to thank the German Center for Vertigo and Balance Disorders (DSGZ) for offering this research position to me and for generously supporting my participation in different conferences and workshops. Specifically, I appreciate Professor Dr. Thomas Brandt, the director of DSGZ, and his deputies, Professor Dr. Marianne Dieterich, and Professor Dr. Hans Straka, for organizing this great center. Also I want to thank Dr. Andreas Schepermann and Ms. Anita Hauser for managing the scientific events and handling the financial supports.

I had the great privilege to do my PhD in the graduate school of systemic neurosciences (GSN-LMU). The international environment and the intimate atmosphere of GSN welcomed me from the first day and became like a second home for me. I learned a lot from the lectures, practical courses, and soft skill courses that were presented by the best professors of the field. In addition, the Monday evening talks and the Friday noon Neurolunchs were two of the greatest weekly events during my PhD and broadened my neuroscientific horizon. GSN also supported my participation in conferences which helped me to extend my scientific network and improve my research. I am extremely grateful to GSN for providing me with these valuable opportunities.

In GSN, the highest scientific quality has been merged with the most vibrant and dynamic ambiance and this is largely indebted to Professor Dr. Benedikt Grothe. I cannot begin to express the depth of my gratitude to Professor Grothe, for establishing and organizing such an exceptional program, and for his personal support.

My warmest thanks go to Ms. Lena Bittl, the head of administration, who always made time to help and support me in every single way, even before my enrollment in GSN. Also I wish to thank Dr. Julia Brenndörfer and Ms. Birgit Reinbold, the previous and the current head of examination office, who assisted me with my study regulations.

GSN organizes many interesting social and scientific events which need considerable planning and organization. I would like to thank Ms. Maj-Catherine Botheroyd-Hobohm who tirelessly organizes all of the GSN events. Also, I would like to thank Professor Dr. Oliver Behrend, Dr. Alexander Kaiser, Ms. Nadine Hamze, Ms. Stefanie Bosse, Ms. Renate Herzog and the other GSN faculty members and GSN staff for creating such a phenomenal program.

During my PhD, I benefited remarkably from valuable discussions with my colleagues and the other great scientists that I met in different conferences and workshops. I very much want to thank all of them for their intellectual contributions.

Although we try to measure everything in science, the depth of the love of my parents is not measurable. They sacrificed their own personal life and happiness so that I could be happy and successful. Being away from them was the most difficult experience of my life, but their love embraced me beyond the boundaries and nourished my soul. I am eternally grateful to my parents for their love and support. Also, I would like to express my gratitude to my brother, my sister and all my relatives for their moral support and continuous encouragement throughout my life.

Finally, I wish to thank all of my friends for helping me in every possible way and for bringing so much joy and humor to my life. Specially, I am forever grateful to a unique friend, Ehsan, whom I met eight months after my birth. He supported me in every moment until he passed away a few months ago. I miss his exceptional personality, brilliant sense of humor, and constant presence, but his memory is treasured in my mind and lives on.

Abstract

Information transmission in the brain is mediated mainly through chemical synapses. The arrival of an action potential at a chemical synapse triggers a sequence of events that leads to the release of a vesicle. The released neurotransmitter molecules open the ion channels on the postsynaptic site and create an excitatory or inhibitory postsynaptic potential.

An incoming action potential does not always elicit a vesicular release. The evoked release probability varies widely among synapses. While the reliable synapses show a release probability close to one, the release probability of an unreliable synapse may be lower than one tenth. Additionally, a synapse sometimes releases spontaneously even in the absence of an action potential. Synaptic unreliability and spontaneous release can significantly alter the information transmission through the synapse. Synaptic plasticity also changes the strength of synaptic connections over a wide range of time scales. In short-term depression, the successive release of vesicles reduces the release probability of the synapse. The functional role of short-term depression in filtering and decorrelation of the presynaptic spike train has been shown in several studies. In this thesis, we investigate the function of short-term depression in modulating the rate of information transmission through the synapse.

We model a synaptic release site by a communication channel, capturing the spike-evoked and spontaneous release of the synapse. The input of the channel is the presynaptic spike train and the output is the elicited postsynaptic potential. To incorporate short-term depression into the synapse model, the state of the channel is switched between a normal state and a used state. After each release, the synapse goes to the used state and the release probabilities of the channel reduce; the synapse recovers back to the normal state in the absence of release. Information theory is then employed to calculate the rate of information that is transferred from the presynaptic spike train to the postsynaptic potential.

Synaptic release is energetically expensive and a neuron needs to compromise between its information efficacy and energy consumption. We consider the energetic cost of the release and calculate the energy-normalized information rate of the synapse. This measure is used to evaluate the rate of information transmission for a given energy budget. We show that the functional role of short-term depression in modulating the information transmission depends on the relative level of depression for spontaneous and spike-evoked releases. If the depression affects spike-evoked

and spontaneous release equally, then the information rate and energy-normalized information rate of the synapse both decrease. However, if spontaneous release is depressed more than spike-evoked release, then short-term depression can enhance the information efficacy of the synapse.

In the two-state model of depression, the synapse transits sharply between the used state and the normal state. To emulate the gradual depression and exponential recovery of short-term depression, the two-state model is extended to a communication channel with a memory of the release history. The content of the memory specifies the release probabilities of the channel based on the dynamics of short-term depression. We calculate the information efficacy of the synapse model and determine the regime of synaptic parameters in which short-term depression enhances/decreases the mutual information rate and energy-normalized information rate of the synapse. Our analysis shows how short-term depression governs the trade-off between the energy expenditure and information rate of the synapse.

Contents

1 Introduction **1**

- 1.1 Synaptic transmission . . . 2
- 1.2 Synaptic plasticity . . . 4
- 1.3 Short-term depression . . . 5
  - 1.3.1 Depletion of vesicles . . . 5
  - 1.3.2 Inactivation of release sites . . . 5
  - 1.3.3 Reduction of presynaptic calcium influx . . . 6
  - 1.3.4 Desensitization of receptors . . . 6
  - 1.3.5 Release-independent depression . . . 6
- 1.4 Functional roles of short-term depression . . . 7
  - 1.4.1 Temporal filtering . . . 7
  - 1.4.2 Decorrelation . . . 8
  - 1.4.3 Adaptation to identical stimuli . . . 8
  - 1.4.4 Regulation of information transfer . . . 9
- 1.5 Information-theoretic measures . . . 10
  - 1.5.1 Entropy of a random variable . . . 10
  - 1.5.2 Conditional entropy . . . 11
  - 1.5.3 Mutual information between two random variables . . . 12
  - 1.5.4 Entropy rate of a random process . . . 12
  - 1.5.5 Mutual information rate between two random processes . . . 13
- 1.6 Synaptic information efficacy . . . 14
- 1.7 Aims of the thesis . . . 15
  - 1.7.1 Modeling of a depressing synapse . . . 15
  - 1.7.2 Analysis of synaptic information efficacy . . . 16
  - 1.7.3 Spike detection . . . 19
  - 1.7.4 Structure of the thesis . . . 19

2 Information rate of the two-state model of depression 21
2.1 Summary 21
2.2 Contributions 21

3 Information efficacy of a depressing synapse 56
3.1 Summary 56
3.2 Contributions 56

4 Spike detection using fractal dimension 82
4.1 Summary 82
4.2 Contributions 83

5 Discussion 103
5.1 Linearity of mutual information rate 104
5.2 Towards synaptic information efficacy 105
5.3 Information efficacy and energy consumption 107
5.4 Spontaneous release 108
5.5 Interpretation of mutual information 108
5.6 Input spike correlations 110
5.7 Multiple release sites 111
5.8 Information rate between two neurons 112
5.9 Complexity of synaptic transmission 113
  5.9.1 Presynaptic terminal 114
  5.9.2 Synaptic cleft 115
  5.9.3 Postsynaptic site 115
5.10 Conclusion 116

Bibliography 117

Chapter 1

Introduction

The functionality of the brain relies on the communication between the neurons. The neuronal communication is mediated by two types of synapses, chemical synapses and electrical synapses. In electrical synapses, the membranes of the two neurons are located very close to each other and some membrane specializations (gap junctions) connect the intracellular regions of the presynaptic and postsynaptic neurons. The potential difference between the two neurons generates an ionic current through the gap junctions and changes the membrane potential of the postsynaptic neuron.

Electrical synapses are bidirectional and the current can flow in both directions. The direct connection between the neurons provides an instantaneous form of communication and permits the electrical synapses to synchronize activity in neuronal populations (Purves et al., 2012). The gap junctions are, however, passive communication channels and the signal is attenuated after each transmission.

In chemical synapses, there is a gap of 20-40 nm between the membranes of the two neurons, and communication is realized through the release of neurotransmitters. The presynaptic neuron releases packets of neurotransmitter into the synaptic cleft. The neurotransmitter molecules open the receptors on the postsynaptic neuron and a synaptic current is generated. In contrast to the electrical synapses, the communication in chemical synapses is unidirectional and has a delay from 0.3 ms to 5 ms (Kandel et al., 2000). Although chemical synapses introduce a delay in signal transmission, they can amplify the signals. One vesicle contains several thousands molecules of neurotransmitter and opens hundreds of receptors on the postsynaptic site. For example, a single action potential in a motor neuron is enough to trigger muscle contraction in several muscle cells (Lodish et al., 1995). The other advantage of a chemical synapse over an electrical synapse is its functional diversity which is achieved by more than 100 types of neurotransmitters and their corresponding re-

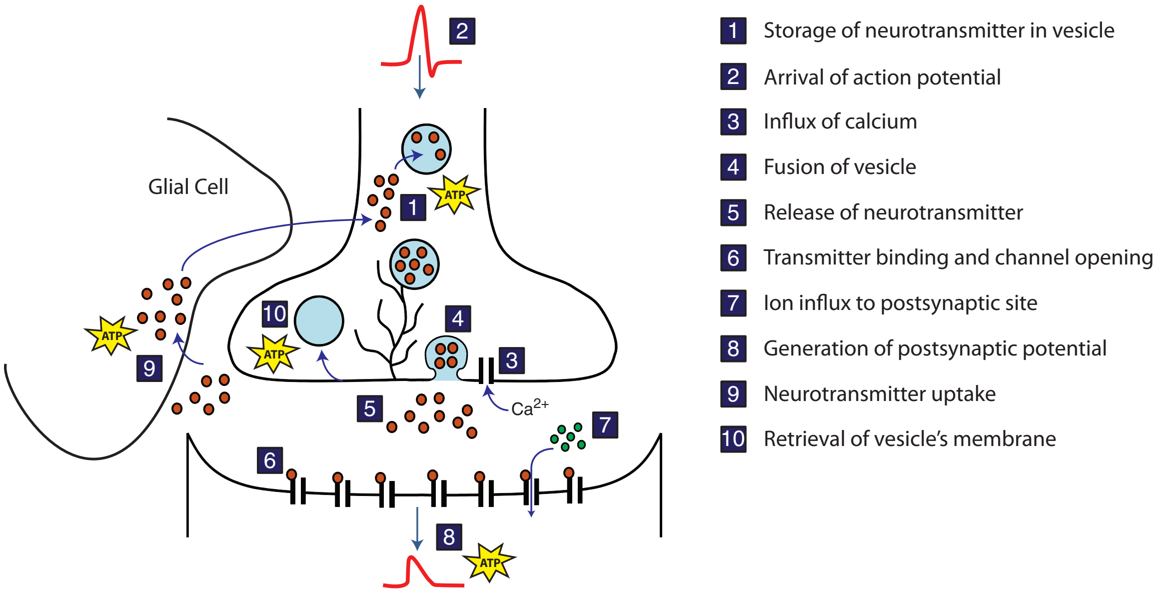

Figure 1.1: Synaptic transmission in a chemical synapse, depicted in ten steps. The presynaptic action potential creates a series of events which leads to the generation of the postsynaptic potential. The ATP symbol shows the energy consumption during synaptic transmission.

ceptors. Chemical synapses modulate the neuronal communications and enhance the computational capacity of the neurons.

The efficacy of chemical synapses in signal transmission highly affects the performance of the brain. In this thesis, we will study how synaptic plasticity changes the information efficacy of the synapse. We first give an overview of the synaptic transmission and different forms of synaptic plasticity. Then we focus on short-term depression and describe its mechanisms and functional roles. We introduce the notions of entropy and mutual information and define synaptic information efficacy using information-theoretic measures. Finally, we present the aims of this thesis and briefly explain our approach towards the analysis of synaptic information efficacy of a dynamic synapse.

1.1 Synaptic transmission

A chemical synapse converts the spiking activity of the presynaptic neuron to the postsynaptic potential. The conversion process can be explained in 10 steps (Fig. 1.1) (Purves et al., 2012):

1- Neurotransmitter molecules are stored inside the vesicles. Synaptic vesicles are clustered around the active zones of the presynaptic nerve terminal. Active zones are specialized parts of the membrane that facilitate docking and fusion of the vesicles. Each active zone is aligned with the receptors on the postsynaptic site (Zhai and Bellen, 2004).

2- Action potential arrives at the presynaptic terminal and changes the membrane potential.

3- The voltage change in the presynaptic membrane opens the voltage-gated calcium channels. The intracellular concentration of the calcium ion in the presynaptic terminal is in the order of $10^{-7}M$ and the extracellular concentration is in the order of $10^{-3}M$. The opening of the calcium channels together with the concentration gradient generates a calcium influx and increases the intracellular concentration of the calcium.

4- The increased concentration of calcium leads to the fusion of the vesicles to the membrane. The fusion machinery of the vesicle is mainly governed by the SNARE complex which brings the vesicle and cell membrane together and initiates the fusion (Rizo and Rosenmund, 2008).

5- The neurotransmitter content of the vesicle is released in the synaptic cleft and initially, generates a concentration peak at the location of the release. The neurotransmitter molecules diffuse in the narrow cleft and the concentration decays rapidly.

6- The neurotransmitter molecules bind the receptors on the postsynaptic site. Brain uses a wide variety of neurotransmitters and receptors to maintain different modes of synaptic signaling. The binding of the neurotransmitter opens the ion channels and changes the conductivity of the membrane.

7- A certain types of ions pass through the opened channels and generate a postsynaptic current. The direction and the amplitude of the postsynaptic current is determined by the type of the passing ions, the concentration gradient of the ions, and the number of opened channels.

8- The postsynaptic current generates a postsynaptic potential and changes the excitability of the postsynaptic neuron.

9- The transporters in the glial cells and the neuronal membrane remove the neurotransmitters from the synaptic cleft. Alternatively, some neurotransmitters are inactivated through enzymatic degradation.

10- The membrane of the vesicle is regenerated and the vesicle is prepared for the next round of neurotransmitter refilling.

The sequence of events in Fig. 1.1 depicts a simplified version of synaptic transmission in a chemical synapse. To understand the synaptic transmission in its full complexity, all the molecular structures and the dynamics of the release machinery should be taken into account.

1.2 Synaptic plasticity

Characteristics of a chemical synapse change dynamically in response to the cellular activity. Synaptic plasticity has been observed in different time scales and is classified into two categories, short-term and long-term plasticity. In the long-term plasticity, the strength of the synaptic connection changes in a time scale of 30 minutes or longer (Purves et al., 2012). Some patterns of activity induce a long-lasting increase in the synaptic strength which is referred to as long-term potentiation (LTP). On the other hand, in long-term depression (LTD), the neuronal activity causes a durable reduction of the synaptic transmission. Long-term plasticity is considered as one of the key cellular correlates of memory formation and learning. The underlying mechanisms for long-term plasticity are modifications of the proteins and changes in the gene expression.

The time scale of short-term plasticity is a few minutes or less. In short-term facilitation, the postsynaptic potential gradually increases in response to a sequence of action potentials (Zucker and Regehr, 2002). Paired-pulse stimulation is used to measure the level of facilitation in synapses. It has been shown that the amplitude of the postsynaptic potential corresponding to the second action potential can be five times larger than the response to the first spike. The time course of the short-term facilitation is hundreds of milliseconds and is usually modeled by an exponential function. Experimental data suggest the role of the presynaptic calcium in the emergence of short-term facilitation. Repeated stimulation increases the concentration of the presynaptic calcium and augments the number of transmitter quanta that is released by an incoming action potential (Zucker and Regehr, 2002).

Short-term depression is another form of short-term plasticity which is a common phenomenon among synapses. In short-term depression, the elevated synaptic activity weakens the synaptic strength and reduces the postsynaptic potential. The underlying mechanisms and functional roles of the short-term depression are discussed in the next sections.

1.3 Short-term depression

The release probability of a synapse is decreased during short-term depression and recovers back to normal with a time constant that varies among synapses from hundreds of milliseconds to tens of seconds. Several mechanisms have been suggested for short-term depression. Here we briefly explain three presynaptic and one postsynaptic mechanism that contribute to short-term depression in many synapses (Fioravante and Regehr, 2011).

1.3.1 Depletion of vesicles

The size of the readily releasable pool of vesicles and the release probability of the vesicles determine the number of vesicles that are released in response to an action potential. When the readily releasable pool shrinks, the number of released vesicles reduces and short-term depression occurs.

Depletion models of short-term depression are used to predict the time course of the post-synaptic potential (Zucker and Regehr, 2002). In the simplest form, it is assumed that the number of releasable vesicles is S and by each action potential, a fraction F of the releasable vesicles are released. If each released vesicle generates a postsynaptic current I, then the total current at the postsynaptic neuron will be SFI. After the first release event, the number of releasable vesicles is reduced to $S(1-F)$. If the second action potential arrives within a short time after the first action potential, the postsynaptic current will be $S(1-F)FI$. The depression level between the two successive release events is then $(1-F)$. The model predicts a higher depression for synapses in which the initial release probability, F, is higher. This prediction is consistent with the data obtained from synapses in the auditory brainstem and corticothalamic synapses (Fioravante and Regehr, 2011).

1.3.2 Inactivation of release sites

The other mechanism for short-term depression is based on the dynamics of the release sites. The fusion of a vesicle changes the properties of a release site and interrupts the release process for hundreds of milliseconds. When the endocytosis is blocked at the presynaptic site, the depression effect is increased. Moreover, by cleaning the membrane from vesicular proteins, the synapse recovers faster from short-term depression (Hosoi et al., 2009). These observations suggest that the inactivation interval of the release site corresponds to the time that is required for cleaning vesicular membrane proteins that are responsible for vesicle fusion (Fioravante and Regehr, 2011).

1.3.3 Reduction of presynaptic calcium influx

Calcium plays a critical role in regulating the release machinery. Slight changes in the intracellular calcium concentration can significantly alter the dynamics of synaptic plasticity (Neher and Sakaba, 2008). A reduction of the calcium influx leads to short-term depression in the calyx of Held (Xu and Wu, 2005). Furthermore, by elevating the presynaptic concentration of the calcium in the climbing fiber synapse, the time constant of the recovery from short-term depression drops to less than 100 ms (Zucker and Regehr, 2002). These findings suggest that by incorporating the dynamics of calcium channels into the depletion models of short-term depression, more realistic models will be developed.

1.3.4 Desensitization of receptors

In addition to the presynaptic mechanisms, desensitization of the postsynaptic receptors contributes to short-term depression (Zucker and Regehr, 2002). When the neurotransmitter molecules bind to the ionotropic receptors (ligand-gated ion channels), the channels open and let the ions pass through the membrane. If the exposure of the ligand-gated channels to the agonist is prolonged, then the receptors enter a refractory period and stop responding to the released neurotransmitter (Kandel et al., 2000). This state of non-responsiveness is called desensitization and takes from tends of milliseconds to minutes. Desensitization reduces the postsynaptic potential and is considered as one of the major causes of short-term depression in several synapses (Zucker and Regehr, 2002).

1.3.5 Release-independent depression

In short-term depression, the release probability of the synapse reduces after successive releases. It has been shown that the release probability of the synapse may reduce even if a presynaptic action potential does not lead to a release (Thomson and Bannister, 1999; Brody and Yue, 2000). Since this type of depression does not depend on the release outcome of the synapse, it is called release-independent depression. Rapid inactivation of the calcium channels has been proposed as a potential mechanism underlying release-independent depression (Thomson and Bannister, 1999). Stochastic fluctuations in the release machinery can also cause release-independent depression in some synapses (Volynski et al., 2006).

1.4 Functional roles of short-term depression

Short-term depression alters the activity pattern of the postsynaptic neuron by reducing the strength of synaptic connections. Several hypotheses have been suggested for the functional role of short-term depression and here, we will review some of them (Abbott and Regehr, 2004).

1.4.1 Temporal filtering

A synapse filters the signals by converting the presynaptic spike train to the postsynaptic potential. Short-term depression can widely alter the filtering characteristics of the synapse (Abbott and Regehr, 2004).

Sensory neurons in the cortex behave as a low-pass filter for the input stimulus. The neurons respond strongly to low-frequency stimuli and generate a very weak signal (if any) in response to high-frequency stimulation (Fortune and Rose, 2001). Computational models show that short-term depression operates as a low-pass filter in neuronal information pathway (Izhikevich et al., 2003).

The low-pass filtering characteristic of short-term depression has been challenged in several studies (Lindner et al., 2009; Merkel and Lindner, 2010). In (Lindner et al., 2009), the filter response of the synapse is studied under natural conditions. The asynchronous activity of the presynaptic neuronal population generates voltage fluctuations in the membrane of the postsynaptic neuron. Coherence analysis is used to measure the power transfer from a rate-modulated input spike process to the postsynaptic conductance. The results show that the information transmission through a depressing synapse is frequency-independent, provided that the postsynaptic fluctuations are considered in the analysis. It is concluded that short-term depression acts as a broadband filter on natural presynaptic inputs.

Debate continues about the filtering response of a depressing synapse. The probabilistic nature of synaptic plasticity, such as random recovery time constant, shapes the filter response of short-term depression (Rosenbaum et al., 2012). The coherence between the presynaptic spike train and the postsynaptic conductance is calculated for a depressing synapse with random recovery time constant. In the absence of stochastic properties of release dynamics, coherence is a constant function which is consistent with the results in (Lindner et al., 2009). However, when the stochastic dynamics are added to the synaptic model, short-term depression creates a high-pass coherence profile. The coherence analysis suggests that a depressing synapse transfers the power of a fast-varying signal with higher fidelity than the power of a signal with low frequencies (Rosenbaum et al., 2012).

1.4.2 Decorrelation

Autocorrelation analysis of intracellular recordings reveals a temporal correlation in the order of hundreds of milliseconds (Dan et al., 1996; Baddeley et al., 1997). The correlation in the spiking activity of a neuron indicates that the neuron carries redundant information. Short-term depression and synaptic failures provide neurons with mechanisms to filter out the redundant information from their inputs. To study the performance of short-term depression in decorrelating spike trains, three categories of correlated processes have been analyzed (Goldman et al., 2002):

1- Spike train of a visual neuron during saccadic eye movements: The spikes are generated by a piecewise homogeneous Poisson process. The neuron generates a Poisson spike train with a fixed rate until a saccade occurs. Then a new rate is assigned to the Poisson process and the neuron's spiking activity is updated.

2- Spike train of bursting neurons: The data is generated by fitting a neuronal model to the data collected from MT neurons in monkeys during visual discrimination task.

3- Experimental spike trains recorded from V1 area of the monkeys viewing natural scenes.

It is shown that short-term depression reduces the redundancy of information in all the three categories of correlated spike trains. By decorrelating the input signal, short-term depression also reduces the number of releases and economizes on the neuronal resources that are used for vesicle release.

Two processes contribute to the correlation in the spiking activity of a neuron: the autocorrelation of the presynaptic spike train, and the cross correlation among the synaptic inputs. Although short-term depression reduces the autocorrelation caused by individual synapses, it can not remove the cross correlation of the presynaptic input processes. Consequently, some correlation remains in the spiking activity of the postsynaptic neuron.

1.4.3 Adaptation to identical stimuli

Many cortical neurons show a reduced responsiveness (adaptation) to sensory stimuli (Ulanovsky et al., 2004; Kohn, 2007; Abolafia et al., 2010; Clifford et al., 2007; Müller et al., 1999). The underlying neuronal mechanism of sensory adaptation has not been fully understood yet. However, it has been shown in the models of V1 neurons that short-term depression can cause adaptation in the response of the neurons to the sensory stimuli (Todorov et al., 1997; Chance et al., 1998). The functional role of short-term depression in adaptation has been also studied in vivo recordings (Chung et al., 2002). A rat's whisker is stimulated and the neurons in the rat's barrel cortex are recorded. Neuronal responses adapt to the repeated stimulation very fast and the recovery time course of adaptation matches the recovery from short-term depression in thalamocortical synapses. It is concluded that shot-term depression in thalamocortical synapses is one of the major causes of sensory adaptations in the cortical neurons (Chung et al., 2002).

1.4.4 Regulation of information transfer

In a static synapse, the release characteristics remain constant over time and the postsynaptic potential does not carry any information about the previous activity of the presynaptic neuron. Many synapses, however, show a wide range of short-term and log-term dynamics. The release characteristics of a dynamic synapse are affected by the activity history of the presynaptic and postsynaptic processes. For example, the release probability of a depressing synapse depends on the timing of the previous release events.

Short-term depression can be considered as a memory for the synapse, regulating the release machinery based on the synaptic release history (Fuhrmann et al., 2002). The postsynaptic neuron can potentially use this intrinsic memory to extract some information about the history of the spiking activity of the presynaptic neuron. Since the flow of information is controlled by the content of this memory, it has been suggested that short-term depression may modulate information efficacy of the synapse.

Synaptic information efficacy is a functional measure for analyzing the information transmission through a synapse. It is defined by information-theoretic measures and provides a mathematical description for the performance of the synapse. In this thesis, we use synaptic information efficacy to study the functional role of short-term depression in modulating the rate of information transfer. First the basic concepts of information theory are reviewed in the next section, and then the definition of synaptic information efficacy is presented.

1.5 Information-theoretic measures

Information theory was founded by Claude E. Shannon to address two major questions in communication theory: the minimum compression rate of the data and the maximum transmission rate over a communication channel (Shannon, 1948). The applications of information theory are not limited to communication systems. The powerful framework of information theory and Shannon's concepts of entropy and mutual information are used in many fields, such as statistics, computer science, physics, economics, and physiology (Cover and Thomas, 2012).

1.5.1 Entropy of a random variable

The definition and quantification of information is at the heart of information theory. Shannon used the term *entropy* to refer to the information content of a random variable. Entropy is measured in bits and quantifies the amount of uncertainty about the value of a random variable. When a fair coin is tossed, the probability of heads or tails is 0.5 each and the amount of uncertainty about the outcome of the coin (entropy) is equal to 1 bit. For an irregular coin that always lands heads up, there is no uncertainty about the tossing outcome and the entropy is zero.

Another example would be a guessing game in which one object is selected from a bag containing eight distinct objects (Fig. 1.2A) and a participant tries to find the object with the minimum number of yes/no questions. In Fig. 1.2B, a strategy is proposed for finding the object with 3 yes/no questions. It can be shown that on average, the minimum number of yes/no questions needed for finding the object is equal to 3. Therefore, the entropy of the bag in Fig. 1.2A is equal to 3 bits.

These examples can be generalized to define the entropy of a random variable. Let X be a discrete random variable with the sample space S_X. The entropy of X is defined by

$$H(X) = -\sum_{x \in S_X} P(X = x) \log_2 P(X = x), \tag{1.1}$$

where $P(.)$ is the probability measure.

The content of the bag in Fig. 1.2A corresponds to the sample space of a random variable X with 8 elements, i.e., $S_X = \{1, 2, ..., 8\}$. Since the objects are selected randomly with uniform distribution, the probability distribution of the random variable is $P(X = x) = \frac{1}{8}$, $1 \leq x \leq 8$. Using these probability values in (1.1), the entropy of X is $H(X) = 3$ bits which is equal to the minimum number of yes/no questions.

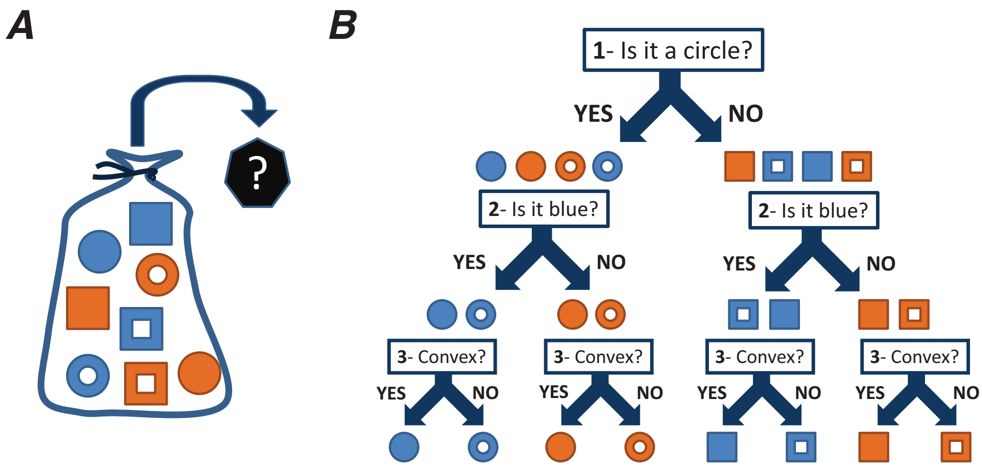

Figure 1.2: Entropy of data. (A) A bag of eight different objects. The examiner selects one object randomly and the participant should guess the object with the minimum number of yes/no questions. (B) An optimal strategy for asking the yes/no questions.

The definition of entropy can be extended to two or more random variables. The entropy of two random variables X and Y is defined by

$$H(X,Y) = -\sum_{(x,y)\in S_X \times S_Y} P(X=x, Y=y) \log_2 P(X=x, Y=y), \qquad (1.2)$$

where $P(X=x, Y=y)$ represents the joint probability distribution of X and Y.

1.5.2 Conditional entropy

The amount of uncertainty about a source can be reduced if some side information is given. For example, if we know that the color of the selected object in Fig. 1.2 is orange, then the number of yes/no questions that are needed for finding the object reduces to 2 questions. The amount of uncertainty about the content of the bag, given the color of the object is the *conditional entropy* of the bag and is equal to 2 bits.

The conditional entropy of a random variable X given another random variable Y is denoted by $H(X|Y)$ and is defined by

$$H(X|Y) = -\sum_{y\in S_Y} P(Y=y) \sum_{x\in S_X} P(X=x|Y=y) \log_2 P(X=x|Y=y). \qquad (1.3)$$

The function $H(X|Y)$ quantifies the uncertainty about the value of the random variable X provided that the value of Y is given.

1.5.3 Mutual information between two random variables

We showed that the uncertainty about the selected object in Fig. 1.2 is 3 bits and the uncertainty is reduced to 2 bits if the color of the object is given. Therefore, the color of the object gives 1 bit of information about the object. In information-theoretic terms, we say that the *mutual information* between the objects of the bag and the color of the objects is 1 bit.

The mutual information between two random variables X and Y is denoted by $I(X;Y)$ and is defined by

$$I(X;Y) = H(X) - H(X|Y). \tag{1.4}$$

Mutual information quantifies the amount of information that one random variable Y gives about the other random variable X. In other words, $I(X;Y)$ determines how much the uncertainty of X is reduced if the value of Y is known.

1.5.4 Entropy rate of a random process

Random processes are used to model a wide variety of signals, such as EEG recordings, fMRI BOLD signals, calcium recordings, spiking activity, and behavioral data. To quantify the information content of these signals, the notion of entropy should be extended to random processes.

Let $X = \{X_i\}_{i=1}^{\infty}$ be a discrete-time random process, where X_i is the random variable corresponding to the value of X at time i. The entropy rate of the random process X is defined by

$$H(X) = \lim_{n\to\infty} \frac{1}{n} H(X_1, X_2, ..., X_n), \tag{1.5}$$

provided that the limit exists.

For example, a fair coin is tossed infinite times and its value at time i is assigned to a binary random variable X_i. Since the random process $X = \{X_i\}_{i=0}^{\infty}$ is independent and identically distributed,

$$H(X_1, X_2, ..., X_n) = nH(X_1), \tag{1.6}$$

and hence, $H(X) = H(X_1) = 1$ bit.

An example of a correlated process is the weather changes (Zucchini et al., 2016). Assume that the weather has two possible states, rainy or sunny. If today is sunny, then with a probability of α, tomorrow will be rainy, and if today is rainy, then the probability of having a sunny day tomorrow is β (Fig. 1.3A). Since the state of the

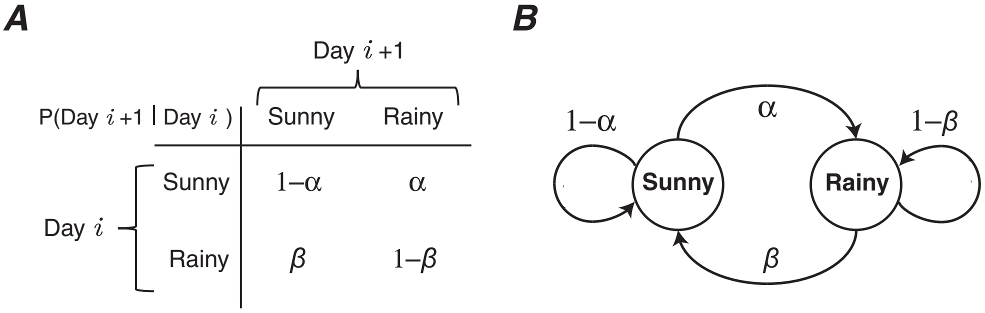

Figure 1.3: Weather changes modeled by a correlated random process. (A) Two states are assumed for the weather (rainy or sunny) and the probability of having a rainy or sunny day on day $i+1$ is determined based on the state of the weather on day i. (B) A two-state Markov chain used to model weather changes.

weather on day $i+1$ depends only on the weather on day i, the weather process can be modeled by a Markov chain with two states (Fig. 1.3B). The entropy rate of the weather process is derived from (Cover and Thomas, 2012),

$$H(X) = \frac{\beta}{\alpha+\beta} h(\alpha) + \frac{\alpha}{\alpha+\beta} h(\beta), \tag{1.7}$$

where $h(x) = -x\log_2(x) - (1-x)\log_2(1-x)$.

For $\alpha = \beta = 0.3$, our uncertainly about the weather is $H(X) = 0.88$ bits. If there was not any dependency between the state of the weather in successive days, the uncertainty about the weather would be 1 bit. However, the correlation between the days reduces the uncertainty to 0.88 bits.

1.5.5 Mutual information rate between two random processes

The interactions between the parts of a system have been studied using information-theoretic measures. Mutual information quantifies the amount of information that can be obtained from the activity of one part of the system about the activity of the other part(s). For example, in a population of neurons, the spiking activity of one neuron may be informative about the spiking process of another neuron. To measure neuronal interactions, the mutual information between the spiking processes of the two neurons are calculated.

The mutual information between two random processes is defined using a similar approach to the entropy of a random process (Vembu et al., 1995). Let $X = \{X_i\}_{i=1}^{\infty}$ and $Y = \{Y_i\}_{i=1}^{\infty}$ be two discrete-time random processes. The mutual information rate between X and Y is defined by

$$I(X;Y) = \lim_{n\to\infty} \frac{1}{n}\Big(H(X_1, X_2, ..., X_n) - H(X_1, X_2, ..., X_n|Y_1, Y_2, ..., Y_n)\Big), \tag{1.8}$$

if the limit exists.

The mutual information is used as a similarity measure between the two random processes. Although the cross correlation function also quantifies the similarity between the two signals, it can not extract the non-linear correlations. Mutual information can be considered as an extension of the cross correlation function which quantifies the linear and non-linear similarities of the two signals by calculating the amount of information that one signal carries about the other one.

Mutual information is a powerful tool for analyzing neural systems (Borst and Theunissen, 1999; Quiroga and Panzeri, 2009; Dimitrov et al., 2011; Brunel and Nadal, 1998; van Steveninck et al., 1997). It is used to evaluate information transmission over a wide range of spatial scales, from connectivity analysis in fMRI BOLD signals (Rubinov and Sporns, 2010) to information coding in single-cell recordings (Nirenberg et al., 2001; Reich et al., 2001; Brostek et al., 2011).

1.6 Synaptic information efficacy

Synapses are the communication channels between the neurons and convert the presynaptic spikes to the postsynaptic potential. Synaptic information efficacy (SIE) is a measure for quantifying the amount of information that is transferred through a synapse and is defined as the mutual information rate between the presynaptic input spike train, X, and the postsynaptic potential, Y (Fig. 1.4) (London et al., 2002). The definition of SIE can be also extended to include all the synapses between the two neurons. Synaptic information efficacy between the two neurons is the mutual information between the presynaptic spike process, X, and the postsynaptic spike train, Z (Fig. 1.5).

Synpatic information efficacy has been used to evaluate the transmission performance of the neurons under different experimental conditions. The spiking activities of the presynaptic neuron(s) and the postsynaptic neuron are recorded and mutual information between the spike trains is calculated by numerical methods (London et al., 2002; Arleo et al., 2010; Gourévitch and Eggermont, 2007; Brochini et al., 2011). Computational models of synaptic transmission are also used to estimate synaptic information efficacy. The presynaptic spike process, synaptic transmission, and the postsynaptic neuron are modeled and synaptic information efficacy is estimated numerically (London et al., 2002; Scott et al., 2012) or analytically (Goldman, 2004; Fuhrmann et al., 2002).

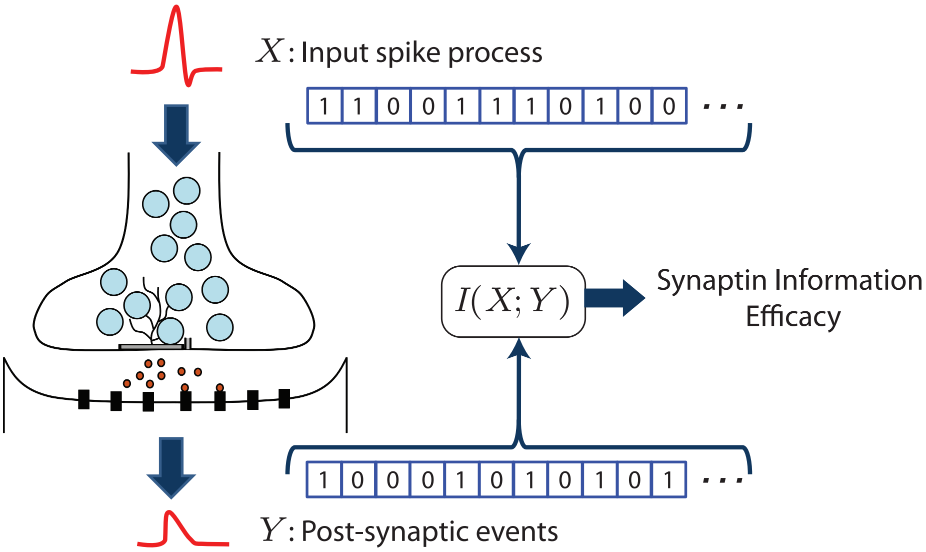

Figure 1.4: Synaptic information efficacy of a single synapse. The spiking activity of the presynaptic neuron is modeled by a binary process X. Each vesicle release generates a miniature postsynaptic potential which is modeled by a binary process Y. Synaptic information efficacy is then defined as the mutual information between the presynaptic input spike process, X, and the postsynaptic process, Y.

1.7 Aims of the thesis

Short-term depression reduces the responsiveness of the synapse to the incoming action potentials. The release probability of the synapse and the number of released vesicles decrease and consequently, the amplitude of the postsynaptic potential drops. There is not a direct relationship between the postsynaptic potential and the information rate of the synapse. In this thesis, we investigate how the reduction of synaptic strength during short-term depression alters synaptic information efficacy. We first present a phenomenological model for a depressing synapse and then use information-theoretic analysis to study the impact of short-term depression on the information efficacy of the model synapse.

1.7.1 Modeling of a depressing synapse

Synapses mediate information transmission between the neurons and can be modeled by communication channels (Levy and Baxter, 2002). A communication channel is a mathematical model for signal transmission from a sender to a receiver and describes the relationship between the transmitted and received signals (Gallager, 1968).

We model a static release site by a binary asymmetric channel (Fig. 1.6A). In this model, the input is the presynaptic input spike process and the output is a binary

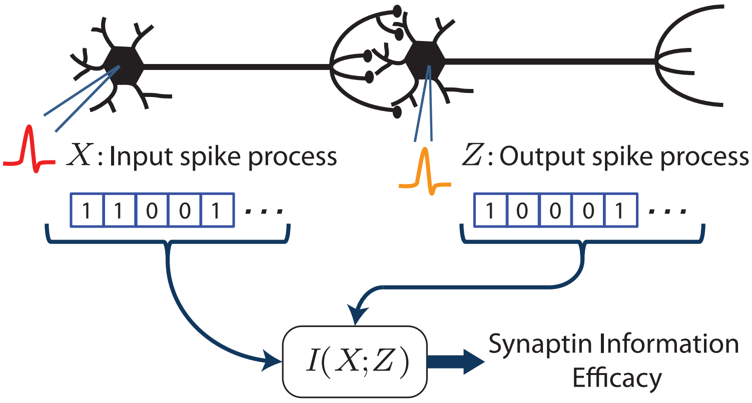

Figure 1.5: Synaptic information efficacy of multiple synapses. The spiking activity of the presynaptic neuron, X, and the postsynaptic neuron, Z, are derived and the mutual information is calculated between X and Z.

process corresponding to the presence or absence of the postsynaptic potential. This simple model captures the two release mechanisms of the synapse, spike-evoked release and spontaneous release. The release probabilities of a static synapse do not depend on the release history of the synapse and are constant over time (Fig. 1.6B).

Short-term depression creates a memory for the synapse by making the release process dependent on the previous activity of the synapse. We, therefore, model short-term depression by a binary asymmetric channel with memory (Fig. 1.7A). The memory of the communication channel stores the release outcomes of the synapse and determines the release probability of the synapse based on the synaptic release history profile.

The binary asymmetric channel with memory captures the dynamics of the release probability during short-term depression. The spike-evoked release probability reduces after each release and recovers back to its initial value exponentially (Fig. 1.7B). There is not yet enough experimental data to verify whether spontaneous release has a depression profile similar to the evoked release (solid blue line in Fig. 1.7B) or remains constant during short-term depression (dashed blue line in Fig. 1.7B) (Zucker and Regehr, 2002).

1.7.2 Analysis of synaptic information efficacy

The information efficacy of a synapse is measured by the mutual information between the presynaptic input spike train and the postsynaptic potential. This measure quantifies the amount of information that is transferred through the synapse. There are, however, several other performance measures that are essential in analyzing neuronal

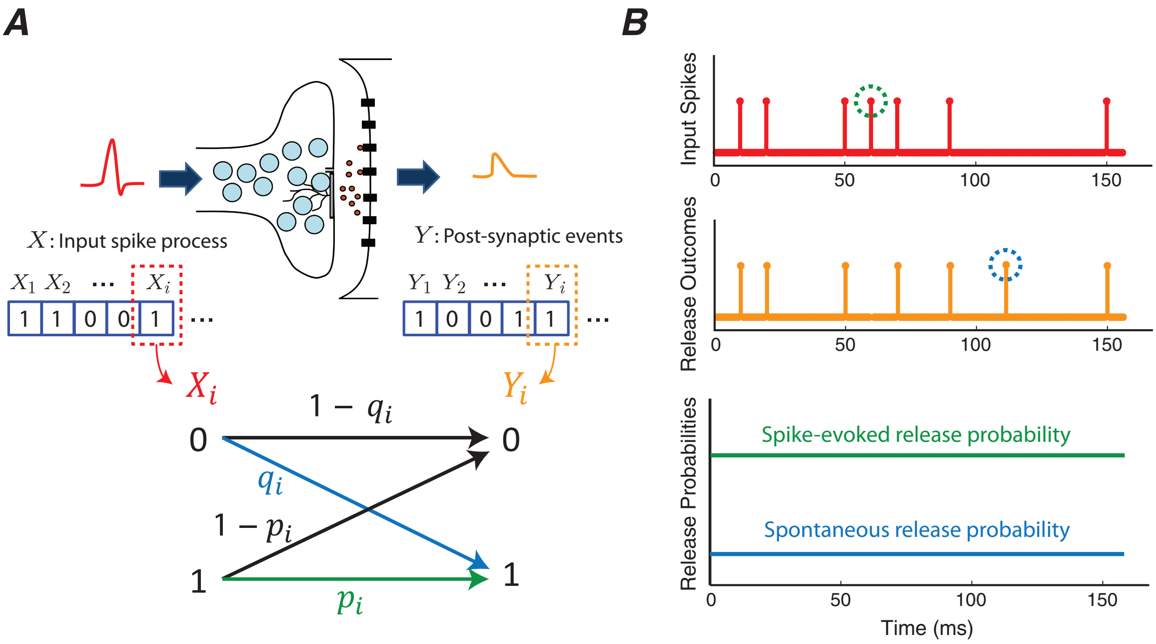

Figure 1.6: Modeling of a static synapse. (A) The synapse is modeled by a binary asymmetric channel. The input of the model is the input spike process and the output is a binary process corresponding to the presence/absence of the postsynaptic potential. The green transition arrow represents the spike-evoked release probability and the blue arrow models the spontaneous release of the synapse. (B) A typical input spike train and the release outcomes of the release site are depicted in the top two panels. Sometimes an action potential does not lead to a release (green circle) and sometimes the synapse releases spontaneously (blue circle). The bottom panel shows the release probabilities of spike-evoked and spontaneous release as a function of time.

transmission. For example, the energy consumption of the synapse imposes a constraint to the release mechanism. The energy cost of synaptic release is high and the neuron needs to find a compromise between its energy expenditure and the rate of information transfer.

The transmission delay is another major factor for signal communication in the brain. Imagine that the peripheral nervous system tries to inform the brain about a critical change in the environment. In this case, the transmission speed is more important than the energy consumption or the bit rate. The brain needs to make a decision as soon as possible to act properly in response to the external event; the energy-efficiency and the precision of the signal are no longer fundamental.

Synaptic transmission is also regulated to economize the limited resources of the neuron and achieve reliable transmission in the long term. If the neuron were to release many vesicles from the pool in response to a transient stimulus (for high

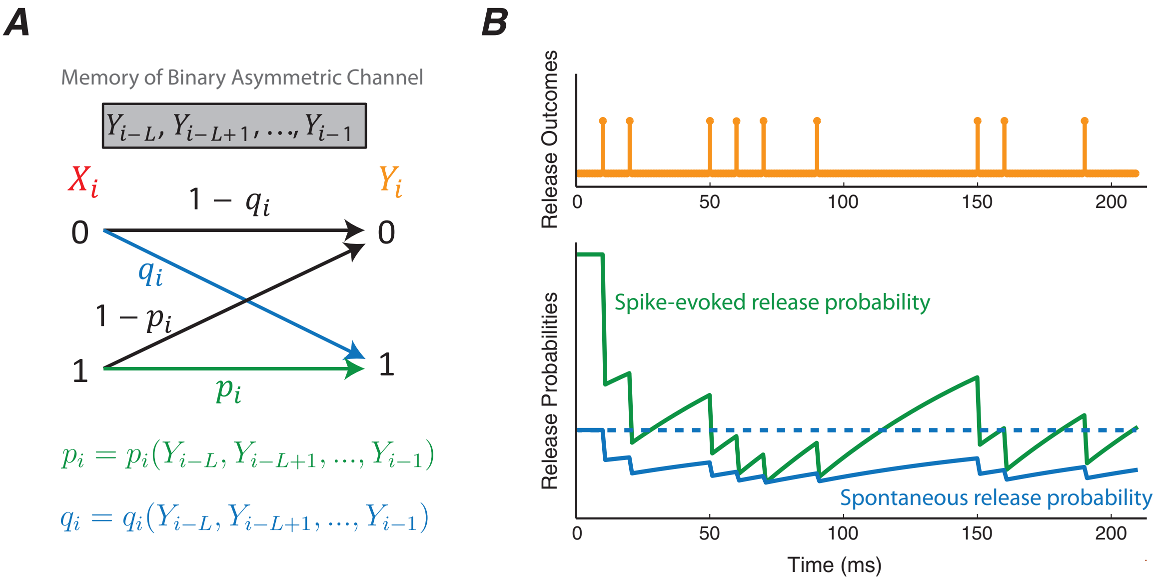

Figure 1.7: Modeling of a dynamic synapse. (A) A binary asymmetric channel with memory. The release probabilities of the synapse depend on the previous release outcomes. (B) A typical release outcome sequence of the synapse (top panel) and the spike-evoked and spontaneous release probabilities of the synapse (bottom panel). The solid and dashed blue lines show the two possible models of depression for spontaneous release.

transmission accuracy), then it could fail to transmit sufficient information for the next sequence of stimuli. Therefore, the different factors in transmission (such as information rate, energy consumption, latency) should be weighted according to the specific function of the synapse to derive the utility/cost function and determine the optimality of synaptic release.

In this thesis, we consider the energy consumption of synaptic release in addition to the mutual information rate. We define and calculate a new measure, named energy-normalized information rate, to study the trade-off between the energy consumption and the rate of information transmission during short-term depression.

We start with a simple model of short-term depression in which the state of the synapse is determined by the previous release outcome. If the synapse has released a vesicle, it goes to the used state, and in the absence of release, the synapse returns to the normal state. The two-state model of short-term depression permits an analytical study of synaptic information efficacy.

We then extend the model to implement the gradual depression and exponential recovery of the synapse during short-term depression. We use a binary asymmetric channel with a memory of an arbitrary length L (Fig. 1.7). We show that the dynamics of our model is consistent with the dynamics that has been observed in experimental data. We calculate the mutual information rate and energy-normalized information rate of the synapse analytically and evaluate the effect of synaptic parameters, such as recovery time constant and the level of depression, on the information efficacy of the synapse. The modulatory role of spontaneous release on the rate of information transmission is also investigated. The information-theoretic analysis of short-term depression reveals three functional classes for synapses and explains how a synapse compromises between the information rate and energy consumption.

1.7.3 Spike detection

Our framework can be used to calculate the information efficacy of a synapses from experimental data. To estimate synaptic information efficacy, the exact timing of the presynaptic action potentials and the postsynaptic release events is required. The timing of action potentials is usually estimated from intracellular or extracellular recordings. However, the detection of spikes in an extracellular signal with low signal to noise ratio (SNR) is challenging. We propose a new method for spike detection which is based on the fractal properties of the extracellular signals. Our results reveal a significant difference between the fractal dimension of spike and noise segments of extracellular signals. Based on this finding, we design a spike detector by thresholding the fractal dimension of the signal's segments. We show that in low SNR extracellular signals, our fractal spike detector outperforms the conventional spike detection algorithms.

1.7.4 Structure of the thesis

We present the results of the two-state model of short-term depression in Section 2. The content of this section has been already published in:

- M. Salmasi, M. Stemmler, S. Glasauer, A. Loebel, "Information Rate Analysis of a Synaptic Release Site Using a Two-State Model of Short-Term Depression", Neural Computation, 29, 1528-1560, 2017.

We analyze the information efficacy of the general model of short-term depression in Section 3. The section is in the format of a manuscript which is ready for submission:

- M. Salmasi, A. Loebel, S. Glasauer, M. Stemmler, “Short-Term Synaptic Depression Can Increase the Rate of Information Transfer at a Release Site”, To be submitted.

In Section 4, we present our suggested algorithm for spike detection in extracellular signals which is based on the fractal properties of the signals. The content of this section has been published in:

- M. Salmasi, U. Büttner, S. Glasauer, “Fractal Dimension Analysis for Spike Detection in Low SNR Extracellular Signals”, Journal of Neural Engineering, 13(3), 36004-36022, 2016.

Chapter 2

Information rate of the two-state model of depression

2.1 Summary

A synapse mediates information transmission by releasing vesicles in response to incoming action potentials. The synaptic release is, however, a stochastic mechanism. While some action potentials do not elicit a vesicle release, a synapse may release spontaneously even in the absence of an action potential. The information efficacy of the synapse is highly affected by the stochasticity of the release.

Synaptic release characteristics also depend on the activity history of the synapse. In short-term depression, the release probability of the synapse reduces after successive releases and the efficacy of the synapse is altered. We model a synaptic release site by two communication channels, corresponding to the normal state and the used state of the synapse. After each release, the synapse goes to the used state, and in the absence of release, the synapse recovers back to the normal state.

We calculate the information rate of the synapse model analytically and evaluate the effects of short-term depression and stochastic release on the information efficacy of the synapse. We show that the relative level of depression for spontaneous release and spike-evoked release determines weather depression enhances or impairs the rate of information transmission through the synapse.

2.2 Contributions

The contributions of the authors Mehrdad Salmasi (MS), Martin B. Stemmler (MBS), Stefan Glasauer (SG) and Alex Loebel (AL) are as follows: MS, MBS, SG and AL designed the study and developed the model. MS analyzed the model and performed the simulations. MS, MBS, SG and AL interpreted the results and wrote the manuscript.

The manuscript was published in the journal of Neural Computation:

- M. Salmasi, M. Stemmler, S. Glasauer, A. Loebel, "Information Rate Analysis of a Synaptic Release Site Using a Two-State Model of Short-Term Depression", Neural Computation, 29, 1528-1560, 2017.

The preliminary results of this study were presented as abstracts and posters in the CNS (2015) and Bernstein (2016) conferences:

- M. Salmasi, M. Stemmler, S. Glasauer, A. Loebel, "Information-Theoretic Analysis of a Dynamic Release Site Using a Two-Channel Model of Depression", 24th Annual Computational Neuroscience Meeting (CNS), Prague, July 2015.
- M. Salmasi, M. Stemmler, S. Glasauer, A. Loebel, "The Impact of Depression on the Information Rate of the Two-Channel Model of Release Site", Bernstein Conference on Computational Neuroscience (BCCN), Heidelberg, September 2015.

LETTER Communicated by Mark McDonnell

Information Rate Analysis of a Synaptic Release Site Using a Two-State Model of Short-Term Depression

Mehrdad Salmasi
mehrdad.salmasi@lrz.uni-muenchen.de
Graduate School of Systemic Neurosciences, Ludwig-Maximilians-Universität, and Bernstein Center for Computational Neuroscience, Munich 82152, Germany; German Center for Vertigo and Balance Disorders, Ludwig-Maximilians-Universität, Munich 81377, Germany

Martin Stemmler
stemmler@bio.lmu.de
Department of Biology II, Ludwig-Maximilians-Universität, and Bernstein Center for Computational Neuroscience, Munich 82152, Germany

Stefan Glasauer
s.glasauer@lrz.uni-muenchen.de
Graduate School of Systemic Neurosciences, Ludwig-Maximilians-Universität, and Bernstein Center for Computational Neuroscience, Munich 82152, Germany; German Center for Vertigo and Balance Disorders, and Department of Neurology, Ludwig-Maximilians-Universität, Munich 81377, Germany

Alex Loebel
loebel@biologie.uni-muenchen.de
Department of Biology II, Ludwig-Maximilians-Universität, and Bernstein Center for Computational Neuroscience, Munich 82152, Germany

Synapses are the communication channels for information transfer between neurons; these are the points at which pulse-like signals are converted into the stochastic release of quantized amounts of chemical neurotransmitter. At many synapses, prior neuronal activity depletes synaptic resources, depressing subsequent responses of both spontaneous and spike-evoked releases. We analytically compute the information transmission rate of a synaptic release site, which we model as a binary asymmetric channel. Short-term depression is incorporated by assigning the channel a memory of depth one. A successful release, whether spike evoked or spontaneous, decreases the probability of a subsequent release; if no release occurs on the following time step, the release probabilities recover back to their default values. We prove that synaptic depression can increase the release site's information rate if spontaneous release is more strongly depressed than spike-evoked release. When

Neural Computation **29, 1528–1560** (2017)
doi:10.1162/NECO_a_00962

depression affects spontaneous and evoked release equally, the information rate must invariably decrease, even when the rate is normalized by the resources used for synaptic transmission. For identical depression levels, we analytically disprove the hypothesis, at least in this simplified model, that synaptic depression serves energy- and information-efficient encoding.

1 Introduction

Synapses, the junction points between neurons, are essential for information processing in the nervous system (Eccles, Katz, & Kuffler, 1941; Foster & Sherrington, 1897). When an action potential arrives at the presynaptic bouton of a synapse, there is a probability that vesicles filled with neurotransmitter are released from release sites into the synaptic cleft (Del Castillo & Katz, 1954). Upon docking at the postsynaptic cell, the neurotransmitter initiates an electrochemical cascade to cause a voltage deflection in the postsynaptic cell's membrane, which in turn may lead to action potentials in the output and thus complete the input-output cycle. The average amplitude of the voltage deflection in response to unitary stimuli is usually considered to be the measure of the synaptic connection's efficacy (Bliss & Lømo, 1973; Dan & Poo, 2004; Gil, Connors, & Amitai, 1999; Markram, Lübke, Frotscher, & Sakmann, 1997; Nelson, Sjöström, & Turrigiano, 2002).

This notion of synaptic efficacy, however, ignores the short-term dynamics of transmission observed at many types of synapses (Markram & Tsodyks, 1996; Wang et al., 2006; Zucker & Regehr, 2002). These dynamics are reflected in time-dependent changes in the release probability. In short-term depression, the release probability decreases following a vesicle release, as it takes time for a release site to be refilled with a new vesicle; during quiescent periods, the release probability recovers back to a baseline (Zucker & Regehr, 2002). As a consequence, the postsynaptic responses of such a synaptic connection are time dependent. This renders the amplitude-driven interpretation of synaptic efficacy questionable, as it is not clear which amplitude to attach to a connection that exhibits short-term dynamics.

The short-term dynamics and the stochastic nature of synaptic transmission have led researchers to consider alternative measures of synaptic efficacy that are based on information theory (Fuhrmann, Segev, Markram, & Tsodyks, 2002; Goldman, 2004; London, Schreibman, Häusser, Larkum, & Segev, 2002; Manwani & Koch, 2001; Scott, Cowan, & Stricker, 2012; Zador, 1998). Presynaptic trains of action potentials and the postsynaptic responses convey information about each other, where the postsynaptic responses could be the time series of the output action potentials of the postsynaptic cell, the voltage fluctuations in the cell body, or the vesicle release outcomes. Quantification of synaptic information efficacy leads to a better understanding of the functional role of different synaptic properties, such as dendritic location, response amplitudes, and their dynamics. However, an analytical, closed-form expression for the synaptic information efficacy in the presence of short-term dynamics is still missing. Consequently, the study of how these dynamics and synaptic parameters affect the information transfer is limited. Nonetheless, reasonable assumptions are that synaptic depression might contribute to efficient coding (Cortes et al., 2012; Rangan, 2012) or modulate the information transfer at a given synapse (Rosenbaum, Rubin, & Doiron, 2012), possibly in a frequency-dependent manner.

Here, we adopt the information-theoretic approach and present a first step toward the analytical estimate of information transfer at a synapse that exhibits short-term depression. We consider a memoryless binary asymmetric channel system as a model for a static release site (Levy & Baxter, 2002) and extend it to a two-state system (i.e., a binary asymmetric channel with a memory of depth one). The current state of the release site is determined by the last output of the system. When a release occurred in the previous time step (through either an action potential or spontaneous release), the system is in the "used" state, in which the release probabilities are depressed. When no release occurs, the state switches to the "recovered" state. We calculate the mutual information rate of the two-state model of depression analytically. The closed-form equation for the information rate facilitates understanding how the parameters of depression affect synaptic efficacy.

The energy consumption of neural systems is a key element in neuronal information processing (Attwell & Laughlin, 2001; Sacramento, Wichert, & van Rossum, 2015; Sengupta, Laughlin, & Niven, 2013; Sengupta, Stemmler, Laughlin, & Niven, 2010; Sengupta, Stemmler, & Friston, 2013), so we also consider the energy costs of synaptic release. Many neuronal circuits can be interpreted as optimizing a trade-off between energy and information (Niven, Anderson, & Laughlin, 2007). However, in this simple model, we prove that, to the contrary, synaptic depression does not optimize such an energy-information trade-off as long as spontaneous and spike-evoked releases are equally depressed. If spontaneous release is more strongly suppressed, though, synaptic depression improves both the mutual and the energy-normalized information rates.

2 Model

A discrete-time model for a static release site is presented first; subsequently, the model is extended to include the dynamic properties of short-term synaptic depression.

2.1 Static Release Site: The One-State Model.

A static release site is modeled by a memoryless binary asymmetric channel (Levy & Baxter, 2002).

The input of the model is a presynaptic input spike train, which is represented by the random process X,

$$X = \{X_i\}_{i=0}^{\infty}, \tag{2.1}$$

where X_i is the random variable corresponding to the value of X at time i, $X_i = 1$ if there is a spike at time i, and $X_i = 0$ otherwise. We assume that X is an independent and identically distributed (i.i.d.) random process and X_i is a Bernoulli random variable with $P(X_i = 1) = \alpha$. The parameter α can be interpreted as the average input spike rate of the presynaptic neuron.

The output of the release site at time i is a binary random variable as well, and it is denoted by Y_i. If there is a release at time i, then $Y_i = 1$, and otherwise, $Y_i = 0$. The sequence of these random variables constructs the output random process of the model, which is denoted by Y,

$$Y = \{Y_i\}_{i=0}^{\infty}. \tag{2.2}$$

The memoryless binary asymmetric channel determines the relation between X_i and Y_i at time i (see Figure 1A). This model embraces two important synaptic phenomena: spontaneous release and synaptic unreliability. Spontaneous release is implemented by the transition from $X_i = 0$ to $Y_i = 1$, that is, even without an input spike, there can be a release with a probability of q. Also synaptic unreliability is captured by the transition from $X_i = 1$ to $Y_i = 0$. This transition indicates that there is a probability of $1 - p$ that an input spike does not result in a vesicle release. It directly follows that p and q are the spike-evoked and spontaneous release probabilities respectively.

In our model, one release site can release at most one vesicle per presynaptic spike, which is in agreement with the one-vesicle hypothesis (Biró, Holderith, & Nusser, 2005; Korn, Triller, Mallet, & Faber, 1981; Silver, Lübke, Sakmann, & Feldmeyer, 2003; Yusim, Parnas, & Segel, 2001).

2.2 Dynamic Release Site: The Two-State Model. In short-term synaptic depression, the release probability is reduced after a vesicle release, and then it recovers back to its initial value during quiescent periods. Here we consider a simplified model for this dynamics and represent a release site with short-term depression by a communication channel with a memory of depth one. That is, the state of the channel at time i is determined by the previous output of the channel, Y_{i-1}. Since Y_{i-1} is a binary random variable, the dynamic release site can be modeled as a combination of two interrelated binary asymmetric channels (see Figure 1B). If there is no release at time $i-1$, that is, $Y_{i-1} = 0$, then the release site at time i follows the recovered state of the channel. If there has been a release at time $i-1$, that is, $Y_{i-1} = 1$, the release site at time i follows the used state of the channel. We assume that the initial state of the release site at time $i = 1$ is the recovered state;

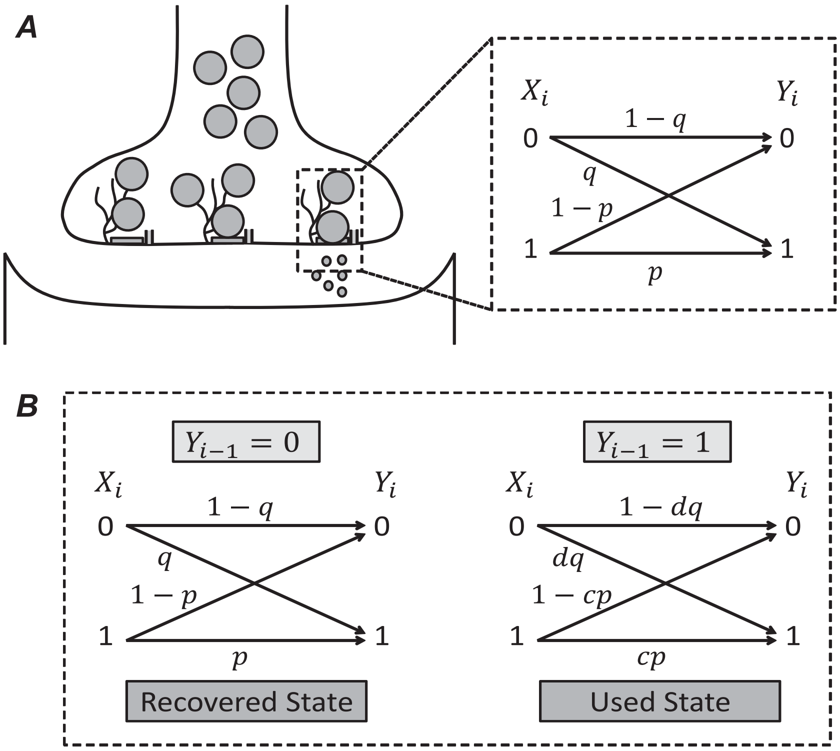

Figure 1: (A) A static release site is modeled by a memoryless binary asymmetric channel. (B) A dynamic release site with depression is modeled by a binary asymmetric channel with a memory of depth one. In particular, if a release occurs at time $i-1$, the channel will be at the used state at time i; if no release occurs, the channel will be at the recovered state at the next time step.

by convention, $Y_0 = 0$. We call this model throughout the letter the *two-state model* of depression. The parameters of the model fulfill the following inequalities:

$$0 < c, d, p, q < 1, \tag{2.3}$$

$$q < p, \tag{2.4}$$

$$dq < cp. \tag{2.5}$$

The inequalities $0 < c, d < 1$ entail the reduction of the release probabilities of the used state. Also, equations 2.4 and 2.5 indicate that the probability of spike-evoked release is higher than the probability of spontaneous release. We note that the spike-evoked release probability is a function of the number of vesicles in the release-ready pool, the proximity of the vesicles to the active zone, and the level of intracellular calcium around the release site (Zucker & Regehr, 2002). When the size of the release-ready pool shrinks, the release probability of the release site decreases gradually until the vesicles from the reserve pool replenish the release-ready pool again

Table 1: Definition of Notations.

Symbol	Definition
X	Presynaptic input spike process
Y	Release outcome process
p	Spike-evoked release probability
q	Spontaneous release probability
c	Depression multiplier for spike-evoked release
d	Depression multiplier for spontaneous release
α	Presynaptic input spike rate
r_D	Mutual information rate of the release site with depression
$I_E^{(D)}$	Energy-normalized information rate of the release site with depression
r_1	Mutual information rate of the release site without depression
$I_E^{(1)}$	Energy-normalized information rate of the release site without depression

and increase the release probability. Therefore, depending on the size of the release-ready pool, the release probability can be greater than zero even in the used state and the release site is potentially capable of releasing a vesicle at any time point. This feature is consistent with the stochastic nature of synaptic release (Zucker & Regehr, 2002) and probabilistic models of synaptic depression (Hanse & Gustafsson, 2001). (For a summary of notations, see Table 1.)

2.3 Information-Theoretic Measures. The entropy of a discrete random variable Z is the amount of uncertainty about its value and is defined as

$$H(Z) = -\sum_{z} P(Z = z) \log_2 P(Z = z), \tag{2.6}$$

where $P(.)$ is the probability measure.

The conditional entropy $H(Z|W)$ is the entropy of the random variable Z given that the value of the random variable W is known. It is defined as

$$H(Z|W) = -\sum_{w} \sum_{z} P(Z = z, W = w) \log_2 P(Z = z|W = w). \tag{2.7}$$

The mutual information between two random variables Z and W, denoted by $I(Z; W)$, is a measure of their dependence and is equal to the reduction of the uncertainty of one of the random variables due to the other one. The mutual information can be defined using the entropy and conditional entropy in the following manner:

$$I(Z; W) = H(Z) - H(Z|W). \tag{2.8}$$

The definition of entropy for a random variable is extended to the entropy rate of random processes (Cover & Thomas, 2012). Let $X = \{X_i\}_{i=0}^{\infty}$ be a discrete-time random process, where X_i is the random variable corresponding to the value of X at time i. We denote by X^n the values of X in the first n time units:

$$X^n \triangleq \begin{cases} (X_1, X_2, \dots, X_n) & \text{if} \quad n > 0 \\ 0 & \text{if} \quad n = 0 \end{cases}. \tag{2.9}$$

The entropy rate of X is defined by

$$H(X) = \lim_{n\to\infty} \frac{1}{n} H(X^n) \tag{2.10}$$

if the limit exists.

The notion of mutual information can be generalized to random processes as well (Vembu et al., 1995). The mutual information rate between the two random processes X and Y is defined by

$$I(X;Y) = \lim_{n\to\infty} \frac{1}{n} I(X^n; Y^n), \tag{2.11}$$

provided that the limit exists.

3 Analytical Results

We derive the mutual information rate of the two-state model of a dynamic release site. We subsequently consider the energy consumption of the release site and define a measure that captures the energy-normalized information rate. Finally, we demonstrate the impact of depression on the information efficacy of the release site. For brevity, the proofs of the theorems are presented in the appendix.

The entropy of a binary random variable Z with $P(Z = 0) = z$ is represented by $h(z)$:

$$h(z) = -z \log_2(z) - \overline{z} \log_2(\overline{z}), \tag{3.1}$$

$$h(0) = h(1) = 0, \tag{3.2}$$

where $\overline{z} = 1 - z$. From the symmetry of $h(.)$, it is clear that $h(z) = h(\overline{z})$. For the binary asymmetric channel in Figure 1A,

$$H(Y_i) = h(\overline{\alpha} q + \alpha p), \tag{3.3}$$

$$H(Y_i|X_i) = \overline{\alpha} h(q) + \alpha h(p). \tag{3.4}$$

Therefore, the mutual information between the input and output random variables of the channel, X_i and Y_i, is

$$I(X_i; Y_i) = h(\overline{\alpha} q + \alpha p) - \overline{\alpha} h(q) - \alpha h(p), \tag{3.5}$$

and since the channel is memoryless, its mutual information and mutual information rate are identical:

$$I(X; Y) = I(X_i; Y_i). \tag{3.6}$$

Let r_1 and r_2 be the mutual information rates of the recovered and used states in Figure 1B. From equation 3.5,

$$r_1 = I(X_i; Y_i | Y_{i-1} = 0) \tag{3.7}$$

$$= h(\overline{\alpha} q + \alpha p) - \overline{\alpha} h(q) - \alpha h(p), \tag{3.8}$$

$$r_2 = I(X_i; Y_i | Y_{i-1} = 1) \tag{3.9}$$

$$= h(\overline{\alpha} dq + \alpha cp) - \overline{\alpha} h(dq) - \alpha h(cp). \tag{3.10}$$

We prove in the appendix (see lemma 1) that for the two-state model.

$$I(X^n; Y^n) = nr_2 + (r_1 - r_2)(n\theta + (1 - \theta)\frac{1 - \lambda^n}{1 - \lambda}), \tag{3.11}$$

where

$$\lambda = g_1 - g_2, \tag{3.12}$$

$$\theta = \frac{g_2}{\overline{g_1} + g_2}, \tag{3.13}$$

$$g_1 = \overline{\alpha}\, \overline{q} + \alpha \overline{p}, \tag{3.14}$$

$$g_2 = \overline{\alpha}\, \overline{dq} + \alpha \overline{cp}. \tag{3.15}$$

We are now ready to calculate the information rate of the two-state model.

Theorem 1. *Let r_D denote the mutual information rate of the two-state model of depression in Figure 1B. Then*

$$r_D = \theta r_1 + (1 - \theta) r_2. \tag{3.16}$$

Corollary 1. *The mutual information rate of the two-state model of depression, r_D, is the weighted sum of the information rates of its constituent channels, and* *the weights, θ and $1-\theta$, are the asymptotic probabilities of being in the recovered state and used state, respectively:*

$$\theta = \lim_{i\to\infty} P(Y_i = 0). \tag{3.17}$$

The information rate r_D is only one possible measure for the information efficacy of a release site. In particular, the transfer of information through synaptic releases is an energetically costly process (Balasubramanian, Kimber, & Berry II, 2001; Friston, 2010; Levy & Baxter, 1996). To address this aspect of synaptic activity, we consider a quantity that reflects both the information rate and the energy consumption of the synapse simultaneously. Let E_i be the average amount of energy that is consumed at time i by the presynaptic neuron for vesicle release. We represent the energy-normalized mutual information between X^n and Y^n by $I_E(X^n; Y^n)$ and define it as

$$I_E(X^n; Y^n) \triangleq \frac{I(X^n; Y^n)}{\sum_{i=1}^{n} E_i}. \tag{3.18}$$

We assume that for each release, one unit of energy is consumed. Consequently, E_i is equal to the probability of release at time i. In the case of the two-state model, we show in the appendix (see lemma 2) that

$$I_E(X^n; Y^n) = \frac{nr_2 + (r_1 - r_2)(n\theta + (1-\theta)\frac{1-\lambda^n}{1-\lambda})}{(1-\theta)(n - \lambda\frac{1-\lambda^n}{1-\lambda})}. \tag{3.19}$$

Subsequently, let $I_E(X; Y)$ be the energy-normalized information rate, which is defined as

$$I_E(X; Y) \triangleq \lim_{n\to\infty} I_E(X^n; Y^n). \tag{3.20}$$

We should note that the term $\frac{1}{n}$ does not appear in equation 3.20, because both terms $I(X^n; Y^n)$ and $\sum_{i=1}^{n} E_i$ in equation 3.18 are normalized by $\frac{1}{n}$.

Using $I_E^{(D)}$ to represent $I_E(X; Y)$ for the two-state model of depression, we show that

$$I_E^{(D)} = \frac{g_2 r_1 + \overline{g_1} r_2}{\overline{g_1}}. \tag{3.21}$$

Corollary 2. *Consider the recovered state and used state in Figure 1B and let their energy-normalized information rates be* $I_E^{(1)}$ *and* $I_E^{(2)}$*. It follows that*

$$I_E^{(1)} = \frac{r_1}{\overline{g_1}}, \tag{3.22}$$

$$I_E^{(2)} = \frac{r_2}{\overline{g_2}}. \tag{3.23}$$

And $I_E^{(D)}$ *is found to be simply the linear summation of these two terms:*

$$I_E^{(D)} = g_2 I_E^{(1)} + \overline{g_2} I_E^{(2)}. \tag{3.24}$$

We note that if $I_E^{(D)} < I_E^{(1)}$, then $r_D < r_1$ (see the appendix). In other words, if depression decreases the energy-normalized information rate of the release site, then it will also decrease the mutual information rate.

We also note that since the static release site is identical to the recovered state of the dynamic release site, r_1 and $I_E^{(1)}$ also represent the mutual information rate and energy-normalized information rate of the static release site.

The above results allow us to analytically study the effect of depression on the two measures of the release site: mutual information rate and energy-normalized information rate. First, if the depression level is the same for spontaneous release and spike-evoked release (i.e., $c = d$), then there is no benefit for depression from the standpoint of mutual information rate and energy-normalized information rate.

Theorem 2. *Let* $c = d$*. For all values of* α, d, p*, and* q*,*

$$I_E^{(D)} \leq I_E^{(1)}, \tag{3.25}$$

$$r_D \leq r_1. \tag{3.26}$$

Hence, for both measures, the release site without depression performs better. However, when the depression levels for spontaneous and spike-evoked releases are not equal, then depression can enhance the performance of the release site:

Theorem 3. *For each* α, p, q*, and* d*, there exists* c_0*,* $d \leq c_0 < 1$*, such that for each* $c > c_0$*,*

$$r_D > r_1, \tag{3.27}$$

$$I_E^{(D)} > I_E^{(1)}. \tag{3.28}$$

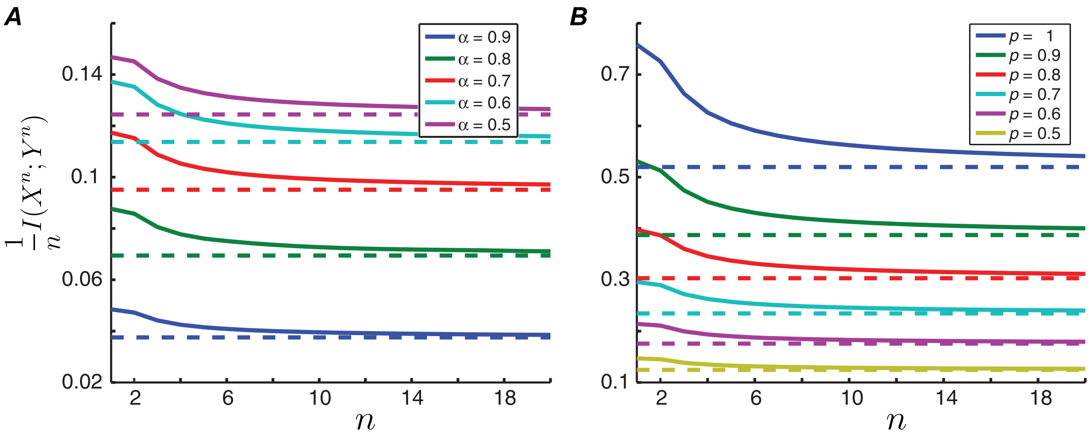

Figure 2: The convergence rate of the mutual information for the two-state model of depression. The mutual information $\frac{1}{n}I(X^n;Y^n)$ (solid lines) is plotted as a function of n for (A) different values of input spike rate α, (B) different values of spike-evoked release probability p. The dashed lines represent r_D, which is the limit of $\frac{1}{n}I(X^n;Y^n)$ when n tends to infinity. The other parameters of the model are $q = 0.1$ and $c = d = 0.5$. Additionally, in panel A, $p = 0.5$, and in panel B, $\alpha = 0.5$.

That is, if the depression multiplier of the spike-evoked release is above a threshold, then the mutual information rate and energy-normalized information rate are increased by depression.

4 Simulation Results

The convergence of the mutual information $I(X^n;Y^n)$ to r_D was found to be fast for all values of the input spike rate α (see Figure 2A) and spike-evoked release probability p (see Figure 2B). The high convergence rate shows that the release site reaches its steady state very fast, and therefore our results remain valid even for the release sites with slowly varying parameters.

We investigate the effect of model's parameters on the mutual information rate of the two-state model of depression. As mentioned in corollary 3, the mutual information rate r_D is a linear summation of r_1 and r_2 with a weight function θ (see Figure 3A). When the input spike rate is reduced, θ increases and the weight of the recovered channel is strengthened in determining r_D. This is expected because by reducing the rate of the input spike train, the number of releases is reduced and the channel stays more in the recovered state. When the input spike rate is increased, the weight shifts from the recovered channel to the used channel.

The mutual information rate also depends on the value of the spike-evoked release probability, p. As p decreases, the unreliability of the release site increases and r_D is strongly reduced (see Figure 3B). In comparison, increasing the depression level has a much weaker effect on

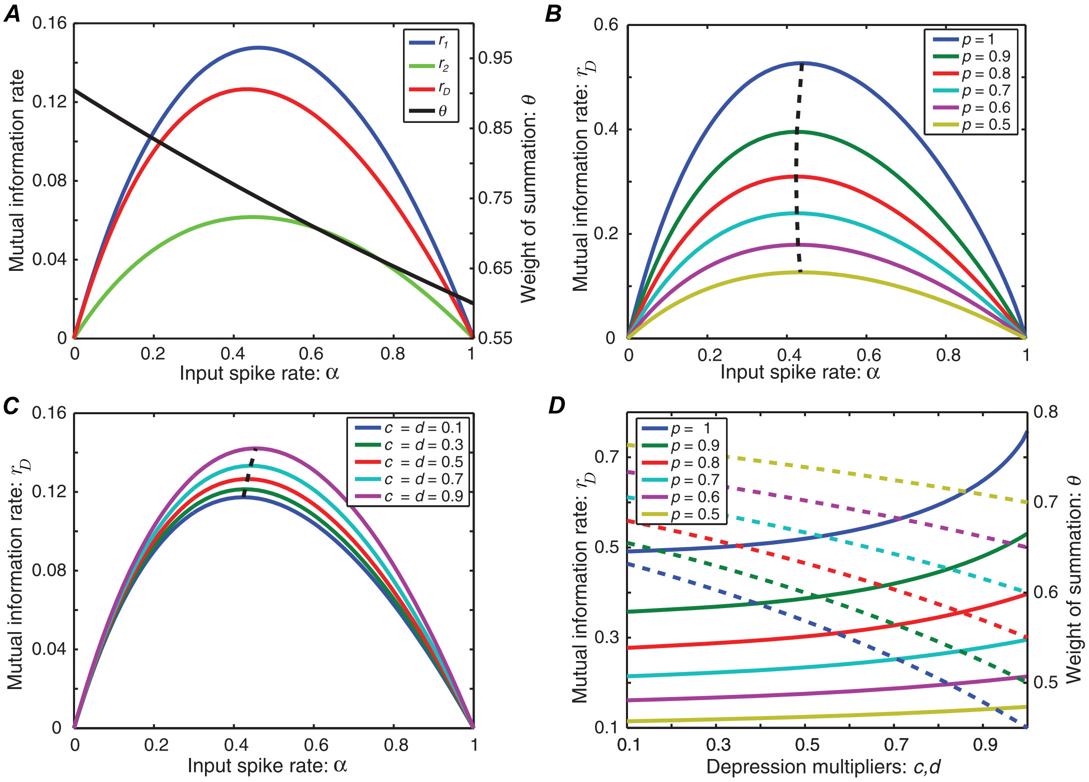

Figure 3: (A) The mutual information rate of the two-state model, r_D, together with the mutual information rates of the recovered channel, r_1, and used channel, r_2, as a function of input spike rate, α. The solid black line is the weight function, θ. The values for the other parameters are $p = 0.5$, $q = 0.1$, $c = d = 0.5$. (B) The mutual information rate, r_D, as a function of the input spike rate, α, for different values of the spike-evoked release probability, p. The other parameters are fixed at $q = 0.1$ and $c = d = 0.5$. (C) The mutual information rate, r_D, as a function of the input spike rate, α, for different values of the depression multipliers, c and d. The dashed black lines in panels B and C indicate the capacity of the release site, $\mathcal{C}_D$. The other simulation parameters are $p = 0.5$, $q = 0.1$. (D) The mutual information rate of the two-state model as a function of the depression multipliers, c and d, for different values of the spike-evoked release probability, p. The dashed lines show the weight function, θ. In this simulation, $c = d$, $q = 0.1$, and $\alpha = 0.5$.

r_D (see Figure 3C). In communication systems, the capacity of a channel is defined as the maximum amount of information that can be transferred through the channel. If we denote the capacity of the two-state model by $\mathcal{C}_D$, then

$$\mathcal{C}_D = \max_{\alpha \in [0,1]} r_D. \tag{4.1}$$

We show in Figure 3B that the value of the input spike rate at which the capacity is attained does not change significantly for different spike-evoked

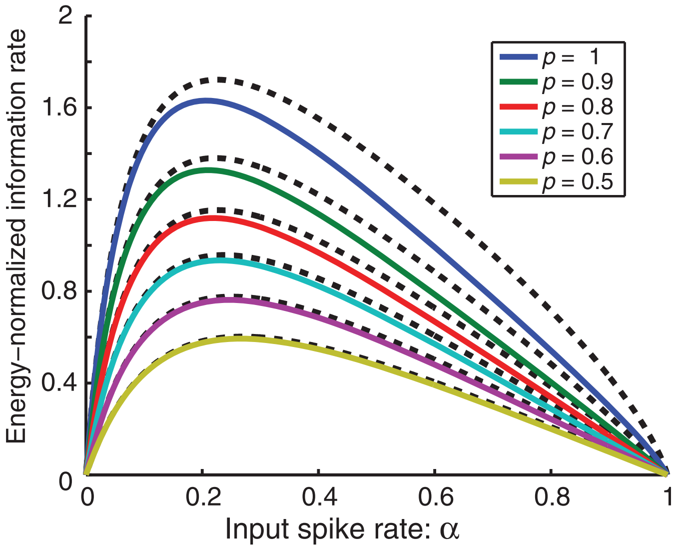

Figure 4: The effect of depression for the case of identical depression multipliers. The energy-normalized information rate of the two-state model of depression, $I_E^{(D)}$, is plotted against the input spike rate for different values of p (colored lines). For comparison, the energy-normalized information rate of the static release site, $I_E^{(1)}$, is plotted as well for corresponding p values (dashed black lines). The remaining simulation parameters are $c = d = 0.5$ and $q = 0.1$.

release probabilities. However, by decreasing the depression multipliers c and d (increasing the level of depression), the capacity of the release site is attained at lower input spike rates (see Figure 3C). Hence, the optimal spike rate of the presynaptic neuron has a reverse relationship with the depression level of its release site. This means that synaptic depression can save energy while maintaining the information rate.

The mutual information rate r_D and the weight function θ are nonlinear functions of the depression multipliers (see Figure 3D). When the level of depression is decreased (by increasing c and d), the mutual information rate of the used channel, r_2, is increased. However, r_1 is independent of the depression, and for $c = d$, we have $r_1 \geq r_2$. Therefore, there are two competing terms in $r_D = \theta r_1 + (1-\theta)r_2$. While θr_1 is a decreasing function of d, the other term, $(1-\theta)r_2$, increases. Overall, we find that the latter term has a greater effect, and r_D is an increasing function of d.

We investigated the subspace of the parameters for which depression decreases or increases the performance of the release site. As expressed in theorem 1, we see in Figure 4 that when the depression levels of the spike-evoked release and spontaneous release are equal, $I_E^{(1)}$ is always larger than $I_E^{(D)}$. In other words, depression decreases the energy-normalized information rate of the release site. Additionally, we found that the maximum of the energy-normalized information rates in Figure 4 are attained at lower input spike rates compared to the spike rates that maximize r_D in

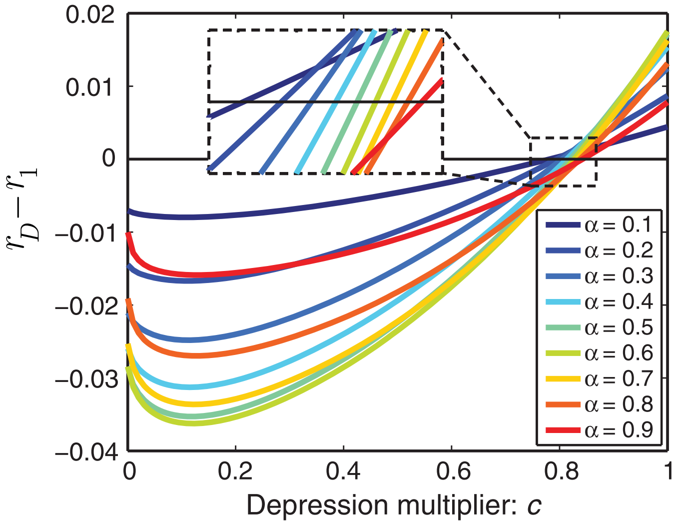

Figure 5: The transition in the impact of depression. The difference between mutual information rate of the release site with and without depression, $r_D - r_1$, is plotted as a function of the depression multiplier, c, for different values of the input spike rate, α. The intersection of the lines with the horizontal axis determines c_0. In the inset, we zoom on the intersection points to see their order as a function of the input spike rate. The other parameters of the simulation are $p = 0.5$, $q = 0.1$, and $d = 0.5$.

Figure 3B. Hence, optimizing the energy-normalized mutual information is energetically more efficient.

When the depression levels c and d are allowed to differ, depression increases the mutual information rate and energy-normalized information rate for all values of $c > c_0$ (see theorem 3). In Figure 5, we see the transition point, c_0, at which the sign of $r_D - r_1$ switches from negative to positive. When the input spike rate decreases, the value of c_0 is also decreased (see the inset of Figure 5). This means that for lower input spike rates, depression can enhance the performance of the release site for a larger subset of the values of depression multiplier c.

Finally, the orange regions in Figure 6 show the locus of parameters for which depression increases the mutual information rate (first row) or energy-normalized information rate (second row) of the release site. In particular, for each column, the orange regions of the first row are a subset of the orange regions of the second row. In other words, if for a set of parameters $r_D > r_1$, then $I_E^{(D)} > I_E^{(1)}$, which is in agreement with our analytical results.

5 Discussion

We modeled depression at a synaptic release site as a switch between two binary asymmetric channels with different release probabilities, representing

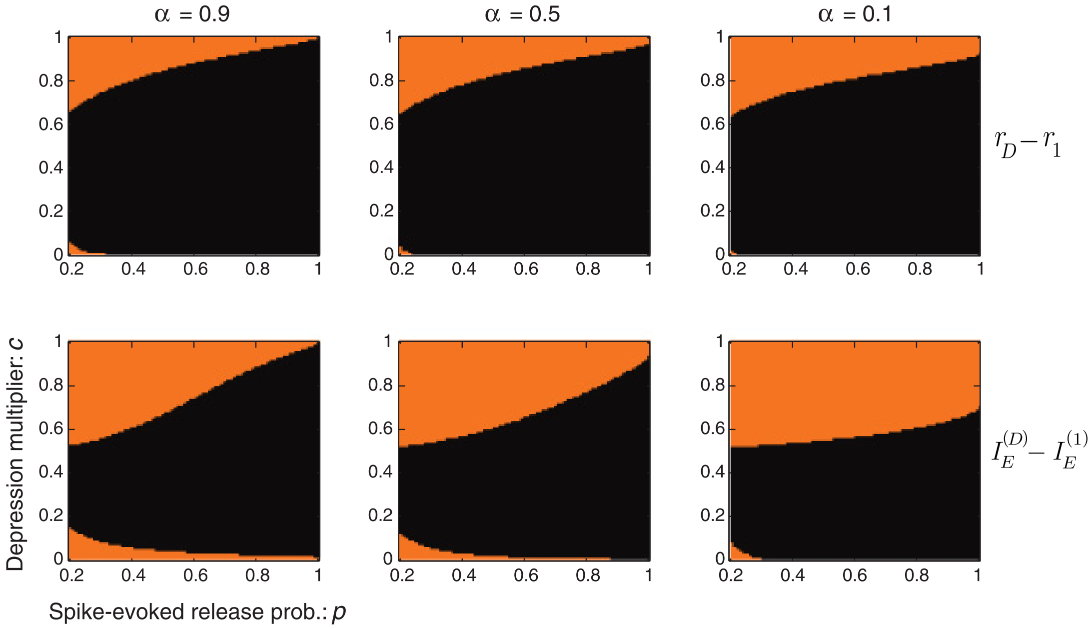

Figure 6: The subspace of parameters, the depression multiplier (c), and the spike-evoked release probability (p), for which depression increases the mutual information rate (first row) and the energy-normalized information rate (second row) of the release site. The orange regions depicts the cases in which $r_D - r_1 > 0$ (upper row) and $I_E^{(D)} - I_E^{(1)} > 0$ (lower row). The columns correspond to different values of the input spike rate, α.

used and recovered states of the release site. Such a simplified model of depression permits the calculation of the information rate in closed form, which reveals that a depressing channel's information rate is a linear sum of the rates of its two constituent channels. This result, although simple, is nontrivial. In particular, for the other form of short-term synaptic dynamics, short-term facilitation, in which the current state of the channel depends on the previous input instead of the previous output, the information rate exceeds that of a linear sum (unpublished results).

To investigate a possible trade-off between the information rate and energy cost of synaptic transmission, we computed an energy-normalized mutual information rate in which we assigned a unit cost to each vesicle release. The energy costs associated with generating the presynaptic spike trains or maintaining the synapse during quiescent periods were not taken into account. In addition, we represented the depression levels of spontaneous and spike-evoked release with two distinct parameters, reflecting recent findings that show that these two release processes are governed by separate biological mechanisms, such as alternative SNARE proteins, distinct vesicle pools, and spatial segregation (Fredj & Burrone, 2009; Melom, Akbergenova, Gavornik, & Littleton, 2013; Walter, Haucke, & Sigrist, 2014) (for a recent review, see Kavalali, 2015). We analytically proved that when the spontaneous release is more strongly depressed than spike-evoked release, synaptic depression can enhance the performance of the release site (see Figure 6). However, if the depression levels of spontaneous and spike-evoked release are identical, then depression degrades even the energy-normalized mutual information rate of the release site. Thus, short-term depression, although it reduces the amount of synaptic resources used in response to ongoing neuronal inputs, can fail to enhance the performance-energy trade-off.

Synaptic information efficacy has been studied numerically and analytically. In the numerical studies, the signals are converted to binary sequences and the mutual information is evaluated by any number of estimation methods for entropy and mutual information (Arleo et al., 2010; London, Larkum, & Häusser, 2008; London et al., 2002; Neymotin, Jacobs, Fenton, & Lytton, 2011). The temporal correlation between the input and output signal, which can be on the order of hundreds of milliseconds in short-term synaptic plasticity, imposes a major limitation on the numerical methods. To estimate the synaptic information efficacy analytically, Fuhrmann et al. (2002) adopt the depression model of Markram and Tsodyks (1996). In particular, they calculate the mutual information between the current postsynaptic potential and the presynaptic input spike train. However, as this approach ignores the history of the postsynaptic voltage trace, it cannot be used to evaluate the impact of depression on the mutual information rate. Goldman (2004) models the input and output signal of a dynamic synapse by renewal processes. The mutual information per vesicle release is calculated for the synapse, which reveals that depression enhances the synaptic information rate for correlated input. When the release probabilities are low, the mutual information rate per unit time is a more appropriate measure (Goldman, 2004), which is what we calculated. In addition, the previous two approaches had not taken spontaneous release into account (Fuhrmann et al., 2002; Goldman, 2004). Depression of spontaneous release can enhance the mutual information rate even for uncorrelated input. Our results show that the relative degree of depression of spontaneous and spike-evoked release plays a critical role in synaptic information efficacy.

In the two-state model of depression, the state-space is strongly reduced and does not reflect the intermediate states one would have to introduce to model the gradual exponential recovery of a synapse after a release event. But only such a reduced-state model is mathematically tractable, which has the advantage that we gain a precise, analytical expression of the synaptic information efficacy in the presence of short-term synaptic depression. Although the exponential recovery is not explicitly modeled, the two-state model is still a good approximation for synapses in which $\nu \times \tau_r < 0.5$, where ν is the input spike rate (in Hz) and τ_r is the recovery time constant of the synapse (in seconds). As an example for such synapses, we can consider synapses with fast recovery that return to the recovered state with a time constant of 6 to 40 milliseconds (Cho, Li, & Von Gersdorff, 2011;

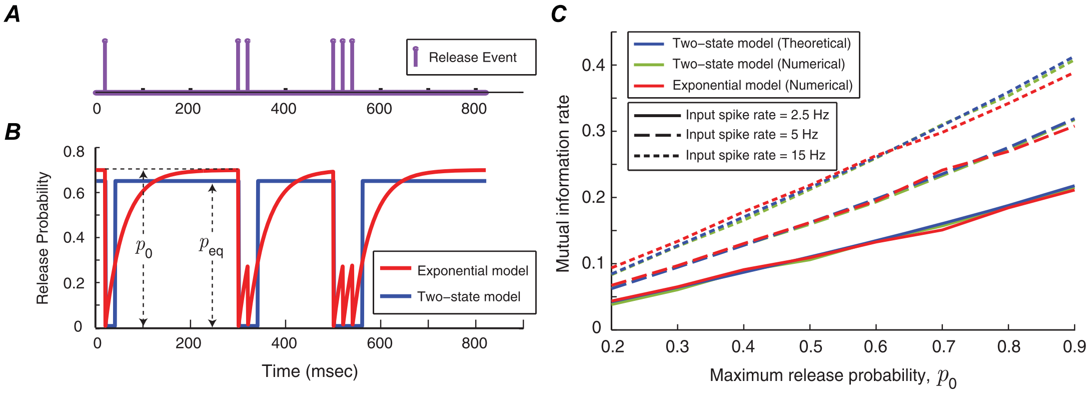

Figure 7: Comparison of the two-state model and the exponential model for a synapse with fast recovery. (A) A typical sequence of the release events of the synapse. (B) The release probabilities of the two-state model and the exponential model in response to the release events. In the exponential model, the release probability is reset to zero after each release and then recovers back exponentially to its maximum (initial) release probability, p_0. In the two-state model, the release probability switches between zero and p_{eq}. (C) The mutual information rate between the input spike train, X, and the release outcome, Y, is calculated as a function of maximum (initial) release probability, p_0. The context tree weighting algorithm, which is available online (Jiao, Permuter, Zhao, Kim, & Weissman, 2013; codes are available at http://web.stanford.edu/~tsachy/DIcode/index.htm). is used to derive a numerical estimate of the mutual information rates of the exponential model and the two-state model. These simulations are based on the parameters of the synapses between cerebellar climbing fiber and Purkinje cells (in rats). The recovery time constant of the synapse is $\tau_r = 40$ msec, and the time unit of the model is set to $\delta = 20$ msec. The input spike rate of the two-state model, α, is related to the spike rate of the exponential model, ν, by $\alpha = \nu(\text{in Hz}) \times \delta(\text{in seconds})$. Finally, p_{eq} is the equivalent release probability of the recovered state that is calculated from $p_{eq} = p_0(1-\alpha)^k + \sum_{i=1}^{k} \alpha(1-\alpha)^{i-1}(1 - e^{\frac{-(i+1)\delta}{\tau_r}})p_0$, where k is the number of time units used for estimating p_{eq}. In this simulation, we set $k = 8$ to cover a time interval of $4\tau_r$.

Hallermann & Silver, 2013; Wang & Manis, 2008). These synapses show a form of depression known as very short-term depression (Dobrunz, Huang, & Stevens, 1997). For such synapses making fast transitions between the recovered state and the depressed (used) state, we can calculate the information rate with high accuracy using the two-state model of depression (see Figure 7).

The discrete time of our model, represented by the index i, is related to the real time, t, through $t = i\delta$, where δ is the time interval between the two discrete time indexes i and $i+1$. The results of this letter are independent of the choice of δ, and our model gives one the freedom to select a proper value for δ based on the depression dynamics. The time unit of the two-state model, δ, should be in the same order of magnitude as the recovery time constant of the synapse, τ_r. For example, by setting $\delta = \frac{\tau_r}{2}$, we can get close approximations for the information rates of the synapse, provided that the synapse fulfills the aforementioned condition.

The mutual information rate that has been calculated in this letter is a measure of the amount of information that can be extracted from the released vesicles about the input spike train. Such mutual information rates are achievable only if the information is encoded and decoded optimally. However, since the brain has limited resources, which may confine the complexity of the encoders and decoders, the mutual information rate should be interpreted as an upper bound for the rate of information transfer. We also note that synapses have not necessarily evolved to optimize the mutual information rate. Several other factors in addition to the transmission rate govern synaptic processes, such as energy consumption, the latency of information transmission, and the limited size of vesicle pools and availability of other resources. Here, we studied a compromise between the energy use and the rate of information transmission. However, a comprehensive understanding of optimality of synaptic release will take into account the specific functionality of the synapse, its strength, and other factors affecting transmission.

The simple model for synaptic depression presented here is a steppingstone for further studies that will incorporate more realistic features of synaptic transmission. The current model can be extended to communication channels with arbitrary memory length, which will capture the gradual nature of recovery from depression, and the input of the presynaptic neuron can be generalized from a simple homogeneous Poisson process to a time-varying process with arbitrary temporal correlation. We also intend to model short-term facilitation and release-independent depression using the binary asymmetric channels with input-dependent states, where the state of the channel is determined by the history profile of presynaptic spikes. We predict that short-term facilitation will enhance the mutual information rate of the release site for normal ranges of parameters. In addition, synaptic connections have from one to hundreds of release sites (Clarke, Chen, & Nishimune, 2012), where each site may have different properties (Branco & Staras, 2009). Extending the model to multiple release sites by considering sets of parallel communication channels will permit a rigorous analysis of the information efficacy of whole synapses.

Appendix: Proofs of Theorems

Lemma 1. *For the two-state model of dynamic release site in Figure 1B,*

$$I(X^n; Y^n) = nr_2 + (r_1 - r_2)(n\theta + (1-\theta)\frac{1-\lambda^n}{1-\lambda}) \tag{A.1}$$

where

$$\lambda = g_1 - g_2, \tag{A.2}$$

$$\theta = \frac{g_2}{\overline{g_1} + g_2}, \tag{A.3}$$

$$g_1 = \overline{\alpha}\,\overline{q} + \alpha\overline{p}, \tag{A.4}$$

$$g_2 = \overline{\alpha}\,\overline{dq} + \alpha\overline{cp}. \tag{A.5}$$

Proof of Lemma 1. From the definition of mutual information,

$$I(X^n; Y^n) = H(Y^n) - H(Y^n|X^n). \tag{A.6}$$

We use the chain rule for the entropy terms in equation A.6:

$$H(Y^n) = \sum_{i=1}^{n} H(Y_i|Y^{i-1}), \tag{A.7}$$

$$H(Y^n|X^n) = \sum_{i=1}^{n} H(Y_i|Y^{i-1}, X^n). \tag{A.8}$$

The output of the channel at time i depends only on X_i and Y_{i-1}. Therefore, given X_i and Y_{i-1}, Y_i is independent of $\{X_j : j \neq i\}$ and $\{Y_j : 1 \leq j \leq i-2\}$. Therefore, for arbitrary values of $a^i = (a_1, a_2, \ldots, a_i)$ and $b^n = (b_1, b_2, \ldots, b_n)$,

$$P(Y_i = a_i|Y^{i-1} = a^{i-1}, X^n = b^n) = P(Y_i = a_i|Y_{i-1} = a_{i-1}, X_i = b_i). \tag{A.9}$$

This implies

$$H(Y_i|Y^{i-1}, X^n) = H(Y_i|Y_{i-1}, X_i), \tag{A.10}$$

and together with equation A.8,

$$H(Y^n|X^n) = \sum_{i=1}^{n} H(Y_i|Y_{i-1}, X_i). \tag{A.11}$$

Also, given Y_{i-1}, Y_i is independent of $\{Y_j : 1 \leq j \leq i-2\}$, because for arbitrary values of $a^i = (a_1, a_2, \ldots, a_i)$,

$$P(Y_i = a_i|Y^{i-1} = a^{i-1}) = \sum_{b_i \in \{0,1\}} P(Y_i = a_i|Y^{i-1} = a^{i-1}, X_i = b_i)P(X_i = b_i) \tag{A.12}$$

$$= \sum_{b_i \in \{0,1\}} P(Y_i = a_i|Y_{i-1} = a_{i-1}, X_i = b_i)P(X_i = b_i) \tag{A.13}$$

$$= P(Y_i = a_i|Y_{i-1} = a_{i-1}). \tag{A.14}$$

From equation A.14,

$$H(Y_i|Y^{i-1}) = H(Y_i|Y_{i-1}), \tag{A.15}$$

and together with equation A.7,

$$H(Y^n) = \sum_{i=1}^{n} H(Y_i|Y_{i-1}). \tag{A.16}$$

From equations A.6, A.11, and A.16,

$$I(X^n; Y^n) = \sum_{i=1}^{n} (H(Y_i|Y_{i-1}) - H(Y_i|Y_{i-1}, X_i)) \tag{A.17}$$

$$= \sum_{i=1}^{n} I(X_i; Y_i|Y_{i-1}). \tag{A.18}$$

We have

$$\begin{aligned} I(X_i; Y_i|Y_{i-1}) = {} & I(X_i; Y_i|Y_{i-1} = 0)P(Y_{i-1} = 0) \\ & + I(X_i; Y_i|Y_{i-1} = 1)P(Y_{i-1} = 1). \end{aligned} \tag{A.19}$$

Let

$$a_i \triangleq \begin{cases} P(Y_i = 0) & \text{if } i > 0 \\ 1 & \text{if } i = 0 \end{cases}. \tag{A.20}$$

From equations 3.7, 3.9, A.19, and A.20,

$$I(X_i; Y_i|Y_{i-1}) = r_1 a_{i-1} + r_2 \overline{a_{i-1}}. \tag{A.21}$$

By plugging equation A.21 into equation A.18,

$$
\begin{aligned}
I(X^n;Y^n) &= \sum_{i=1}^{n}(r_1 a_{i-1} + r_2 \overline{a_{i-1}}) \qquad \text{(A.22)} \\
&= n r_2 + (r_1 - r_2)\sum_{i=1}^{n} a_{i-1}. \qquad \text{(A.23)}
\end{aligned}
$$

We now derive a recurrence equation for a_i:

$$
\begin{aligned}
P(Y_i = 0) = {} & P(Y_i = 0 | Y_{i-1} = 0) P(Y_{i-1} = 0) \\
& + P(Y_i = 0 | Y_{i-1} = 1) P(Y_{i-1} = 1). \qquad \text{(A.24)}
\end{aligned}
$$

From Figure 1B,

$$
\begin{aligned}
P(Y_i = 0 | Y_{i-1} = 0) &= \overline{\alpha}\,\overline{q} + \alpha \overline{p} \qquad \text{(A.25)} \\
&= g_1 \qquad \text{(A.26)}
\end{aligned}
$$

and

$$
\begin{aligned}
P(Y_i = 0 | Y_{i-1} = 1) &= \overline{\alpha}\,\overline{dq} + \alpha \overline{cp} \qquad \text{(A.27)} \\
&= g_2. \qquad \text{(A.28)}
\end{aligned}
$$

By substituting these equations in A.24,

$$
a_i = (g_1 - g_2) a_{i-1} + g_2. \qquad \text{(A.29)}
$$

Defining

$$
\begin{aligned}
\lambda &\triangleq g_1 - g_2, \qquad \text{(A.30)} \\
\gamma &\triangleq g_2, \qquad \text{(A.31)}
\end{aligned}
$$

we find an inhomogeneous recurrence equation,

$$
\begin{aligned}
a_i &= \lambda a_{i-1} + \gamma, \qquad \text{(A.32)} \\
a_0 &= 1. \qquad \text{(A.33)}
\end{aligned}
$$

Let

$$
\begin{aligned}
\theta &= \frac{\gamma}{1 - \lambda} \qquad \text{(A.34)} \\
&= \frac{g_2}{\overline{g_1} + g_2}. \qquad \text{(A.35)}
\end{aligned}
$$

By defining a new variable, $b_i = a_i - \theta$, the inhomogeneous recurrence equation is converted to a homogeneous equation:

$$b_i = \lambda b_{i-1}, \tag{A.36}$$

$$b_0 = 1 - \theta. \tag{A.37}$$

The general solution of equation A.36 is

$$b_i = kw^i, \tag{A.38}$$

where k and w are constants. From equations A.36 to A.38,

$$w = \lambda, \tag{A.39}$$

$$k = 1 - \theta. \tag{A.40}$$

Therefore, the solution of the inhomogeneous equation is

$$a_i = (1-\theta)\lambda^i + \theta. \tag{A.41}$$

By plugging equation A.41 into A.23,

$$I(X^n; Y^n) = nr_2 + (r_1 - r_2)\sum_{i=1}^{n}((1-\theta)\lambda^{i-1} + \theta) \tag{A.42}$$

$$= nr_2 + (r_1 - r_2)(n\theta + (1-\theta)\frac{1-\lambda^n}{1-\lambda}). \tag{A.43}$$

□

Proof of Theorem 1. Using equation 2.11 and lemma 1,

$$r_D = \lim_{n\to\infty} \frac{1}{n} I(X^n; Y^n) \tag{A.44}$$

$$= \lim_{n\to\infty} \frac{1}{n}(nr_2 + (r_1 - r_2)(n\theta + (1-\theta)\frac{1-\lambda^n}{1-\lambda})) \tag{A.45}$$

$$= r_2 + (r_1 - r_2)\theta. \tag{A.46}$$

□

Proof of Corollary 1. From theorem 1,

$$r_D = \theta r_1 + (1-\theta)r_2, \tag{A.47}$$

which shows that the information rate is a weighted sum of the information rates of the recovered state and used state in Figure 1B. From equations A.20 and A.32,

$$\lim_{i\to\infty} P(Y_i = 0) = \lambda \lim_{i\to\infty} P(Y_{i-1} = 0) + \gamma. \tag{A.48}$$

Therefore,

$$\lim_{i\to\infty} P(Y_i = 0) = \frac{\gamma}{1-\lambda} \tag{A.49}$$

$$= \theta. \tag{A.50}$$

□

Lemma 2. *Suppose that in each release, one unit of energy is consumed by the presynaptic neuron. For the two-state model of depression, we have*

$$I_E(X^n; Y^n) = \frac{nr_2 + (r_1 - r_2)(n\theta + (1-\theta)\frac{1-\lambda^n}{1-\lambda})}{(1-\theta)(n - \lambda\frac{1-\lambda^n}{1-\lambda})}, \tag{A.51}$$

$$I_E^{(D)} = \frac{g_2 r_1 + \overline{g_1} r_2}{\overline{g_1}}. \tag{A.52}$$

Proof of Lemma 2. The probability of release at time i is $P(Y_i = 1)$. In each release, one unit of energy is consumed by the neuron,

$$E_i = P(Y_i = 1) \times 1, \tag{A.53}$$

and the total amount of energy consumed until the time n is

$$\sum_{i=1}^{n} E_i = \sum_{i=1}^{n} P(Y_i = 1). \tag{A.54}$$

From equations A.20 and A.41,

$$P(Y_i = 1) = 1 - a_i \tag{A.55}$$

$$= (1-\theta)(1-\lambda^i). \tag{A.56}$$

By plugging equation A.56 in A.54,

$$\sum_{i=1}^{n} E_i = (1-\theta)\left(n - \lambda\frac{1-\lambda^n}{1-\lambda}\right), \tag{A.57}$$

and together with lemma 1, equation A.51 is derived.

Moreover, from equations 3.20 and A.51,

$$I_E^{(D)} = \frac{\theta r_1 + (1-\theta) r_2}{1-\theta}, \tag{A.58}$$

and using equation A.3, the lemma is proved. □

Proof of Corollary 2. For the recovered state of the dynamic channel in Figure 1B,

$$E_i = P(Y_i = 1) \times 1 \tag{A.59}$$

$$= \overline{g_1}, \tag{A.60}$$

which proves equation 3.22.

We prove equation 3.23 in a similar way, and equation 3.24 follows from equations A.52, 3.22, and 3.23. □

Lemma 3. *If* $I_E^{(D)} < I_E^{(1)}$, *then*

$$I_E^{(2)} < I_E^{(1)}, \tag{A.61}$$

$$r_2 < r_1, \tag{A.62}$$

$$r_D < r_1. \tag{A.63}$$

The lemma remains valid if we substitute all the $<$ *signs with* $\leq$.

Proof of Lemma 3. From equation 3.24,

$$I_E^{(2)} = \frac{I_E^{(D)} - g_2 I_E^{(1)}}{\overline{g_2}} \tag{A.64}$$

$$< \frac{I_E^{(1)} - g_2 I_E^{(1)}}{\overline{g_2}} \tag{A.65}$$

$$= I_E^{(1)}. \tag{A.66}$$

Since $I_E^{(D)} < I_E^{(1)}$,

$$\frac{g_2 r_1 + \overline{g_1} r_2}{\overline{g_1}} < \frac{r_1}{\overline{g_1}}, \tag{A.67}$$

which implies

$$\overline{g_1} r_2 < \overline{g_2} r_1. \tag{A.68}$$

In the depression model, $dq < q$ and $cp < p$. Since $\overline{g_1} = \overline{\alpha}q + \alpha p$ and $\overline{g_2} = \overline{\alpha}dq + \alpha cp$, we have

$$\overline{g_2} \leq \overline{g_1}, \tag{A.69}$$

and equation A.62 follows from A.68 and A.69. Finally,

$$\begin{aligned} r_D &= \theta r_1 + (1-\theta)r_2 && \text{(A.70)}\\ &< \theta r_1 + (1-\theta)r_1 && \text{(A.71)}\\ &= r_1. && \text{(A.72)} \end{aligned}$$

The proof is also valid for the other variant of the lemma in which all the $<$ signs are substituted with $\leq$. ☐

Lemma 4. *Suppose f is a real continuous function on $[0, 1]$, twice differentiable on $(0, 1)$, $f(0) = 0$, $f(1) = 0$, and $\frac{d^2 f}{dx^2} < 0$ for all $x \in (0, 1)$. Then $f(x) > 0$ for all $x \in (0, 1)$.*

Proof of Lemma 4. We prove it by contradiction. Suppose that for some $x \in (0, 1)$, $f(x) \leq 0$. Two cases can happen.

Case 1: There exists $x_0 \in (0, 1)$, such that $f(x_0) < 0$.

Since f is continuous on $[0, 1]$, from the extreme value theorem, f attains its minimum value on the interval $[0, 1]$. Thus, there exists $x_1 \in [0, 1]$ such that $f(x_1) \leq f(x)$ for all $x \in [0, 1]$. In particular,

$$\begin{aligned} f(x_1) &\leq f(x_0) && \text{(A.73)}\\ &< 0, && \text{(A.74)} \end{aligned}$$

and since $f(0) = f(1) = 0$, we have $x_1 \in (0, 1)$. From Fermat's theorem for stationary points (Rudin, 1964),

$$\frac{df}{dx}(x_1) = 0, \tag{A.75}$$

where $\frac{df}{dx}(x_1)$ stands for the first derivative of f at x_1.

Since $\frac{d^2 f}{dx^2}(x_1) < 0$ and $\frac{df}{dx}(x_1) = 0$, from theorem 8.32 in Shilov and Šilov (1996), $f(x_1)$ is a local maximum of f. However, based on the definition, x_1 is also a local minimum. The only possibility is that f is constant in a neighborhood of x_1. But this contradicts $\frac{d^2 f}{dx^2}(x_1) < 0$.

Case 2: $f(x) \geq 0$ for all $x \in (0, 1)$, and there exists $x_0 \in (0, 1)$ such that $f(x_0) = 0$.

In this case, f has a local minimum at x_0 and the same argument can be used to show the contradiction. ☐

Proof of Theorem 2. The hypothesis $c = d$ together with equation A.5 implies

$$\overline{g_2} = \overline{\alpha} dq + \alpha cp \tag{A.76}$$

$$= \overline{\alpha} dq + \alpha dp \tag{A.77}$$

$$= d\overline{g_1}. \tag{A.78}$$

We use equations A.52, 3.22, and A.78 to derive the following equivalency:

$$I_E^{(D)} \leq I_E^{(1)} \iff \overline{g_1} r_2 \leq \overline{g_2} r_1 \tag{A.79}$$

$$\iff r_2 \leq d r_1. \tag{A.80}$$

Therefore, instead of proving $I_E^{(D)} \leq I_E^{(1)}$, we define

$$\Delta = d r_1 - r_2 \tag{A.81}$$

and prove that $\Delta \geq 0$.

For given values of d, p, and q, we consider Δ as a function of α. Since r_1 and r_2 are zero at $\alpha = 0$ and $\alpha = 1$,

$$\Delta(\alpha = 0) = 0, \tag{A.82}$$

$$\Delta(\alpha = 1) = 0. \tag{A.83}$$

From equations 3.8 and 3.10,

$$r_1 = h(\overline{\alpha} q + \alpha p) - \overline{\alpha} h(q) - \alpha h(p), \tag{A.84}$$

$$r_2 = h(\overline{\alpha} dq + \alpha d\, p) - \overline{\alpha} h(dq) - \alpha h(dp). \tag{A.85}$$

Also, for $x \in (0, 1)$,

$$\frac{dh}{dx} = \log_2\left(\frac{1-x}{x}\right). \tag{A.86}$$

Therefore,

$$\frac{\partial^2 \Delta}{\partial \alpha^2} = d\frac{\partial^2 r_1}{\partial \alpha^2} - \frac{\partial^2 r_2}{\partial \alpha^2} \tag{A.87}$$

$$= -k\left(\frac{1}{1-(\overline{\alpha} q + \alpha p)} - \frac{d}{1-d(\overline{\alpha} q + \alpha p)}\right) \tag{A.88}$$

$$= -k \frac{(1-d)}{(1-\overline{g_1})(1-d\overline{g_1})}, \tag{A.89}$$

where

$$k = \frac{(p-q)^2}{(\overline{\alpha}q + \alpha p).\ln 2}. \tag{A.90}$$

In our model, $q < p$, which implies that k is strictly greater than zero. Since $d < 1, \overline{g_1} < 1$, and $k > 0$,

$$\frac{\partial^2 \Delta}{\partial \alpha^2} < 0. \tag{A.91}$$

From equations A.82,A.83, A.91 and lemma 4,

$$\Delta \geq 0, \tag{A.92}$$

for all values of α, d, p and q. This proves equation 3.25, and together with lemma 3, we have

$$r_D \leq r_1. \tag{A.93}$$

□

Lemma 5. *If w is defined as*

$$w \triangleq h(\alpha p) - h(\overline{\alpha}q + \alpha p) + \overline{\alpha}h(q), \tag{A.94}$$

then $w > 0$, for all values of q, p and $\alpha \in (0, 1)$.

Proof. We consider w as a function of α:

$$w(\alpha = 0) = 0, \tag{A.95}$$

$$w(\alpha = 1) = 0. \tag{A.96}$$

We have

$$\frac{\partial^2 w}{\partial \alpha^2} = \frac{qpL}{(\overline{\alpha}q + \alpha p)(1 - \overline{\alpha}q - \alpha p)(\alpha p)(1 - \alpha p)}, \tag{A.97}$$

where

$$L = \overline{\alpha}(-1 + q + 3\overline{p} - 2\overline{p}^2 - 2q\overline{p}) - 2\overline{p} + q\overline{p} + 2\overline{p}^2. \tag{A.98}$$

We consider L as a function of α,

$$L(\alpha = 1) = \overline{p}(q - 2p). \tag{A.99}$$

Since $q < p$,

$$L(\alpha = 1) < 0. \tag{A.100}$$

Also,

$$L(\alpha = 0) = p(q - 1) \tag{A.101}$$

$$< 0. \tag{A.102}$$

Since L is a linear function of α and it is negative at $\alpha = 0$ and $\alpha = 1$,

$$L < 0, \tag{A.103}$$

for all values of α.

The denominator of equation A.97 is positive for all $\alpha \in (0, 1)$ because $0 < \overline{g_1} = \overline{\alpha}q + \alpha p < 1$ and $0 < \alpha p < 1$. Also from equation A.103, the nominator of A.97 is always negative. Therefore,

$$\frac{\partial^2 w}{\partial \alpha^2} < 0 \tag{A.104}$$

for all $\alpha \in (0, 1)$. Using lemma 5 for w completes the proof. □

Lemma 6. *Let v be defined as*

$$v \triangleq h(\overline{\alpha}dq + \alpha p) - \overline{\alpha}h(dq) - h(\overline{\alpha}q + \alpha p) + \overline{\alpha}h(q). \tag{A.105}$$

For all values of $p, q, \alpha \in (0, 1)$, and $d \in [0, 1)$, we have $v > 0$.

Proof. We consider v as a function of d.

$$v(d = 0) = w, \tag{A.106}$$

and from lemma 5, for all values of p, q, and $\alpha \in (0, 1)$,

$$v(d = 0) > 0. \tag{A.107}$$

Also

$$v(d = 1) = 0. \tag{A.108}$$

We prove that v is strictly decreasing on the interval $[0, 1)$:

$$\frac{\partial v}{\partial d} = \overline{\alpha} q \log \frac{(1 - \overline{\alpha} dq - \alpha p) dq}{(\overline{\alpha} dq + \alpha p)(1 - dq)}. \tag{A.109}$$

We have the following equivalencies,

$$\frac{\partial v}{\partial d} < 0 \iff \frac{(1 - \overline{\alpha} dq - \alpha p) dq}{(\overline{\alpha} dq + \alpha p)(1 - dq)} < 1 \tag{A.110}$$

$$\iff dq < \overline{\alpha} dq + \alpha p \tag{A.111}$$

$$\iff dq < p. \tag{A.112}$$

The inequalities $q < p$ and $d < 1$ imply that $dq < p$. Therefore,

$$\frac{\partial v}{\partial d} < 0. \tag{A.113}$$

From equations A.107, A.108, and A.113, it follows that $v > 0$ for all values of $d \in [0, 1)$. □

Proof of Theorem 3. We define the function Δ as

$$\Delta \triangleq r_2 - r_1. \tag{A.114}$$

From equations 3.8 and 3.10,

$$\Delta = h(\overline{\alpha} dq + \alpha cp) - \overline{\alpha} h(dq) - \alpha h(cp) - h(\overline{\alpha} q + \alpha p) + \overline{\alpha} h(q) + \alpha h(p). \tag{A.115}$$

Consider Δ as a function of c. If $c = d$, then from theorem 3, $r_D \leq r_1$. Also from equation A.70, $r_D \leq r_1$ if and only if $r_2 \leq r_1$. Therefore

$$\Delta(c = d) \leq 0. \tag{A.116}$$

From equation A.105,

$$\Delta(c = 1) = v, \tag{A.117}$$

and lemma 6 implies that

$$\Delta(c = 1) > 0. \tag{A.118}$$

We now prove that Δ is a strictly increasing function of c in the interval $[d, 1]$:

$$\frac{\partial \Delta}{\partial c} = \alpha p \log \frac{(1 - \overline{\alpha} dq - \alpha cp)cp}{(\overline{\alpha} dq + \alpha cp)(1 - cp)}. \tag{A.119}$$

We have the following equivalencies:

$$\frac{\partial \Delta}{\partial c} > 0 \iff \frac{(1 - \overline{\alpha} dq - \alpha cp)cp}{(\overline{\alpha} dq + \alpha cp)(1 - cp)} > 1 \tag{A.120}$$

$$\iff cp > \overline{\alpha} dq + \alpha cp \tag{A.121}$$

$$\iff cp > dq. \tag{A.122}$$

From equation 2.5,

$$\frac{\partial \Delta}{\partial c} > 0, \tag{A.123}$$

for $c \in (d, 1)$. From equations A.116, A.118, and A.123, we infer that there exists c_0, $d \leq c_0 < 1$, such that $\Delta(c = c_0) = 0$ and for $c > c_0$, $\Delta(c) > 0$. From equation A.70, $r_2 > r_1$ if and only if $r_D > r_1$. Therefore,

$$r_D > r_1, \tag{A.124}$$

for $c > c_0$. Finally, it follows from lemma 3 and equation A.124 that $I_E^{(D)} > I_E^{(1)}$ for $c > c_0$. □

Acknowledgments

This work was supported by the BMBF grant 01EO1401 (German Center for Vertigo and Balance Disorders). We thank the reviewers for their insightful remarks and suggestions.

References

Arleo, A., Nieus, T., Bezzi, M., D'Errico, A., D'Angelo, E., & Coenen, O. J.-M. (2010). How synaptic release probability shapes neuronal transmission: Information-theoretic analysis in a cerebellar granule cell. *Neural Computation*, *22*(8), 2031–2058.

Attwell, D., & Laughlin, S. B. (2001). An energy budget for signaling in the grey matter of the brain. *Journal of Cerebral Blood Flow and Metabolism*, *21*(10), 1133–1145.

Balasubramanian, V., Kimber, D., & Berry II, M. J. (2001). Metabolically efficient information processing. *Neural Computation*, *13*(4), 799–815.

Biró, Á. A., Holderith, N. B., & Nusser, Z. (2005). Quantal size is independent of the release probability at hippocampal excitatory synapses. *Journal of Neuroscience*, *25*(1), 223–232.

Bliss, T. V., & Lømo, T. (1973). Long-lasting potentiation of synaptic transmission in the dentate area of the anaesthetized rabbit following stimulation of the perforant path. *Journal of Physiology*, *232*(2), 331–356.

Branco, T., & Staras, K. (2009). The probability of neurotransmitter release: Variability and feedback control at single synapses. *Nature Reviews Neuroscience*, *10*(5), 373–383.

Cho, S., Li, G.-L., & Von Gersdorff, H. (2011). Recovery from short-term depression and facilitation is ultrafast and CA2+ dependent at auditory hair cell synapses. *Journal of Neuroscience*, *31*(15), 5682–5692.

Clarke, G. L., Chen, J., & Nishimune, H. (2012). Presynaptic active zone density during development and synaptic plasticity. *Frontiers in Molecular Neuroscience*, *5*.

Cortes, J. M., Marinazzo, D., Series, P., Oram, M. W., Sejnowski, T. J., & Van Rossum, M. C. (2012). The effect of neural adaptation on population coding accuracy. *Journal of Computational Neuroscience*, *32*(3), 387–402.

Cover, T. M., & Thomas, J. A. (2012). *Elements of information theory*. New York: Wiley.

Dan, Y., & Poo, M.-m. (2004). Spike timing-dependent plasticity of neural circuits. *Neuron*, *44*(1), 23–30.

Del Castillo, J., & Katz, B. (1954). Quantal components of the end-plate potential. *Journal of Physiology*, *124*(3), 560–573.

Dobrunz, L. E., Huang, E. P., & Stevens, C. F. (1997). Very short-term plasticity in hippocampal synapses. *Proceedings of the National Academy of Sciences*, *94*(26), 14843–14847.

Eccles, J. C., Katz, B., & Kuffler, S. W. (1941). Nature of the endplate potential in curarized muscle. *Journal of Neurophysiology*, *4*(5), 362–387.

Foster, M., & Sherrington, C. S. (1897). *The central nervous system*, vol. 3. New York: Macmillan.

Fredj, N. B., & Burrone, J. (2009). A resting pool of vesicles is responsible for spontaneous vesicle fusion at the synapse. *Nature Neuroscience*, *12*(6), 751–758.

Friston, K. (2010). The free-energy principle: A unified brain theory? *Nature Reviews Neuroscience*, *11*(2), 127–138.

Fuhrmann, G., Segev, I., Markram, H., & Tsodyks, M. (2002). Coding of temporal information by activity-dependent synapses. *Journal of Neurophysiology*, *87*(1), 140–148.

Gil, Z., Connors, B. W., & Amitai, Y. (1999). Efficacy of thalamocortical and intracortical synaptic connections: Quanta, innervation, and reliability. *Neuron*, *23*(2), 385–397.

Goldman, M. S. (2004). Enhancement of information transmission efficiency by synaptic failures. *Neural Computation*, *16*(6), 1137–1162.

Hallermann, S., & Silver, R. A. (2013). Sustaining rapid vesicular release at active zones: Potential roles for vesicle tethering. *Trends in Neurosciences*, *36*(3), 185–194.

Hanse, E., & Gustafsson, B. (2001). Paired-pulse plasticity at the single release site level: An experimental and computational study. *Journal of Neuroscience*, *21*(21), 8362–8369.

Jiao, J., Permuter, H. H., Zhao, L., Kim, Y.-H., & Weissman, T. (2013). Universal estimation of directed information. *IEEE Transactions on Information Theory*, *59*(10), 6220–6242.

Kavalali, E. T. (2015). The mechanisms and functions of spontaneous neurotransmitter release. *Nature Reviews Neuroscience*, *16*(1), 5–16.

Korn, H., Triller, A., Mallet, A., & Faber, D. S. (1981). Fluctuating responses at a central synapse: *n* of binomial fit predicts number of stained presynaptic boutons. *Science*, *213*(4510), 898–901.

Levy, W. B., and Baxter, R. A. (1996). Energy efficient neural codes. *Neural Computation*, *8*(3), 531–543.

Levy, W. B., & Baxter, R. A. (2002). Energy-efficient neuronal computation via quantal synaptic failures. *Journal of Neuroscience*, *22*(11), 4746–4755.

London, M., Larkum, M. E., & Häusser, M. (2008). Predicting the synaptic information efficacy in cortical layer 5 pyramidal neurons using a minimal integrate-and-fire model. *Biological Cybernetics*, *99*(4–5), 393–401.

London, M., Schreibman, A., Häusser, M., Larkum, M. E., & Segev, I. (2002). The information efficacy of a synapse. *Nature Neuroscience*, *5*(4), 332–340.

Manwani, A., & Koch, C. (2001). Detecting and estimating signals over noisy and unreliable synapses: Information-theoretic analysis. *Neural Computation*, *13*(1), 1–33.

Markram, H., Lübke, J., Frotscher, M., & Sakmann, B. (1997). Regulation of synaptic efficacy by coincidence of postsynaptic APS and EPSPS. *Science*, *275*(5297), 213–215.

Markram, H., & Tsodyks, M. (1996). Redistribution of synaptic efficacy between neocortical pyramidal neurons. *Nature*, *382*, 807–810.

Melom, J. E., Akbergenova, Y., Gavornik, J. P., & Littleton, J. T. (2013). Spontaneous and evoked release are independently regulated at individual active zones. *Journal of Neuroscience*, *33*(44), 17253–17263.

Nelson, S. B., Sjöström, P. J., & Turrigiano, G. G. (2002). Rate and timing in cortical synaptic plasticity. *Philosophical Transactions of the Royal Society B: Biological Sciences*, *357*(1428), 1851–1857.

Neymotin, S. A., Jacobs, K. M., Fenton, A. A., & Lytton, W. W. (2011). Synaptic information transfer in computer models of neocortical columns. *Journal of Computational Neuroscience*, *30*(1), 69–84.

Niven, J. E., Anderson, J. C., & Laughlin, S. B. (2007). Fly photoreceptors demonstrate energy-information trade-offs in neural coding. *PLoS Biology*, *5*(4), e116.

Rangan, A. V. (2012). Functional roles for synaptic-depression within a model of the fly antennal lobe. *PLoS Computational Biology*, *8*(8), e1002622.

Rosenbaum, R., Rubin, J., & Doiron, B. (2012). Short term synaptic depression imposes a frequency dependent filter on synaptic information transfer. *PLoS Computational Biology*, *8*, e1002557.

Rudin, W. (1964). *Principles of mathematical analysis*, vol. 3. New York: McGraw-Hill.

Sacramento, J., Wichert, A., & van Rossum, M. C. (2015). Energy efficient sparse connectivity from imbalanced synaptic plasticity rules. *PLoS Computational Biology*, *11*(6), e1004265.

Scott, P., Cowan, A. I., & Stricker, C. (2012). Quantifying impacts of short-term plasticity on neuronal information transfer. *Physical Review E*, *85*(4), 041921.

Sengupta, B., Laughlin, S. B., & Niven, J. E. (2013). Balanced excitatory and inhibitory synaptic currents promote efficient coding and metabolic efficiency. *PLoS Computational Biology*, *9*(10), e1003263.

Sengupta, B., Stemmler, M. B., & Friston, K. J. (2013). Information and efficiency in the nervous system—a synthesis. *PLoS Computational Biology*, *9*(7), e1003157.

Sengupta, B., Stemmler, M., Laughlin, S. B., & Niven, J. E. (2010). Action potential energy efficiency varies among neuron types in vertebrates and invertebrates. *PLoS Computational Biology*, *6*(7), e1000840.

Shilov, G. E., & Šilov, G. E. (1996). *Elementary real and complex analysis*. Mineola, NY: Dover Publications.

Silver, R. A., Lübke, J., Sakmann, B., & Feldmeyer, D. (2003). High-probability uniquantal transmission at excitatory synapses in barrel cortex. *Science*, *302*(5652), 1981–1984.

Vembu, S., Verdù, S., & Steinberg, Y. (1995). The source-channel separation theorem revisited. *IEEE Transactions on Information Theory*, *41*(1), 44–54.

Walter, A. M., Haucke, V., & Sigrist, S. J. (2014). Neurotransmission: Spontaneous and evoked release filing for divorce. *Current Biology*, *24*(5), R192–R194.

Wang, Y., & Manis, P. B. (2008). Short-term synaptic depression and recovery at the mature mammalian endbulb of held synapse in mice. *Journal of Neurophysiology*, *100*(3), 1255–1264.

Wang, Y., Markram, H., Goodman, P. H., Berger, T. K., Ma, J., & Goldman-Rakic, P. S. (2006). Heterogeneity in the pyramidal network of the medial prefrontal cortex. *Nature Neuroscience*, *9*(4), 534–542.

Yusim, K., Parnas, H., & Segel, L. (2001). One-vesicle hypothesis for neurotransmitter release: A possible molecular mechanism. *Bulletin of Mathematical Biology*, *63*(6), 1025–1040.

Zador, A. (1998). Impact of synaptic unreliability on the information transmitted by spiking neurons. *Journal of Neurophysiology*, *79*(3), 1219–1229.

Zucker, R. S., & Regehr, W. G. (2002). Short-term synaptic plasticity. *Annual Review of Physiology*, *64*(1), 355–405.

Received August 12, 2016; accepted January 17, 2017.

Chapter 3

Information efficacy of a depressing synapse

3.1 Summary

In Chapter 2, we modeled a depressing synapse using two communication channels corresponding to the used state and the normal state. The simplicity of the two-state model permitted an analytical calculation of the regimes of synaptic parameters in which depression enhances/degrades the information efficacy of the synapse. The two-state model, however, does not capture the gradual fatigue and exponential recovery of short-term depression.

We extend the synapse model to a communication channel with memory. The content of the memory is the release history of the synapse and determines the state of the channel. We first show that our model emulates the dynamics of short-term depression precisely. Then we calculate the information rate of the synapse analytically and derive a closed-form expression for the rate of information transmission.

The energetic cost of synaptic release is high and the neurons need to compromise between the rate of information transmission and the energy consumption. To study the energy-rate trade-off of the synapse, we assume that one unit of energy is consumed for each release and calculate the energy-normalized information rate. The energy-rate analysis shows how short-term depression modulates the information efficacy of a synapse with a limited energy budget.

3.2 Contributions

The contributions of the authors Mehrdad Salmasi (MS), Alex Loebel (AL), Stefan Glasauer (SG) and, Martin B. Stemmler (MBS) are as follows: MS, AL, SG and

MBS designed the study and developed the model. MS analyzed the model and performed the simulations. MS, AL, SG and MBS interpreted the results and wrote the manuscript.

The following manuscript is ready for submission:

- M. Salmasi, A. Loebel, S. Glasauer, M. Stemmler, “Short-Term Synaptic Depression Can Increase the Rate of Information Transfer at a Release Site”, to be submitted.

The preliminary results of this study were presented as abstracts and posters in the Bernstein (2016) and SfN (2016) conferences:

- M. Salmasi, A. Loebel, S. Glasauer, M. Stemmler, “Information Rate of a Release Site under Short-term Synaptic Depression”, Bernstein Conference on Computational Neuroscience (BCCN), Berlin, September 2016.
- M. Salmasi, A. Loebel, S. Glasauer, M. Stemmler, “Short-Term Synaptic Depression Can Increase the Information Rate at a Release Site”, 46th Annual Meeting of the Society for Neuroscience (SfN), San Diego, November 2016.

Short-term synaptic depression can increase the rate of information transfer at a release site

Mehrdad Salmasi[a,c], Alex Loebel[b,d], Stefan Glasauer[a,b,c,e], Martin Stemmler[b,d]

[a] *Graduate School of Systemic Neurosciences, Ludwig-Maximilian University, Munich, Germany*
[b] *Bernstein Center for Computational Neuroscience, Munich, Germany*
[c] *German Center for Vertigo and Balance Disorders, Ludwig-Maximilian University, Munich, Germany*
[d] *Department of Biology II, Ludwig-Maximilian University, Munich, Germany*
[e] *Department of Neurology, Ludwig-Maximilian University, Munich, Germany*

Abstract

The release of neurotransmitters from synapses follows complex and stochastic dynamics. Depending on the recent history of synaptic activation, many synapses depress their release probability. Our understanding of the information efficacy of such synapses, however, is limited. Here we propose a mathematically tractable model of both spike-evoked and spontaneous release to analyze the impact of synaptic depression on the information conveyed by a synapse. The model transits between discrete states of a communication channel, with the present state depending on many past time steps. This history dependence enables such a model to emulate the gradual depression and exponential recovery of the synapse.

Spontaneous release plays a critical role in shaping the information efficacy of the synapse. We prove that depression can enhance both the information rate and the information rate per unit energy expended, provided that spike-evoked release depresses less (or recovers faster) than the spontaneous release. We derive several consequences for metaplasticity of short-term synaptic depression. Although the information rate of the synapse varies considerably for different dynamics of short-term depression, we show that the energy-normalized information rate is robust to variations in the parameters governing the depression dynamics. As a consequence, for a fixed arrival rate of presynaptic spikes, a synapse can adjust its energy expenditure by changing the dynamics of short-term synaptic depression without affecting the net information conveyed by each successful release. Moreover, the optimal input spike rate is independent of the amplitude or time constant of synaptic depression; instead, the ideal input rate only depends on the ratio between spontaneous and evoked release probabilities. As long as this ratio remains constant, a synapse could adapt its properties while continuing to work at the optimal operating point.

Keywords: Short-term synaptic depression, release site, information theory, binary asymmetric channel, mutual information rate, metaplasticity.

Author Summary

Fatigue is an intrinsic property of living systems and synapses are no exception. Synaptic fatigue or synaptic depression reduces the ability of synapses to release vesicles in response to an incoming action potential. Whether synaptic depression simply reflects the exhaustion of neuronal resources or whether it serves some additional function is still an open question. There are several hypotheses on the role of synaptic depression. One key hypothesis is that it modulates the information transfer between neurons by keeping the synapse in an appropriate operating range. In this study, we use communication channels to model synaptic transmission and study information transmission through a depressing synapse. This model captures both spontaneous and evoked release events; the probability of both events is determined by depression dynamics. Our approach leads to a closed-form expression for the mutual information rate. With this result, we can answer the question whether depression enhances or impairs information transfer: it depends on the relative level of depression for spontaneous and spike-evoked releases. We also study the compromise a synapse makes between its energy consumption and the rate of information transmission. Interestingly, we show that the transmitted information per unit energy is independent of the synapse's depression dynamics.

1. Introduction

Chemical synapses are the main conduits of information in the nervous system [1]. At such synapses, a pre-synaptic action potential induces docked vesicles, packed with neurotransmitters, to release with a certain probability. A vesicle release leads to a local post-synaptic dendritic voltage fluctuation, which, in turn, can lead to the generation or inhibition of a post-synaptic action potential, depending on whether the synapse is excitatory or inhibitory [2]. Due to the stochastic nature of vesicle release, a release failure may occur upon the arrival of an action-potential; and alternatively, a spontaneous release can occur even without an action-potential [3]. In addition, at many synaptic connections, the release probability is not constant, but exhibits short-term dynamics on time scales of tens to hundreds of milliseconds [4–7]. The prevalent dynamics consists of short-term depression, in which the release probability instantaneously decrease upon vesicle release, and gradually recovers back during quiescent periods [8, 9]. Several hypotheses have been suggested for the functional role of short-term depression, such as temporal filtering of pre-synaptic spike trains [10, 11], decorrelation and compression of inputs [12], adaptation to identical stimuli [13], and regulation of information transfer [14, 15].

In particular, the rate of information transfer at a synapse is an essential measure of its efficacy. Synaptic information efficacy has been studied numerically [15–17], its capacity bounded analytically [18], and, in combination with numerical methods, some approximations of the information rate have been derived [19, 20]. However, the complexity and dynamics of synaptic transmission have forced the use of elaborate models for information transmission and have proved to be an obstacle to the derivation of a closed form expression for synaptic information efficacy. Furthermore, the energy-efficiency of information transfer at synapses has yet to be studied analytically. Stronger depression and slower recovery reduce both the use of metabolic energy and the release probability, so the parameters of depression tune the information-energy trade-off in neurons [21]. Moreover, it remains elusive how the stochastic properties of the synapse, in particular spontaneous release, modulate the energy-information regime of the synapse.

To address these issues, we present a tractable, mathematical multi-state model for short-term depression at a single release site. The stochastic relation between spikes and synaptic releases is represented by a binary asymmetric channel for each state. The model allows us to distinguish between the two synaptic release mechanisms, namely spike-evoked and spontaneous release; and the current state (release probability) of the channel is determined by the release history. Building upon an earlier model [22], the introduction of multiple states allows the present model to capture the gradual recovery of the site after a release, and thus connects to classic models of depression based on differential equations [20].

Using this model, we derive analytical closed-from expression for the mutual information rate of the release site under depression. We also consider the energy consumption of the synapse and calculate the energy-normalized information rate of the release site. We study the impact of depression parameters on the information rate and information-energy compromise of the synapse. Our findings clarify how the level of depression and the recovery time constant modulate the information rate of the release site. We subsequently assess the impact of spontaneous release on the information rate of a synapse during short-term depression. The joint analysis of short-term depression and spontaneous release reveals the modulatory impact of stochastic features of the synapse on the functional role of depression. Our results present a new categorization for synapses which is based on the increase/decrease of information rate and energy-normalized information rate of the synapse during short-term depression.

2. Model and analytical results

We model a single release site by a binary asymmetric channel with memory (Fig. 1A). The input of the channel is the pre-synaptic spike train, a Poisson process which is modeled by a sequence of independent Bernoulli random variables, $X = \{X_i\}_{i=1}^{n}$. The random variable X_i corresponds to the presence ($X_i = 1$) or

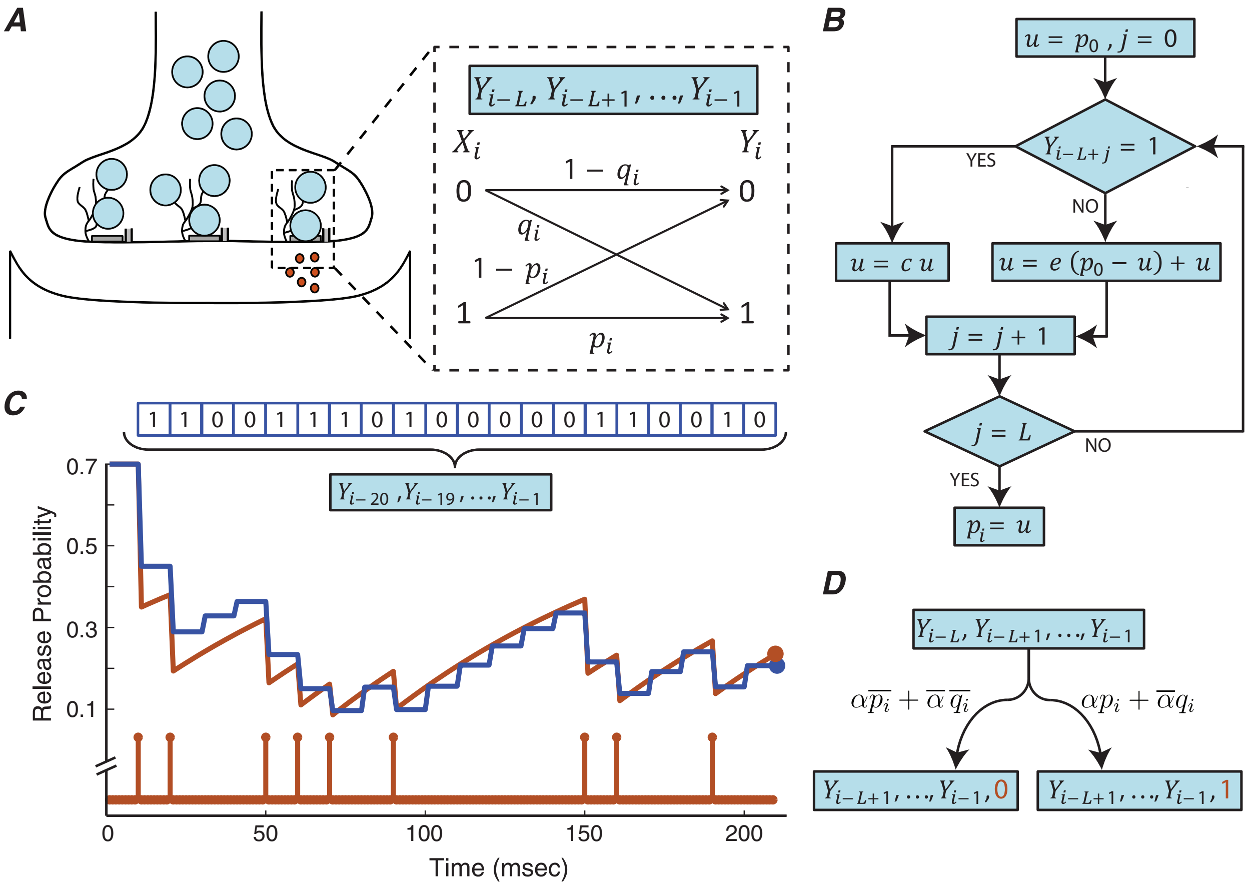

Figure 1: (A) A binary asymmetric channel with a finite memory is used to model the release site under short-term depression. The spike-evoked release probability, p_i, and the spontaneous release probability, q_i, are determined based on the previous L release outcomes of the release site. (B) The algorithm for calculating the spike-evoked release probability, p_i, given the last L release outcomes, $(Y_{i-L}, Y_{i-L+1}, ..., Y_{i-1})$. The spontaneous release probability, q_i, can be derived similarly by substituting c, e and p with d, f and q respectively. We assume that the model parameters $(\alpha, c, d, e, f, p_0, q_0)$ are strictly greater than zero and less than one . (C) The performance of the algorithm is compared with the stochastic model of depression [20]. The stochastic model is based on the differential equation $\frac{dp_r}{dt} = \frac{p_0 - p_r}{\tau} - up_r\delta(t - t_r)$, where $p_r, \tau, p_0, u,$ and t_r are the release probability, recovery time constant, default (maximum) release probability, depression coefficient and the release timing. At the bottom of the panel, the orange stem plot shows the timing of the release, t_r, during an interval of 200 msec. The orange line demonstrates the release probability, p_r, calculated from the differential equation. By assuming a time unit of $\Delta = 10$ msec for the MRO model, the 200 msec interval corresponds to a memory of length $L = 20$. The memory content of the model is shown at the top of the panel. The blue line demonstrates the release probability calculated from the algorithm in (B). The final values of the release probability are indicated by filled circles. (D) Every arbitrary state of the release site can transit to two other states, depending on the release outcome. The transition probabilities are shown on the transition links.

absence $(X_i = 0)$ of the spike at time i, with $\alpha = P(X_i = 1)$ representing the input spike rate. The output of the channel, $Y = \{Y_i\}_{i=1}^{n}$, is the release outcome of the release site. If a vesicle is released at time i, then $Y_i = 1$ and otherwise $Y_i = 0$. The two release mechanisms of the synapse, spike-evoked and spontaneous release, are modeled by transitions from $X_i = 1$ and $X_i = 0$ to $Y_i = 1$, and the transition probabilities p_i and q_i are called the spike-evoked and spontaneous release probabilities.

We use a memory of the last L release outcomes of the channel to implement the short-term depression in our model. The release probabilities of the release site, p_i and q_i, are determined by,

$$p_i = p_i(Y_{i-L}, Y_{i-L+1}, ..., Y_{i-2}, Y_{i-1}), \tag{1}$$

$$q_i = q_i(Y_{i-L}, Y_{i-L+1}, ..., Y_{i-2}, Y_{i-1}). \tag{2}$$

After each successful release, the spike-evoked and spontaneous release probabilities decrease to a fraction of their earlier values. This fraction is represented by the multiplier c or d, depending on the type of release. In quiescent intervals, in which no vesicle is released, the release probabilities gradually recover back to their default values (p_0 and q_0) with recovery coefficients e and f. The algorithm in Fig. 1B describes how the spike-evoked release probability, p_i, is calculated from the release site's history $(Y_{i-L}, Y_{i-L+1}, ..., Y_{i-2}, Y_{i-1})$. The spontaneous release probability, q_i, is independently parameterized by the depression multiplier e and the recovery coefficient f. The interval between two discrete time indices i and $i+1$ is called the time unit of the model and is represented by Δ. Throughout this paper, we set $\Delta = 10$ msec. The biological interpretation of Δ, as well as the other model parameters, is discussed in more details in Appendix C. Our model can reproduce the depression and recovery dynamics of the release site and is consistent with the probabilistic models of synaptic depression [20] (Fig. 1C). Throughout this paper, we refer to the model as the binary asymmetric channel with a Memory of Release Outcomes, abbreviated by MRO.

To study the synaptic information efficacy of the release site under depression, we use information-theoretic measures (please see Appendix A for an overview). The information rate of the release site is derived by calculating the mutual information between the pre-synaptic input spike train, X, and the release outcome process of the release site Y.

The release site in the MRO model can be in any one of 2^L states. Let j, $0 \leq j \leq 2^L - 1$, be an arbitrary state of the release site with spike-evoked and spontaneous release probabilities $p(j)$ and $q(j)$. It can be easily shown that the mutual information rate of the binary asymmetric channel at state j, denoted by R_j, is equal to

$$R_j = h\big(\overline{\alpha}q(j) + \alpha p(j)\big) - \overline{\alpha}h\big(q(j)\big) - \alpha h\big(p(j)\big), \tag{3}$$

where $\overline{\alpha} = 1 - \alpha$ and $h(x) = -x \log_2(x) - \overline{x} \log_2(\overline{x})$.

Each state of the release site can transit to two other states, depending on the release outcome (Fig. 1D). The state transitions of the release site are modeled by a Markov chain with 2^L states (e.g., Fig. 2 shows the Markov chain for the case of $L = 2$). We prove that regardless of the initial state, the probability of each state j converges to a stationary probability π_j. The stationary probabilities are calculated using the power iteration method [23]. The next theorem provides a closed-form expression for the information rate of the release site.

Theorem 1. *Let R_D be the mutual information rate of the release site with short-term depression. Then*

$$R_D = \sum_{j=0}^{2^L-1} R_j \pi_j. \tag{4}$$

This theorem shows that the mutual information rate of the release site is equal to the statistical average over the information rates of its constituent states. Therefore, the rate of every release profile has a linear share in the information rate of the release site; the share is determined by the occurrence probability of the profile. This theorem is an extension of the result that we derived for a two-state model of depression (equivalent to $L = 1$) [22]. All the proofs are found in Appendix D.

The brain uses more energy on synaptic transmission than on any other process [24]. To gain a better understanding of the trade-off between the energy consumption and information rate in a synapse during short-term depression, we consider the energy cost of synaptic release and derive the energy-normalized information rate of the release site. The energy-normalized information rate is calculated by dividing the mutual information (between the input and output processes) of the release site by the total amount of energy that is consumed for synaptic release. This measure quantifies the amount of information that can be transferred through the release site for one unit of energy (see Appendix A for the mathematical formulation of these concepts).

The next theorem gives a simple expression for calculating the energy-normalized information rate of the release site.

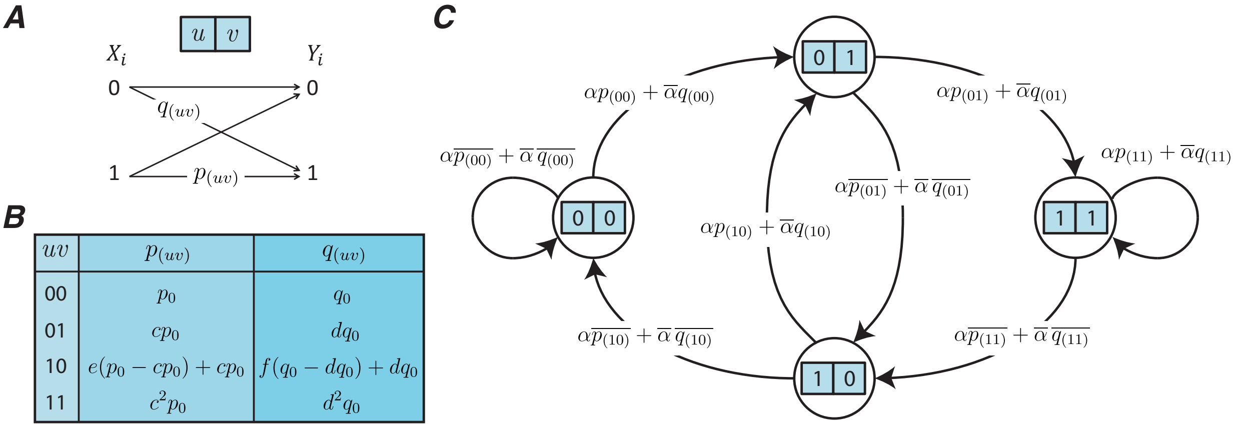

uv	$p_{(uv)}$	$q_{(uv)}$
00	p_0	q_0
01	cp_0	dq_0
10	$e(p_0 - cp_0) + cp_0$	$f(q_0 - dq_0) + dq_0$
11	$c^2 p_0$	$d^2 q_0$

Figure 2: An example of the MRO model. (A) The binary asymmetric channel with a memory of length $L = 2$. (B) The table of release probabilities for every possible release outcome. The spike-evoked and spontaneous release probabilities are calculated from the Algorithm in Fig. 1B. (C) The Markov chain model representing the transitions between the $2^L = 4$ states of the model. The transition probabilities are calculated using the values in table (B) and the rule given in Fig. 1D.

Theorem 2. *Assume that the neuron consumes one unit of energy for each vesicle release. If we denote the energy-normalized information rate of the release site under depression by* $R_D^{(E)}$*, then*

$$R_D^{(E)} = \frac{\sum_{j=0}^{2^L-1} R_j \pi_j}{\sum_{j=0}^{2^{(L-1)}-1} \pi_{2j+1}}. \tag{5}$$

The energy normalized information rate, $R_D^{(E)}$, can be used to evaluate the compromise between the rate of information transfer and the energy consumption of the synapse.

We derived the mutual information rate and energy-normalized information rate of a synapse with depression in Theorem 1 and Theorem 2. For a synapse without depression, we can use the same theorems to calculate the corresponding information rates.

Corollary 1. *Let* R_0 *and* $R_0^{(E)}$ *be the mutual information rate and energy-normalized information rate of the release site 'without' depression. Then*

$$R_0 = h(\overline{\alpha} q_0 + \alpha p_0) - \overline{\alpha} h(q_0) - \alpha h(p_0), \tag{6}$$

$$R_0^{(E)} = \frac{R_0}{\overline{\alpha} q_0 + \alpha p_0}. \tag{7}$$

In contrast to the MRO model, for which the current state is determined by the last L releases, another approach would be to let the channel's state depend only on the release outcome and the release probabilities at time $i-1$, i.e.,

$$p_i = p_i(Y_{i-1}, p_{i-1}), \tag{8}$$

$$q_i = q_i(Y_{i-1}, q_{i-1}). \tag{9}$$

To compute the mutual information rate analytically for this second model, we need to quantize the release probabilities to a finite set of possible p_i and q_i, as we describe in detail in Appendix E. The two models generate similar performance results (Appendix F).

3. Simulation Results

Short-term synaptic depression represents a memory buffer for the synapse, as the current release dynamics of the synapse depends on the history of releases. When pre-synaptic spikes accumulate, the initial state

Table 1: Definition of notations

Symbol	Definition
X	Pre-synaptic input spike process
Y	Release outcome process
L	Memory length of the release site
p	Spike-evoked release probability
q	Spontaneous release probability
c	Depression multiplier for spike-evoked release
d	Depression multiplier for spontaneous release
e	Recovery coefficient for spike-evoked release
f	Recovery coefficient for spontaneous release
α	Pre-synaptic input spike rate
Δ	Time unit of the MRO model
R_D	Mutual information rate of the release site with depression
$R_D^{(E)}$	Energy-normalized information rate of the release site with depression
R_0	Mutual information rate of the release site without depression
$R_0^{(E)}$	Energy-normalized information rate of the release site without depression

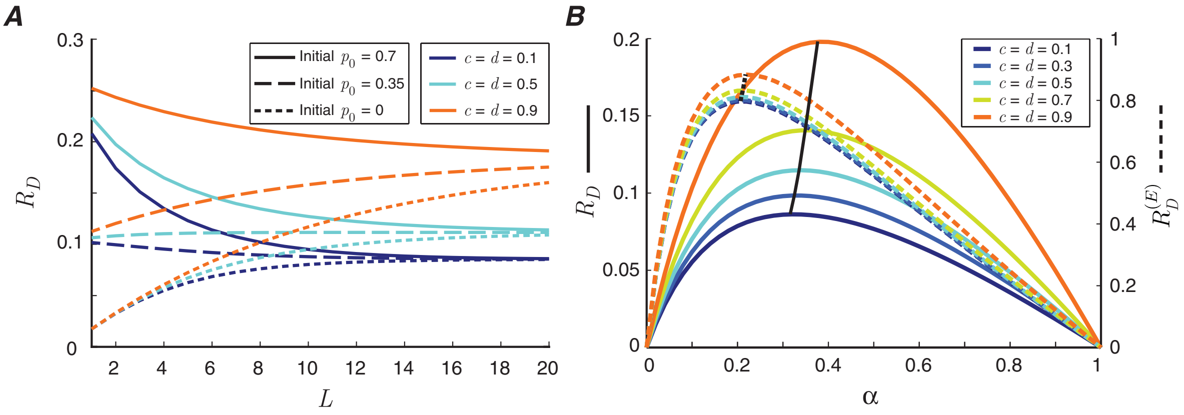

Figure 3: (A) The mutual information rate of the release site as a function of the memory length of the channel, L, for different values of depression coefficients. Three release probabilities are used as the initial state of the release site to measure the effective memory of the depressing synapse. (B) The mutual information rate (solid lines), R_D, and the energy-normalized information rate (dashed lines), $R_D^{(E)}$, as a function of input spike rate, α, for various depression coefficients, c, d. The black lines connect the maximum values of the curves. The other parameters of the model are $p_0 = 0.7, q_0 = 0.1, e = f = 0.1$. In (A), $\alpha = 0.3$, and in (B), $L = 20$.

of the synapse, as measured by its release probability, is slowly forgotten. We measure the effective memory length of short-term depression by calculating the time that the synapse requires to become independent of its initial release probability (Fig. 3A). This memory length can differ from the nominal recovery time constant of the synapse from a single release. We find that, if the release probability of the synapse is halved after each release ($c = d = 0.5$), after 160 msec (corresponding to $L = 16$), the relative variation of the mutual information caused by different initial values drops to 10%. For a synapse with stronger depression (e.g., $c = d = 0.1$), the effective memory of the synapse reduces to 120 msec.

The memory length of the MRO model, L, should match the effective memory of the synapse. We show in Appendix C that for a large enough L, the mutual information rate of the MRO model converges to the

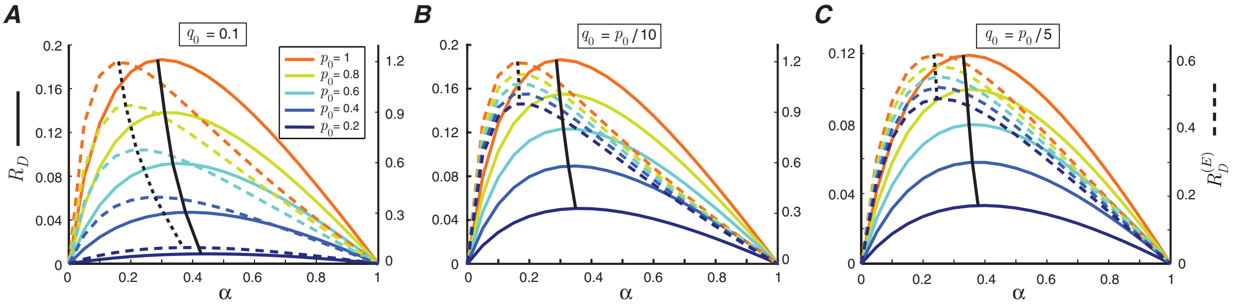

Figure 4: The ratio between evoked and spontaneous release probability controls the optimal operating point of the synapse. Mutual information rate (solid lines) and energy-normalized information rate (dashed lines) of the synapse are plotted as a function of input spike rate for different values of default (maximum) evoked release probability, p_0. (A) The default spontaneous release probability is fixed at $q_0 = 0.1$. The black lines connect the maximum values of the curves. (B) The default spontaneous release probability is a fraction of the default evoked release probability, $q_0 = p_0/10$. (C) Similar to (B) for $q_0 = p_0/5$. The other parameters of the model are $L = 20, c = d = 0.5, e = f = 0.1$.

information rate of a classical stochastic model of depression [20], the latter of which can only be evaluated numerically.

The capacity of a release site is the maximum amount of information that can be transferred through it. We show that the capacity is reduced significantly by increasing the depression level (or decreasing the speed of recovery) and is attained at lower input spike rates (solid lines in Fig. 3B). Compared to the capacity, the maximum of energy-normalized information rate is achieved at lower input spike rates, as expected. Moreover, the energy-normalized information rate is robust to variations in the parameters of depression, so that the spike rate that guarantees the optimal rate-energy performance of the release site is relatively independent of the depression level (and recovery constant) (dashed lines in Fig. 3B). This shows that even synapses with different synaptic dynamics ought to be activated at similar rates to work optimally (see also Appendix B).

The default (maximum) evoked release probability of a synapse, p_0, changes synaptic information efficacy substantially (Fig. 4A). However, if the ratio between default spike-evoked and spontaneous release probability, p_0/q_0, remains constant, then the range of variation in the energy-normalized information rate as a function of p_0 is limited; indeed, the optimal input spike rate is nearly independent of the release probability p_0 (Fig. 4B and 4C)

A release site with a memory length of $L = 20$ consists of more than one million states. In Theorem 1, we prove that the mutual information rate of the release site is equal to the statistical average of the information rates of its constituent states. Therefore, the distribution of information rates and stationary probabilities of the states specifies the share of the memory patterns in the mutual information rate. We show that there are no dominant states for the release site. Indeed, the majority of the states have a very low mutual information rate (Fig. 5A). The different states of the release site cluster, as seen in the distribution of stationary state probabilities (Fig. 5B) and in the rate-probability representation of Fig. 5D. To characterize the clusters, we identify them for the case of $L = 5$ (Fig. 5E). The clusters each turn out to represent a fixed number of releases within the release site's history.

We now study how depression dynamics of spike-evoked release affect the information efficacy of the release site, while keeping the dynamics of spontaneous release fixed. We show that for low values of spike-evoked release probability, p_0, and high values of spike-evoked depression multiplier, c, short-term depression increases the mutual information rate (Fig. 6A) and energy-normalized information rate (Fig. 6B) of the release site. Also, the enhancement effect of depression on the synaptic information efficacy is larger for the synapses with lower input spike rates. Based on our analysis, release sites can be classified into three functional categories depending on their depression dynamics (Fig. 6C):

Category 1: Depression increases both the mutual information rate and energy-normalized information rate of the release site.

Category 2: Depression increases the energy-normalized information rate, while the mutual information

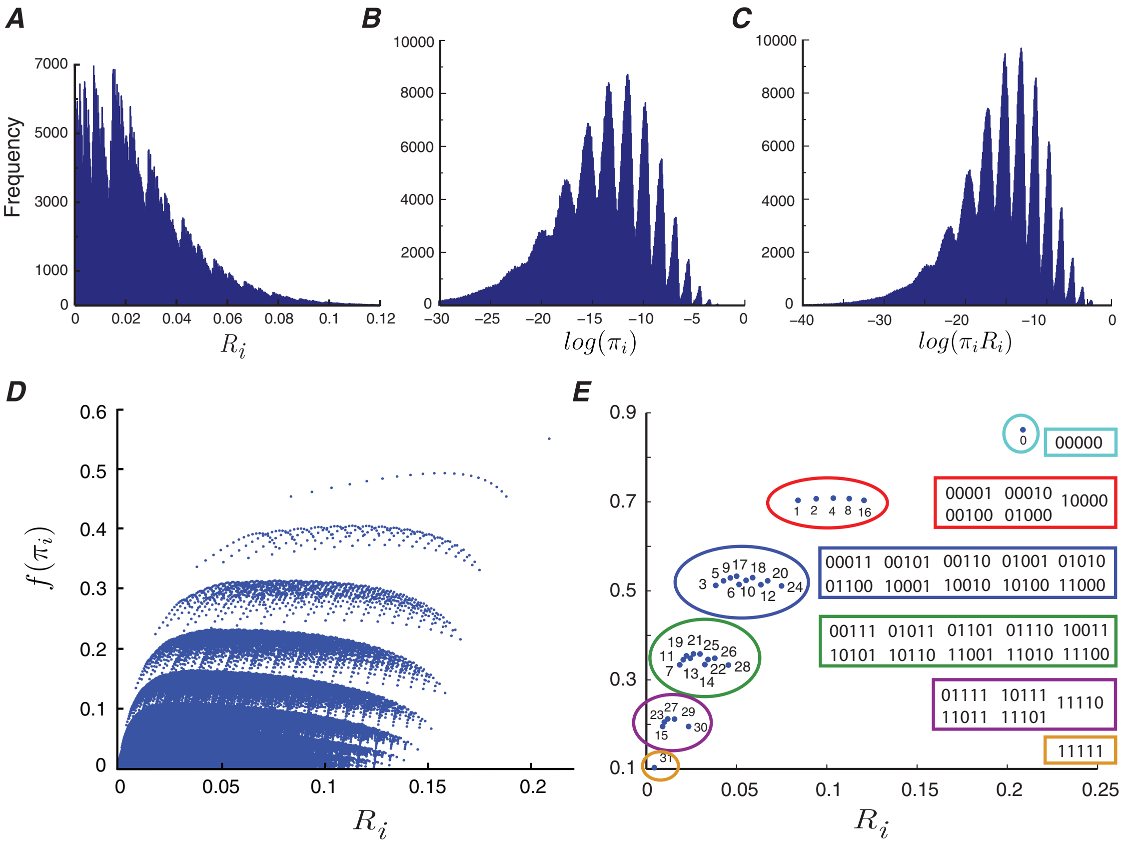

Figure 5: Distribution of the release site's states for $L = 20$. (A) Histogram of the mutual information rates of the states, R_i. (B) Histogram of the logarithm of states' stationary probabilities, $\log(\pi_i)$. The logarithm function shows the dynamic range of probabilities more clearly. (C) The histogram of $\log(R_i \pi_i)$. (D) The stationary probability of each state is plotted against its mutual information rate. The clusters get more prominent by setting $f(x) = x^{0.15}$. (E) Similar to (D), for a release site with a memory length of $L = 5$. The corresponding memory pattern is also shown for each state. The other simulation parameters are $c = d = 0.5, e = f = 0.1, p_0 = 0.7, q_0 = 0.1, \alpha = 0.2$.

rate of the release site is reduced.

Category 3: Depression impairs the performance of the release site by decreasing both the mutual information rate and the energy-normalized information rate.

The three categories imply that the enhancement of energy-normalized information rate is a necessary condition for the increase of mutual information rate during depression. We also note that the recovery coefficient of spike-evoked release has a similar impact on the synaptic information efficacy and creates the same functional categories (refer to Appendix B).

Although spontaneous release is usually ignored in information rate analysis, we show that its dynamics have a critical impact on the synaptic information efficacy during short-term depression; the release probability and depression multiplier of spontaneous release can completely change the regime of information transmission (Fig. 7A-Fig. 7C). We see that for synapses with larger spontaneous release probability, q_0, and lower depression multiplier, d, the mutual information rate and energy-normalized information rate increase during short-term depression. On the other hand, in the absence of spontaneous release ($q_0 = 0$), depression always decreases both the mutual information rate and energy-normalized information rate of the release site (Fig. 7D). Interestingly, if spontaneous release does not depress at all ($d = 1$), depression can still increase the information rate of the release site, provided that spontaneous release probability, q_0, is large enough (Fig. 7D). In addition, as long as spontaneous and spike-evoked release have similar depression dynamics ($c = d$ and $e = f$), depression will always decrease the energy-normalized information rate (Fig.

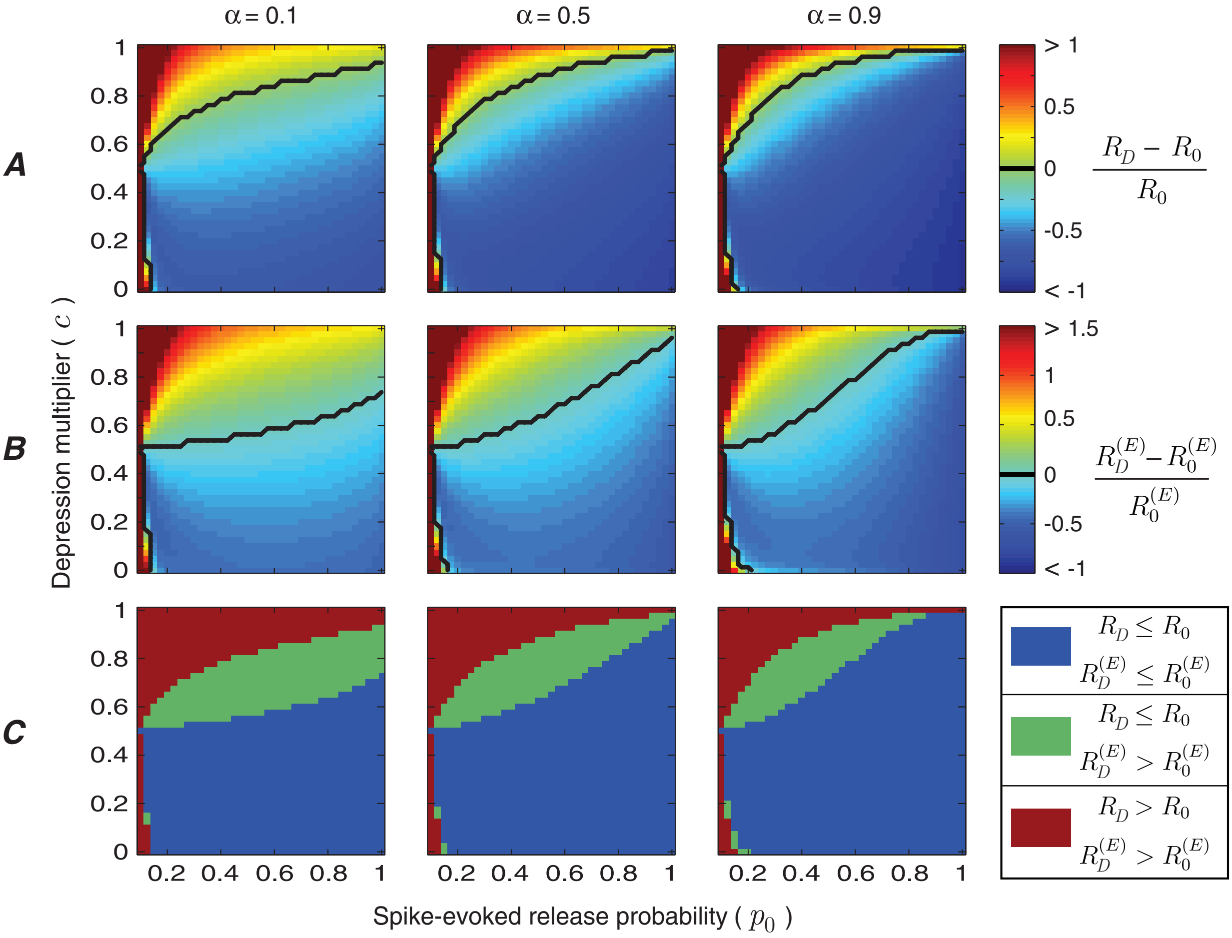

Figure 6: The impact of spike-evoked release dynamics on synaptic information transmission during short-term depression. (A) Relative difference between the mutual information rates of the release site with and without depression, as a function of depression multiplier, c, and release probability, p_0, of spike-evoked release. The black line indicates the boundary at which the functional role of synaptic depression switches from degradation to enhancement of information rate. Each column corresponds to a different input spike rate. (B) Relative difference between the energy-normalized information rates of the release site with and without depression under the same conditions as (A). (C) Classification of release sites to three functional categories based on the impact of depression on the mutual information rate and energy-normalized information rate of the release site. The parameters of spontaneous release are fixed at $d = 0.5$ and $q_0 = 0.1$, and the recovery coefficients are $e = f = 0.1$.

7E).

4. Discussion

By modeling a single synaptic release site as a binary asymmetric channel with memory, we were able to derive the information rate of synaptic release analytically. Such theoretical models rely on quantization, but the theoretical results are fully consistent with the numerical evaluation of experimentally motivated stochastic models of short-term depression [20]. In contrast to many other approaches, our calculations treat both spontaneous and spike-evoked release; both mechanisms of release are subject to short-term depression. Recent studies show that spike-evoked and spontaneous release are regulated by different biological mechanisms, such as separate vesicle pools and alternative SNARE proteins [3, 25–28]. As a consequence, the two mechanisms do not necessarily follow the same depression dynamics. We note that our statistical approach subsumes asynchronous vesicle release [29] into the spontaneous release category.

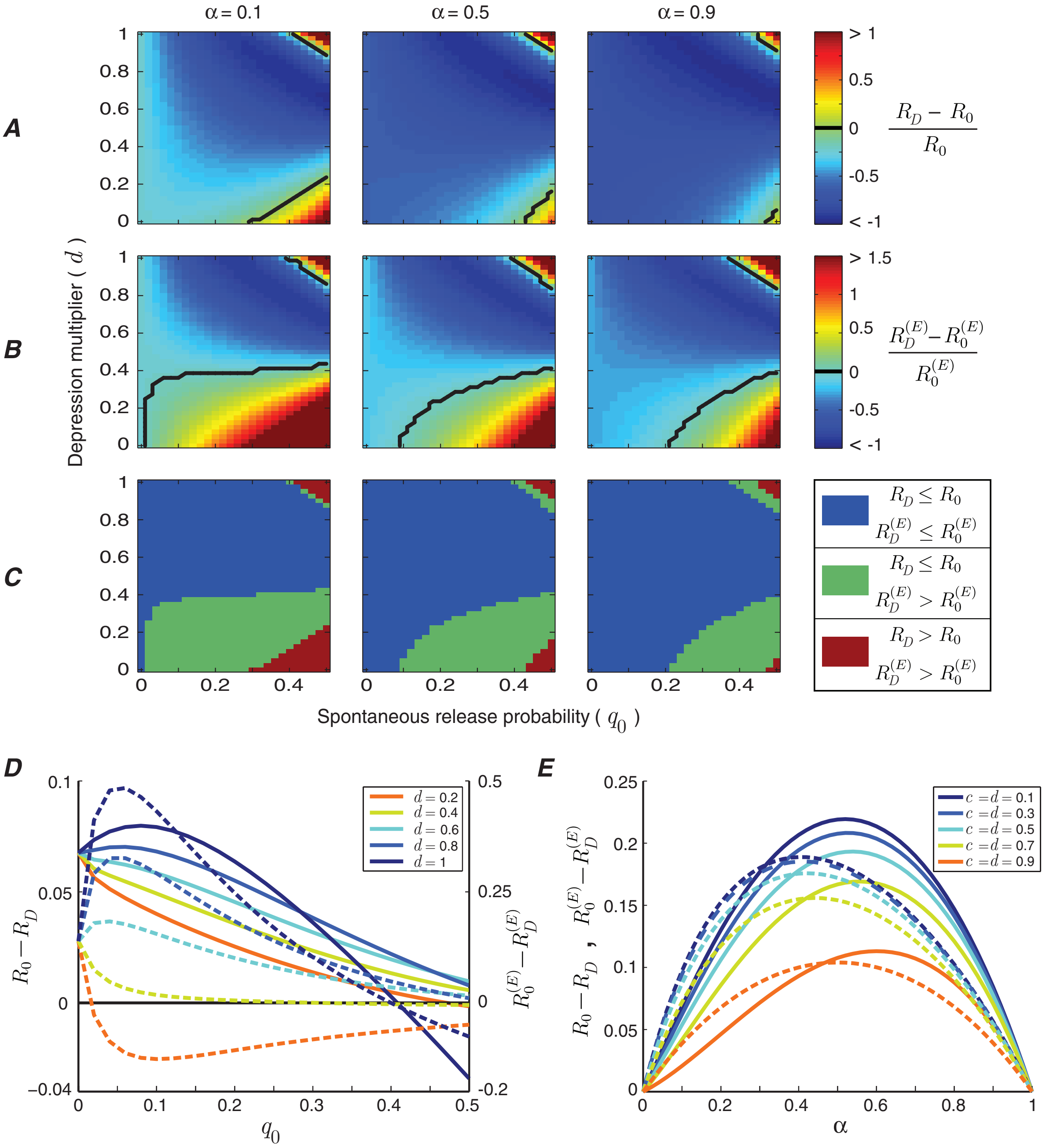

Figure 7: The modulatory effect of spontaneous release dynamics on synaptic information efficacy during short-term depression. (A) Relative difference between the mutual information rates of the release site with and without depression, as a function of depression multiplier, d, and release probability, q_0, of spontaneous release. For the spike-evoked release, the dynamics is kept fixed at $c = 0.5$ and $p_0 = 0.7$. The black line shows the boundary between positive and negative values. (B) Relative difference between the energy-normalized information rates of the release site with and without depression. (C) Three functional categories of the release site during depression. (D) Changes in the mutual information rate (solid lines), $R_0 - R_D$, and energy-normalized information rate (dashed lines), $R_0^{(E)} - R_D^{(E)}$, during depression. The functions are plotted against spontaneous release probability, q_0, for different values of depression multiplier, d. (E) The impact of similar depression dynamics for spontaneous and spike-evoked release ($c = d$) on the rate changes during depression. We simulate $R_0 - R_D$ and $R_0^{(E)} - R_D^{(E)}$ as a function of input spike rate, α, for different values of depression multiplier. For the simulations in this figure, the recovery time constants are fixed at $e = f = 0.1$.

Strikingly, we were able to show that synaptic depression can *enhance* information transmission provided that spike-evoked release is depressed less (or recovers faster) than the spontaneous release. On the other hand, if the depression dynamics for both spontaneous and evoked release are the same, then synaptic depression always decreases the information rate of the release site, as we proved. To our knowledge, there are no published data on the dynamics of synaptic depression following spontaneous release to date. What is known is that short-term plasticity differs widely in its dynamics across synapses [30]. Our results, therefore, suggest that synapses fall into one of three functional categories, based on the relative effects of depression on spike-evoked and spontaneous release (Fig. 6C).

We proved that the information rate of every release-history-dependent state contributes linearly to the overall information rate of the release site and its share is determined by the stationary probability of its occurrence. The linearity of the mutual information rate is a unique feature of short-term depression and is absent in short-term facilitation, for which the statistical average is just a lower bound for information rate (unpublished result).

Synaptic release is energetically expensive [24, 31, 32]. Indeed, it has been hypothesized that synaptic mechanisms optimize the energy-information rate balance during neuronal transmission [14, 24, 33]. To study the energy-information trade-off at the release site, we calculated the energy-normalized information rate analytically. Only the energy that is consumed by synaptic release was taken into account, which ignored the energy expenditure needed for the generation of action potentials, cellular homeostasis, or protein synthesis and transport.

In comparison to the information rate, the energy-normalized information rate of the release site was much more robust to the variations in the depression dynamics. Specifically, the optimal pre-synaptic spike rate was invariant. The spike rate needed to achieve information capacity, in contrast, was sensitive to the strength of depression, as stronger depression implied lower input spike rates. Notably, the depression dynamics vary across synapses and release sites, even in the same neuron [4]. Metaplasticity changes the depression characteristics of the release site over different time scales [34, 35]. The prediction of our work is that the input spike rate is uncoupled from synaptic metaplasticity: the input rate need not adapt to maintain the optimal energy-information balance for release sites.

We now list a few of the limitations of the model. Strictly speaking, the proposed model is valid for a single synaptic release site. The number of release sites in a synapse varies between one to hundreds, with most central nervous system synapses having one or two sites [36]. Some studies have addressed the information efficacy of the whole synapse by treating all the release sites similarly [16, 37], neglecting the individual differences of the release sites [38]. It should be possible to use parallel MRO models (with potentially distinct dynamics) to calculate the information rate of the entire synapse.

We only considered constant-rate input spike trains here. However, synaptic depression not only shapes the synaptic information channels, but directly implements temporal filtering, making neurons more sensitive to changes in presynaptic rate rather than the steady-state rate [1, 10, 11, 30, 39]. The input model can be generalized to heterogeneous Poisson processes to account for the rate changes of the input in the presence or absence of a stimulus.

To completely resolve the puzzle of information transmission between two neurons, we would still need to consider the feedback mechanisms of the synapse [40, 41], the non-linearity of receptors at the post-synaptic neuron [1, 42, 43], and other short-term and long-term dynamical mechanisms of the synapse [4, 44]. Filling in these gaps will yield a complete picture of synaptic information transmission. We believe that the MRO model can serve as an elemental building block to develop more detailed models and aid in future research to complete the full picture of synaptic information transmission.

Acknowledgement

This work was supported by the BMBF grant 01EO1401 (German Center for Vertigo and Balance Disorders).

Appendix

A. Information theoretic measures

Let X be a discrete random variable with a finite sample space $\{x_1, x_2, ..., x_n\}$. The entropy of X, denoted by $H(X)$, is the amount of uncertainty about the value of X and is calculated by

$$H(X) = -\sum_i P(X = x_i) \log_2 P(X = x_i), \tag{10}$$

where $P(.)$ is the probability measure.

For two discrete random variables X and Y, the conditional entropy of Y given X, denoted by $H(Y|X)$, describes the remaining uncertainty about the value of Y provided that the value of X is known. The conditional entropy is derived from

$$H(Y|X) = -\sum_x \sum_y P(X = x, Y = y) \log_2 P(Y = y|X = x). \tag{11}$$

The mutual information between the two random variables X and Y is defined by

$$I(X;Y) = H(Y) - H(Y|X), \tag{12}$$

and quantifies the amount of information that can be obtained from X about Y.

The notions of entropy and mutual information are extended to random processes as well. Let $X = \{X_i\}_{i=1}^{\infty}$ be a discrete time random process, where X_i is the random variable corresponding to the value of X at time i. We represent by X^n the first n instances of X,

$$X^n \triangleq \begin{cases} (X_1, X_2, ..., X_n) & \text{if} \quad n > 0 \\ 0 & \text{if} \quad n \leq 0 \end{cases} \tag{13}$$

The entropy rate of X is defined by

$$H(X) = \lim_{n \to \infty} \frac{1}{n} H(X^n), \tag{14}$$

if the limit exists.

The mutual information rate of two random processes $X = \{X_i\}_{i=1}^{\infty}$ and $Y = \{Y_i\}_{i=1}^{\infty}$ is

$$I(X;Y) = \lim_{n \to \infty} \frac{1}{n} I(X^n; Y^n), \tag{15}$$

provided that the limit exists.

Assume that the random processes X and Y are the input and output of a communication channel. Let E_i be the (random) amount of energy that is consumed by the channel at time i. The energy-normalized information rate of the channel is defined by

$$I_E(X;Y) = \lim_{n \to \infty} \frac{I(X^n; Y^n)}{\mathbf{E}(\sum_{i=1}^{n} E_i)}, \tag{16}$$

where $\mathbf{E}(.)$ is the expected value.

B. Recovery time constant and synaptic information efficacy

The speed of recovery from depression modulates the rate of information transfer at a release site. Slower recovery expands the range of the release history's impact and consequently increases the release site's memory length (Fig. 8A). The mutual information rate of a synapse with a recovery time constant of $\tau = 100$ msec (corresponding to $e = 0.1$) becomes independent of its initial state after 160 msec. For a synapse with faster recovery, $e = 0.3$ (equivalent to τ=28 msec), the impact of the initial state of the synapse is negligible after just 70 msec.

Faster recovery increases both the mutual information rate and energy-normalized information rate of the release site. (Fig. 8B). The mutual information rate changes substantially by the variations of recovery coefficient while the energy-normalized information rate is relatively robust. Specifically, by increasing the recovery coefficient, the capacity of the release site is attained at higher input spike rates. But the input spike rate that results in the optimal energy-normalized information rate, is practically independent of the recovery time constant. From Fig. 8B and Fig. 3B, we conclude that the release sites with different depression dynamics can work at their optimal energy-rate regime with the same input spike rate.

If the recovery of the spike-evoked release is faster than the recovery of spontaneous release, then depression can increase the mutual information rate (Fig. 8C) and energy-normalized information rate of the release site (Fig. 8D). We show that the differences in recovery coefficient among synapses (and release sites) create three distinct functional categories for short-term depression (Fig. 8E).

C. Model parameters

We set the parameters of the MRO model by establishing a correspondence with an updated version of the stochastic model of depression [20]. The release probability (spontaneous or spike-evoked) follows a first-order differential equation in the stochastic model,

$$\frac{dp_r}{dt} = \frac{p_0 - p_r}{\tau} - up_r\delta(t - t_r), \tag{17}$$

where p_r, τ, p_0, u, and t_r are the release probability, recovery time constant, default (maximum) release probability, depression coefficient and the release timing. In the absence of release, the release probability recovers exponentially to its default value. Assuming that the release probability at time $t = 0$ is p_{in},

$$p_r(t) = p_0 - (p_0 - p_{in})exp(-t/\tau). \tag{18}$$

Correspondingly, if we assume that in the MRO model, the release probability at time index $i = 0$ is p_{in}, then it can be easily shown that after k steps of recovery (k successive quiescent intervals),

$$p_r(k) = p_0 - (p_0 - p_{in})(1 - e)^k, \tag{19}$$

where e is the recovery coefficient of the MRO model.

The discrete time k and the continuous time t are related through the time unit, Δ, of the MRO model,

$$k = t/\Delta. \tag{20}$$

To have similar recovery dynamics in the two models,

$$(1 - e)^k = exp(-t/\tau), \tag{21}$$

and by substituting k from (20),

$$ln(1 - e) = \frac{-\Delta}{\tau}. \tag{22}$$

This equation shows the relation between the recovery coefficient of the MRO model and the recovery time constant of the synapse. For example, if the recovery time constant of a synapse is $\tau = 100$ msec, then for a time unit of $\Delta = 10$ msec, the recovery coefficient of the MRO model should be $e = 0.1$.

We use the context tree weighting algorithm [45] to calculate numerically the information rate of the synapse in a classical, stochastic model of depression [20]. In Fig. 9, we show that by increasing the memory length, L, the analytical mutual information rate of the MRO model converges to the numerical information rate estimates of the classical stochastic model of depression.

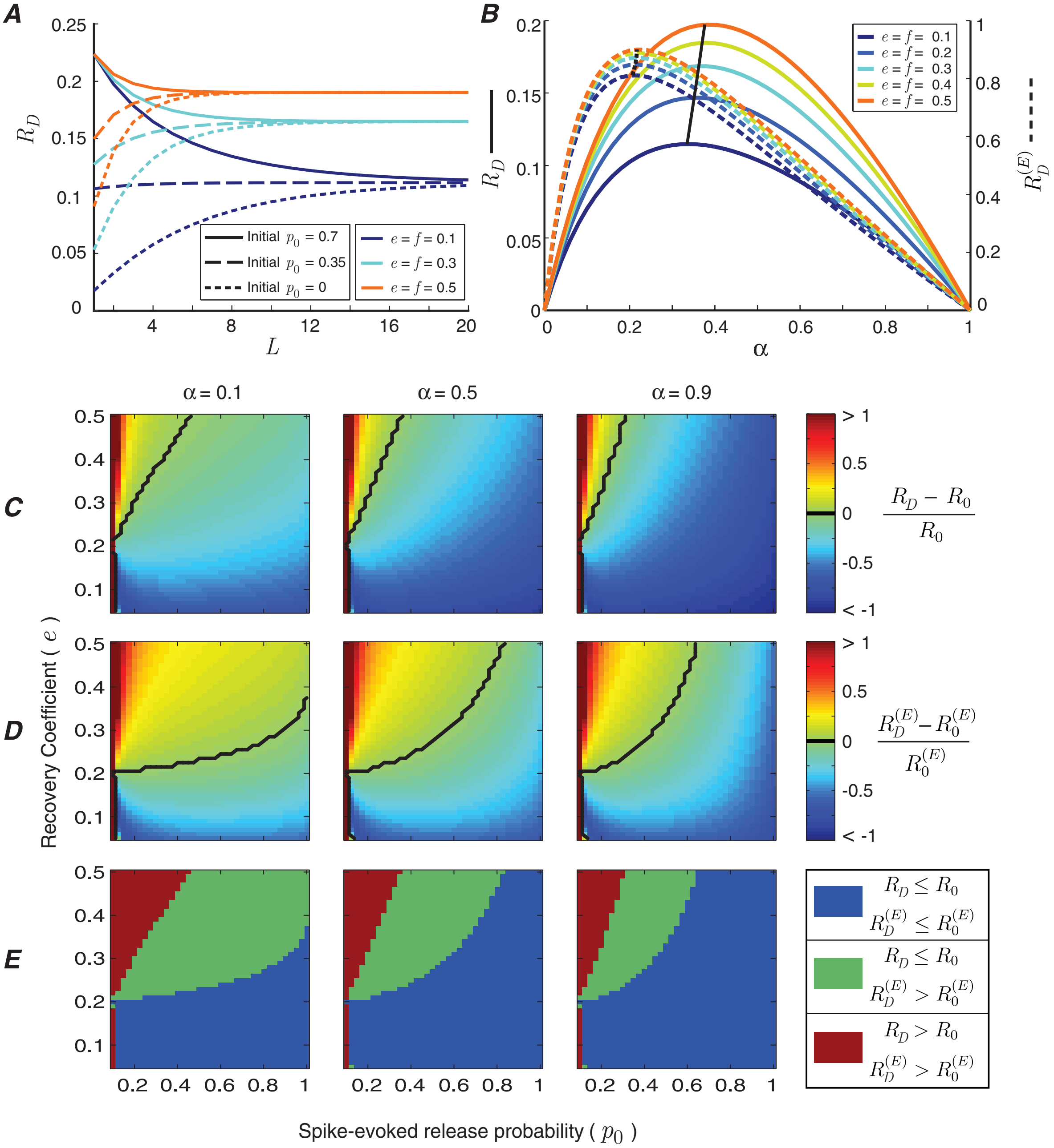

Figure 8: Modulation of information rate by the recovery coefficient of the release site. (A) Mutual information rate as a function of the release site's memory length L, for different recovery coefficients. Three release probabilities are used as the initial state of the synapse to measure the effective memory of synaptic depression. (B) Mutual information rate (solid lines) and energy-normalized information rate (dashed lines) of the release site against the input spike rate. The black lines connect the maximum of the curves. (C) Relative difference between R_D and R_0 as a function of the recovery coefficient, e, and the release probability, p_0, of spike-evoked release. The recovery coefficient of spontaneous release is fixed at $f = 0.2$. The black lines specify the zero transitions and columns correspond to different input spike rates. (D) Relative difference between $R_D^{(E)}$ and $R_0^{(E)}$, under the same conditions as (C). (E) Three functional categories for short-term depression at a release site, determined by e and p_0. In these simulations, the depression multipliers are fixed at $c = d = 0.5$ and the default spontaneous release is $q_0 = 0.1$. Also the memory length is set to $L = 20$ (except in (A)). The default spike-evoked release probability is $p_0 = 0.7$ in (A) and (B), and the input spike rate is $\alpha = 0.3$ in (A).

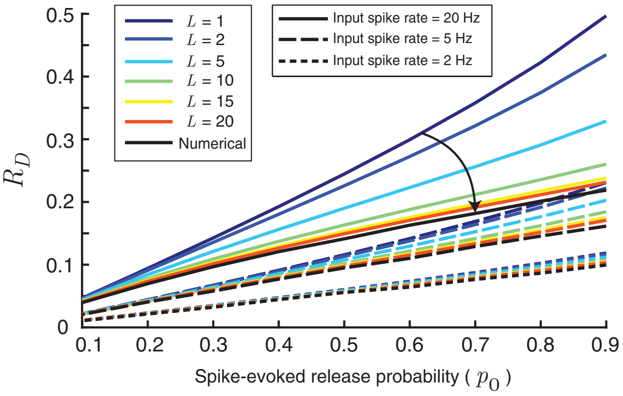

Figure 9: Comparison between the analytical mutual information rate of the MRO model with the numerical estimation of the information rate of a classical stochastic model of depression [20]. The mutual information is plotted as a function of maximum spike-evoked release probability (p_0) for various values of memory length, L, and input spike rates. The recovery time constant of the stochastic model is 100 msec and the corresponding recovery coefficient of the MRO model is $e = 0.1$. To make the comparison shown, we needed to assume that there is no spontaneous release and the depression coefficient is $c = 0$.

D. Proof of Theorems

Proof of Theorem 1: By definition

$$R_D = \lim_{n\to\infty} \frac{1}{n} I(X^n; Y^n), \tag{23}$$

where

$$I(X^n; Y^n) = H(Y^n) - H(Y^n|X^n). \tag{24}$$

Using the chain rule [46],

$$H(Y^n) = \sum_{i=1}^{n} H(Y_i|Y^{i-1}). \tag{25}$$

For integer values a, b, we define

$$Y_a^b \triangleq \begin{cases} (Y_a, Y_{a+1}, ..., Y_b) & \text{if} \quad 1 \le a \le b \\ (Y_1, Y_2, ..., Y_b) & \text{if} \quad a \le 0 < b \\ 0 & \text{if} \quad a \le b \le 0 \end{cases} \tag{26}$$

The random variable Y_i depends on the release probabilities at time i, p_i and q_i, and the input spike variable at time i, X_i. Since p_i and q_i are functions of $(Y_{i-L}, Y_{i-L+1}, ..., Y_{i-1})$, and X_i is independent of Y^{i-1},

$$H(Y_i|Y^{i-1}) = H(Y_i|Y_{i-L}^{i-1}). \tag{27}$$

Applying the chain rule to $H(Y^n|X^n)$,

$$H(Y^n|X^n) = \sum_{i=1}^{n} H(Y_i|X^n, Y^{i-1}). \tag{28}$$

With a similar argument,

$$H(Y_i|X^n, Y^{i-1}) = H(Y_i|X_i, Y_{i-L}^{i-1}). \tag{29}$$

From (24), (27) and (29),

$$I(X^n; Y^n) = \sum_{i=1}^{n} \left(H(Y_i|Y_{i-L}^{i-1}) - H(Y_i|X_i, Y_{i-L}^{i-1}) \right), \tag{30}$$

and based on the definition of conditional mutual information,

$$I(X^n;Y^n) = \sum_{i=1}^{n} I(X_i;Y_i|Y_{i-L}^{i-1}). \tag{31}$$

The sample set of Y_{i-L}^{i-1} consists of all the binary vectors of length L. For the sake of notational simplicity, instead of the binary vector $(Y_{i-L},...,Y_{i-2},Y_{i-1})$, we use its corresponding decimal value $j = Y_{i-1} + 2Y_{i-2} + 2^2Y_{i-3} + ... + 2^{L-1}Y_{i-L}$. From (31),

$$I(X^n;Y^n) = \sum_{i=1}^{n} \sum_{j=0}^{2^L-1} I(X_i;Y_i|Y_{i-L}^{i-1} = j)P(Y_{i-L}^{i-1} = j). \tag{32}$$

Let R_j represent the mutual information rate of the release site at state j. By definition,

$$R_j = I(X_i;Y_i|Y_{i-L}^{i-1} = j). \tag{33}$$

The release probabilities of the release site at state j, denoted by $p(j)$ and $q(j)$, are calculated from the algorithm in Fig. 1B. It can be easily shown that

$$R_j = h\big(\overline{\alpha}q(j) + \alpha p(j)\big) - \overline{\alpha}h\big(q(j)\big) - \alpha h\big(p(j)\big). \tag{34}$$

Each state of the release site can transit to two other states and the transition probabilities are fully determined by the current state (Fig. 1D). Therefore, a Markov chain is used to model the state transitions of the release site. The transition matrix of the Markov chain, denoted by M, is a $2^L \times 2^L$ matrix and has two non-zero entries on each row. The pattern of the non-zero entries of M is shown in Fig. 10A. It is shown in [47] that for an irreducible aperiodic finite-state Markov chain, regardless of the initial state, the probability of each state j will converge to a steady-state probability, denoted by π_j. We prove in Lemma 1 that the Markov chain of the release site in the MRO model is irreducible and aperiodic. Therefore,

$$\lim_{i\to\infty} P(Y_{i-L}^{i-1} = j) = \pi_j. \tag{35}$$

By interchanging the summations in (32),

$$I(X^n;Y^n) = \sum_{j=0}^{2^L-1} \sum_{i=1}^{n} I(X_i;Y_i|Y_{i-L}^{i-1} = j)P(Y_{i-L}^{i-1} = j). \tag{36}$$

Since $I(X_i;Y_i|Y_{i-L}^{i-1} = j) = R_j$ and is independent of i,

$$I(X^n;Y^n) = \sum_{j=0}^{2^L-1} \left(\sum_{i=1}^{n} P(Y_{i-L}^{i-1} = j) \right) R_j. \tag{37}$$

We then have

$$\begin{aligned} R_D &= \lim_{n\to\infty} \frac{1}{n} I(X^n;Y^n) && (38) \\ &= \sum_{j=0}^{2^L-1} \left(\lim_{n\to\infty} \frac{1}{n} \sum_{i=1}^{n} P(Y_{i-L}^{i-1} = j) \right) R_j. && (39) \end{aligned}$$

Using (35) and the Cesàro mean theorem,

$$\lim_{n\to\infty} \frac{1}{n} \sum_{i=1}^{n} P(Y_{i-L}^{i-1} = j) = \pi_j. \tag{40}$$

Finally, from (39) and (40),

$$R_D = \sum_{j=0}^{2^L-1} R_j \pi_j. \tag{41}$$

□

We note that the stationary probability vector $\overrightarrow{\pi} = (\pi_0, ..., \pi_{2^L-1})$ is calculated using the power method. We start by a random probability vector $\overrightarrow{x_0}$ and in each iteration $i \geq 0$, we calculate

$$\overrightarrow{x_{i+1}} = \overrightarrow{x_i} \times M. \tag{42}$$

Then we substitute $\overrightarrow{x_i}$ with $\overrightarrow{x_{i+1}}$ and repeat (42). It is easily shown that the probability vector $\overrightarrow{x_i}$ converges to $\overrightarrow{\pi}$.

Lemma 1. *In the MRO model, the markov chain of the release site is irreducible and aperiodic.*

Proof. Let j and j' be two arbitrary states of the release site corresponding to the binary vectors $(a_1, a_2, ..., a_L)$ and $(b_1, b_2, ..., b_L)$. We show that the state j' is always accessible from the state j in the Markov chain M.

Assume that the Markov chain is in the state j at time $i = 1$. The release site can transit to the state $(a_2, a_3, ..., a_L, b_1)$ with a non-zero probability $P_1(b_1)$. Similarly, at each time $i, 1 \leq i \leq L$, the release site can transit from the state $(a_i, ..., a_L, b_1, ..., b_{i-1})$ to $(a_{i+1}, ..., a_L, b_1, ..., b_i)$ with the non-zero probability $P_i(b_i)$. Therefore, the probability of transition from $(a_1, a_2, ..., a_L)$ to $(b_1, b_2, ..., b_L)$ after L time steps is greater than or equal to $\prod_{i=1}^{L} P_i(b_i)$. This proves that the state j' is accessible from the state j, and consequently, M is irreducible. Moreover, there is a non-zero transition probability from the state $j = 0$ to itself. Since every irreducible finite-state Markov chain with a self-loop is aperiodic [47], we conclude that M is aperiodic and the proof is complete.

□

Proof of Theorem 2: The energy-normalized information rate of the release site is defined by (refer to Appendix A):

$$R_D^{(E)} = \lim_{n\to\infty} \frac{I(X^n; Y^n)}{\mathbf{E}(\sum_{i=1}^{n} E_i)}. \tag{43}$$

where E_i is the energy consumed by the release site to release a vesicle at time i. By assumption, one unit of energy is consumed at each release. Therefore,

$$E_i = Y_i, \tag{44}$$

and

$$\mathbf{E}(\sum_{i=1}^{n} E_i) = \sum_{i=1}^{n} P(Y_i = 1). \tag{45}$$

From (43), (45) and Theorem 1,

$$R_D^{(E)} = \frac{\lim_{n\to\infty} \frac{1}{n} I(X^n; Y^n)}{\lim_{n\to\infty} \frac{1}{n} \sum_{i=1}^{n} P(Y_i = 1)}, \tag{46}$$

$$= \frac{\sum_{j=0}^{2^L-1} R_j \pi_j}{\lim_{n\to\infty} \frac{1}{n} \sum_{i=1}^{n} P(Y_i = 1)}. \tag{47}$$

Also,

$$P(Y_i = 1) = \sum_{j=0}^{2^{(L-1)}-1} P(Y_i = 1, Y_{i-L+1}^{i-1} = j), \tag{48}$$

$$= \sum_{j=0}^{2^{(L-1)}-1} P(Y_{i-L+1}^{i} = 2j+1). \tag{49}$$

Therefore,

$$\lim_{n\to\infty} P(Y_i = 1) = \sum_{j=0}^{2^{(L-1)}-1} \pi_{2j+1}. \tag{50}$$

From (47), (50) and Cesàro mean theorem,

$$R_D^{(E)} = \frac{\sum_{j=0}^{2^L-1} R_j \pi_j}{\sum_{j=0}^{2^{(L-1)}-1} \pi_{2j+1}}. \tag{51}$$

□

E. Quantized release probabilities

In the MRO model, the release probabilities of the release site at time i are determined by the last L release outcomes, Y_{i-L}^{i-1}. Alternatively, the release probabilities at time i can be derived recursively from the release probabilities and the release outcome at time $i-1$. In this recursive approach, the state of the release site at time i is specified by the pair (P_i, Q_i), where P_i and Q_i are the random variables corresponding to the spike-evoked and spontaneous release probabilities. Since P_i and Q_i are continuous variables, the number of states goes to infinity by increasing i. To avoid the limitations of infinite-state models, we quantize the release probabilities. For a quantization level of δ, the sample space of release probabilities is defined by

$$S = \{0, \delta, 2\delta, ..., [\frac{1}{\delta}]\delta\}, \tag{52}$$

where [.] is the floor function.

Let $[x]_S$ represent the largest entry in S that is less than or equal to x, i.e.,

$$[x]_S = \max\{y : y \in S, y \leq x\}. \tag{53}$$

Also assume that $p_0, q_0 \in S$ are the default (maximum) spike-evoked and spontaneous release probability of the release site. The quantized release probabilities at time $i+1$ are calculated recursively from

$$p_{i+1} = \begin{cases} [e(p_0 - p_i) + p_i]_S, & \text{if } Y_i = 0 \\ [cp_i]_S, & \text{if } Y_i = 1 \end{cases} \tag{54}$$

and

$$q_{i+1} = \begin{cases} [f(q_0 - q_i) + q_i]_S, & \text{if } Y_i = 0 \\ [dq_i]_S, & \text{if } Y_i = 1 \end{cases} \tag{55}$$

We refer to this model as the binary asymmetric channel with Quantized Release Probabilities, abbreviated by QRP.

We note that since spike-evoked and spontaneous release probabilities do not exceed p_0 and q_0, the sample space of (P, Q) can be reduced from $S \times S$ to $S_P \times S_Q$, where

$$S_P = \{0, \delta, 2\delta, ..., p_0\}, \tag{56}$$

and

$$S_Q = \{0, \delta, 2\delta, ..., q_0\}. \tag{57}$$

In the QRP model, the state of the release site at time i, (p_i, q_i), can transit to two other states, the recovered state $([e(p_0 - p_i) + p_i]_S, [f(q_0 - q_i) + q_i]_S)$ and the depressed state $([cp_i]_S, [dq_i]_S)$, with the transition probabilities $\alpha\overline{p_i} + \overline{\alpha}\,\overline{q_i}$ and $\alpha p_i + \overline{\alpha} q_i$ respectively. The state transitions of the QRP model are represented by a Markov chain with the transition matrix $\widehat{M}$. Unlike the MRO model, the pattern of the non-zero entries of $\widehat{M}$ is not fixed and varies with the model parameters (Fig. 10B). For each state (p, q), the stationary probability, $\pi_{(p,q)}$, is calculated using the power method. Also, the mutual information rate of the binary asymmetric channel, $R_{(p,q)}$, is derived from

$$R_{(p,q)} = h(\overline{\alpha} q + \alpha p) - \overline{\alpha} h(q) - \alpha h(p). \tag{58}$$

Theorem 3. *Let R_D and $R_D^{(E)}$ be the mutual information rate and energy-normalized information rate of the release site in the QRP model. Then*

$$R_D = \sum_{(p,q)\in P_S \times Q_S} R_{(p,q)} \pi_{(p,q)}, \tag{59}$$

$$R_D^{(E)} = \frac{\sum_{(p,q)\in P_S \times Q_S} R_{(p,q)} \pi_{(p,q)}}{\sum_{(p,q)\in P_S \times Q_S} (\alpha p + \overline{\alpha} q) \pi_{(p,q)}}. \tag{60}$$

Proof. Let $X = \{X_i\}_{i=1}^{\infty}$ and $Y = \{Y_i\}_{i=1}^{\infty}$ be the input and output random processes of the QRP model (the top panel in Fig. 10B). By definition,

$$R_D = \lim_{n\to\infty} \frac{1}{n} I(X^n; Y^n), \tag{61}$$

where

$$I(X^n; Y^n) = H(Y^n) - H(Y^n | X^n). \tag{62}$$

Using the chain rule for $H(Y^n)$ and $H(Y^n|X^n)$,

$$H(Y^n) = \sum_{i=1}^{n} H(Y_i | Y^{i-1}), \tag{63}$$

$$H(Y^n | X^n) = \sum_{i=1}^{n} H(Y_i | Y^{i-1}, X^n). \tag{64}$$

The vector of release probabilities, (P_i, Q_i), can be calculated from Y^{i-1}. Also, given X_i and (P_i, Q_i), Y_i is independent of Y^{i-1}, X^{i-1} and X_{i+1}^{n}. Therefore,

$$H(Y_i | Y^{i-1}, X^n) = H\big(Y_i | (P_i, Q_i), X_i\big). \tag{65}$$

Similarly, given (P_i, Q_i), Y_i is independent of Y^{i-1}, implying that

$$H(Y_i | Y^{i-1}) = H\big(Y_i | (P_i, Q_i)\big). \tag{66}$$

Hence,

$$\begin{aligned} I(X^n; Y^n) &= \sum_{i=1}^{n} H\big(Y_i | (P_i, Q_i)\big) - H\big(Y_i | (P_i, Q_i), X_i\big) \qquad (67) \\ &= \sum_{i=1}^{n} I\big(X_i; Y_i | (P_i, Q_i)\big). \qquad (68) \end{aligned}$$

From the definition of conditional mutual information,

$$I\big(X_i; Y_i | (P_i, Q_i)\big) = \sum_{(p,q) \in P_S \times Q_S} I\big(X_i; Y_i | (P_i, Q_i) = (p,q)\big) P\big((P_i, Q_i) = (p,q)\big). \tag{69}$$

The term $I\big(X_i; Y_i | (P_i, Q_i) = (p,q)\big)$ is the mutual information rate of the binary asymmetric channel with release probabilities p and q, which is denoted by $R_{(p,q)}$. Therefore,

$$\begin{aligned} R_{(p,q)} &= I\big(X_i; Y_i | (P_i, Q_i) = (p,q)\big) && (70) \\ &= h(\overline{\alpha} q + \alpha p) - \overline{\alpha} h(q) - \alpha h(p). && (71) \end{aligned}$$

Together with (61), (68) and (69),

$$R_D = \lim_{n \to \infty} \frac{1}{n} \sum_{i=1}^{n} \sum_{(p,q) \in P_S \times Q_S} R_{(p,q)} P\big((P_i, Q_i) = (p,q)\big). \tag{72}$$

By interchanging the summations and moving the limit inside,

$$R_D = \sum_{(p,q) \in P_S \times Q_S} R_{(p,q)} \Big(\lim_{n \to \infty} \frac{1}{n} \sum_{i=1}^{n} P\big((P_i, Q_i) = (p,q)\big) \Big). \tag{73}$$

The state of the release site at time i is given by (P_i, Q_i) and the state transitions of the release site are modeled by a Markov chain with a transition matrix $\widehat{M}$ of order $|P_S| \times |Q_S|$. We prove in Lemma 2 that the Markov chain $\widehat{M}$ is uni-chain and its recurrent class is aperiodic. Therefore, it has a unique stationary distribution and the probability of each state (p,q) converges to its stationary probability $\pi_{(p,q)}$ [47]. That is

$$\lim_{i \to \infty} P\big((P_i, Q_i) = (p,q)\big) = \pi_{(p,q)}. \tag{74}$$

Applying the Cesàro mean theorem to (73),

$$R_D = \sum_{(p,q) \in P_S \times Q_S} R_{(p,q)} \pi_{(p,q)}. \tag{75}$$

Finally, similar to the proof of Theorem 2,

$$R_D^{(E)} = \frac{\sum_{(p,q) \in P_S \times Q_S} R_{(p,q)} \pi_{(p,q)}}{\lim_{n \to \infty} \frac{1}{n} \sum_{i=1}^{n} P(Y_i = 1)}. \tag{76}$$

In the QRP model,

$$P(Y_i = 1) = \sum_{(p,q) \in P_S \times Q_S} P\big(Y_i = 1 | (P_i, Q_i) = (p,q)\big) P\big((P_i, Q_i) = (p,q)\big). \tag{77}$$

Hence,

$$\lim_{i \to \infty} P(Y_i = 1) = \sum_{(p,q) \in P_S \times Q_S} (\alpha p + \overline{\alpha} q) \pi_{(p,q)}. \tag{78}$$

From (76), (78) and the Cesàro mean theorem,

$$R_D^{(E)} = \frac{\sum_{(p,q) \in P_S \times Q_S} R_{(p,q)} \pi_{(p,q)}}{\sum_{(p,q) \in P_S \times Q_S} (\alpha p + \overline{\alpha} q) \pi_{(p,q)}}. \tag{79}$$

□

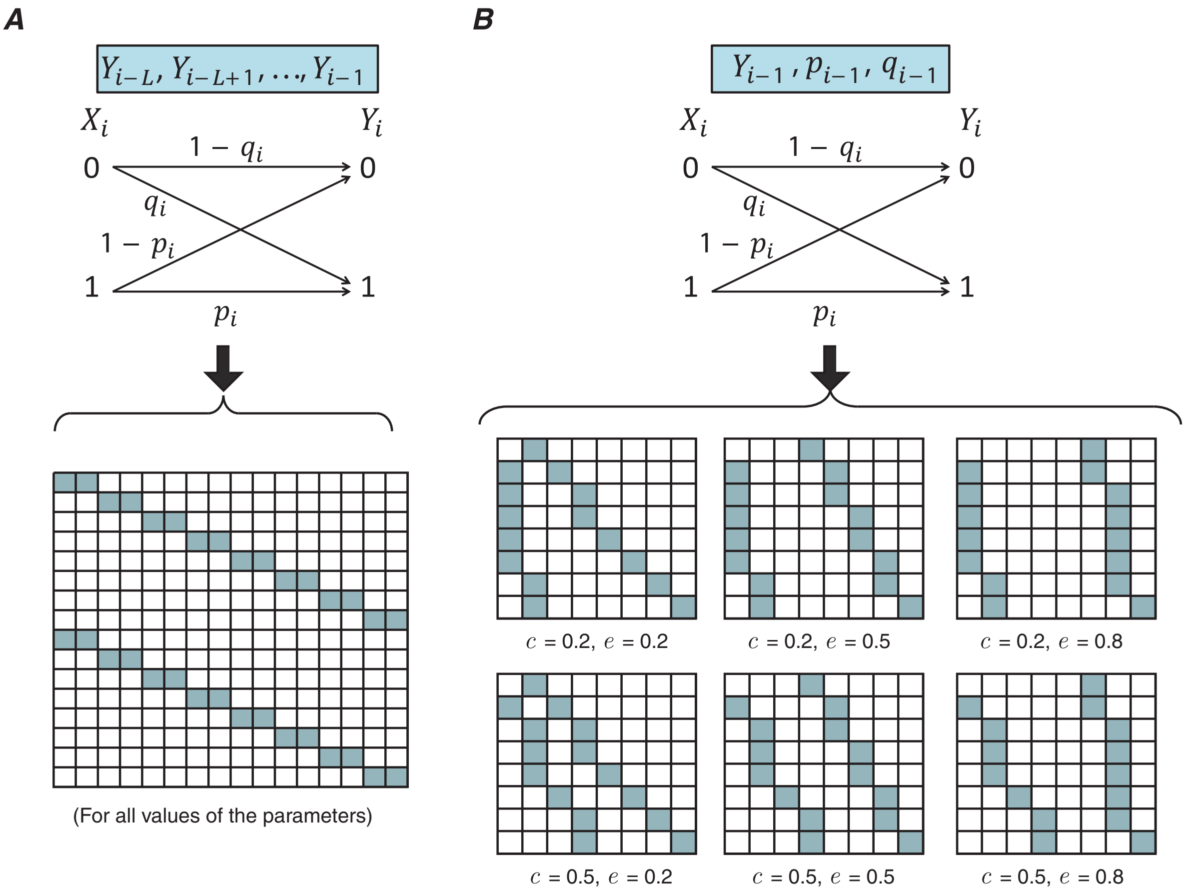

Figure 10: The non-zero entries of the transition matrix in the two models. (A) The MRO model with a memory of length $L = 4$. The transition matrix is invariant and does not change by altering the model parameters. (B) The QRP model. The pattern of the transition matrix varies based on the model parameters. The first row shows the pattern for fixed depression multiplier ($c = 0.2$) and different recovery coefficients. The second row shows the variation of the pattern for $c = 0.5$. The other parameters are $\alpha = 0.6, p_0 = 0.7, q_0 = 0.1, d = c, f = e$.

Lemma 2. *The Markov chain of the QRP model, $\widehat{M}$, is uni-chain and its recurrent class is aperiodic.*

Proof. To show that the transition matrix of the QRP model is uni-chain, we need to prove that there exists only one recurrent class in $\widehat{M}$ and the other states (if any) are transient.

Let $(a_0, b_0) \neq (0, 0)$ be an arbitrary state in $\widehat{M}$. Consider the path $(a_0, b_0) \to (a_1, b_1) \to (a_2, b_2) \to \ldots$ in which every state (a_i, b_i) transits to its depressed state, i.e., $(a_{i+1}, b_{i+1}) = ([ca_i]_S, [db_i]_S)$. As long as $(a_i, b_i) \neq (0, 0)$, the transition probability to the depressed state, (a_{i+1}, b_{i+1}), is positive. Moreover, if $a_i > 0$ then $a_{i+1} < a_i$, and if $b_i > 0$ then $b_{i+1} < b_i$. Since the number of states in the Markov chain is finite and the sequences $(a_i)_i$ and $(b_i)_i$ are monotonically decreasing to zero, there will be a large enough integer N such that $(a_N, b_N) = (0, 0)$. Therefore, there is a path from (a_0, b_0) to the state $(0, 0)$ in $\widehat{M}$. This implies that the state $(0, 0)$ is accessible from every state in the Markov chain.

Now assume that there are two recurrent classes C_1 and C_2 in the Markov chain. Since the states in C_1 have access to $(0, 0)$, from the definition of recurrent states, $(0, 0) \in C_1$. With a similar argument, $(0, 0) \in C_2$. Therefore, $C_1 = C_2$ and there is only one recurrent class in $\widehat{M}$, meaning that $\widehat{M}$ is a uni-chain.

Now we show that the period of the recurrent class is equal to one. Since the transition probability to the recovered state is always positive in the Markov chain $\widehat{M}$, we can consider the path $(a_0, b_0) = (0, 0) \to (a_1, b_1) \to (a_2, b_2) \to \ldots$ in which every state (a_i, b_i) transits to its recovered state, i.e., $(a_{i+1}, b_{i+1}) =$

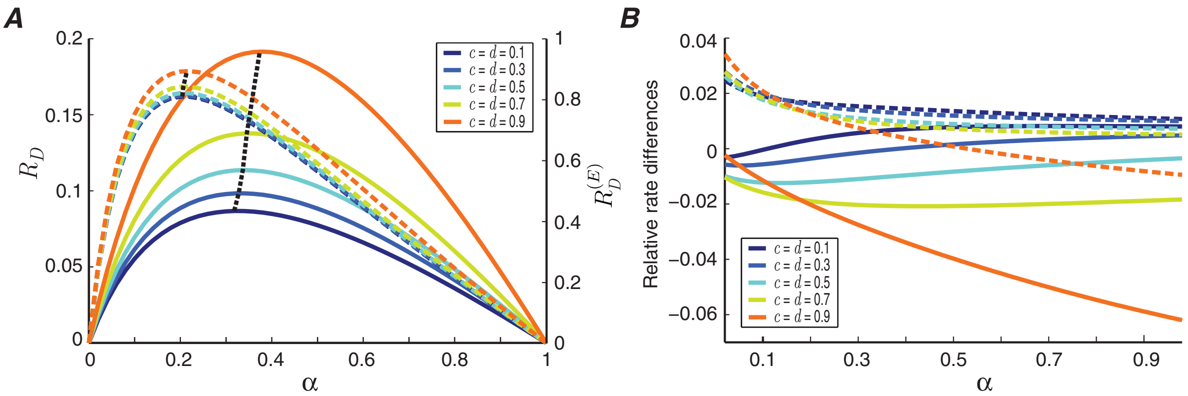

Figure 11: (A) For the QRP model, the mutual information rate (solid lines) and the energy-normalized information rate (dashed lines) are plotted as a function of input spike rate, for various depression multipliers. The other parameters of the model are $e = f = 0.1$, $p_0 = 0.7$ and $q_0 = 0.1$. (B) The relative difference between the information rates of the MRO model and the QRP model, as a function of input spike rate, for various values of depression multiplier. The solid lines show the relative difference of mutual information rates, $\frac{R_D(QRP)-R_D(MRO)}{R_D(MRO)}$, and the dashed lines show the relative difference of energy-normalized information rates, $\frac{R_D^{(E)}(QRP)-R_D^{(E)}(MRO)}{R_D^{(E)}(MRO)}$. The parameters of the two models are similar to (A).

$([e(p_0 - a_i) + a_i]_S, [f(q_0 - b_i) + b_i]_S)$. It is clear that for each i, $a_{i+1} \geq a_i$ and $b_{i+1} \geq b_i$. Since the number of states is finite, there exists a finite integer N such that

$$a_N = [e(p_0 - a_N) + a_N]_S, \tag{80}$$

$$b_N = [f(q_0 - b_N) + b_N]_S. \tag{81}$$

Therefore, the state (a_N, b_N) transits to itself with probability $\alpha \overline{a_N} + \overline{\alpha}\, \overline{b_N}$. On the other hand, (a_N, b_N) is accessible from $(0, 0)$, meaning that it belongs to the recurrent class. Since a recurrent state with a loop is aperiodic [47], we conclude that (a_N, b_N), and consequently the recurrent class of $\widehat{M}$, is aperiodic and the proof is complete. □

F. Comparison between the two models of short-term depression

There are two models that can be used to calculate the mutual information rate of the release site during short-term depression: the MRO model and QRP model. The mutual information rates and energy-normalized information rates for the release site are comparable (compare Fig. 11A to Fig. 3B). Indeed, the relative difference between the calculated rates of the two models is negligible (Fig. 11B). The two models, however, have different advantages and disadvantages. The state of the release site in the MRO model is a binary vector of length L, which corresponds to the last L release outcomes. The Markov chain of the release site consists of 2^L states and its transition matrix, M, grows exponentially with memory length. The pattern of non-zero entries in M is always fixed and does not depend on depression dynamics (Fig. 10A). In contrast, the state space of the QRP model consists of the quantized release probabilities, which is modeled by a Markov chain, $\widehat{M}$, of order $|S_P| \times |S_Q|$. Therefore, the size of the Markov chain in the QRP model can be much smaller than that of the MRO model. This will decrease the computational resources that are required for calculations of information rate in the QRP model. However, the pattern of non-zero entries of $\widehat{M}$ varies with depression coefficients (Fig. 10B), thus making it more difficult to achieve further analytical advances.

References

[1] L. Abbott, W. G. Regehr, Synaptic computation, Nature 431 (7010) (2004) 796–803.

[2] E. R. Kandel, J. H. Schwartz, T. M. Jessell, et al., Principles of neural science, Vol. 4, McGraw-hill New York, 2000.

[3] E. T. Kavalali, The mechanisms and functions of spontaneous neurotransmitter release, Nature Reviews Neuroscience 16 (1) (2015) 5–16.

[4] R. S. Zucker, W. G. Regehr, Short-term synaptic plasticity, Annual Review of Physiology 64 (1) (2002) 355–405.

[5] A. C. Kreitzer, W. G. Regehr, Modulation of transmission during trains at a cerebellar synapse, Journal of Neuroscience 20 (4) (2000) 1348–1357.

[6] S. A. Fisher, T. M. Fischer, T. J. Carew, Multiple overlapping processes underlying short-term synaptic enhancement, Trends in Neurosciences 20 (4) (1997) 170–177.

[7] J. S. Dittman, A. C. Kreitzer, W. G. Regehr, Interplay between facilitation, depression, and residual calcium at three presynaptic terminals, Journal of Neuroscience 20 (4) (2000) 1374–1385.

[8] R. Schneggenburger, T. Sakaba, E. Neher, Vesicle pools and short-term synaptic depression: lessons from a large synapse, Trends in Neurosciences 25 (4) (2002) 206–212.

[9] J. S. Dittman, W. G. Regehr, Calcium dependence and recovery kinetics of presynaptic depression at the climbing fiber to purkinje cell synapse, Journal of Neuroscience 18 (16) (1998) 6147–6162.

[10] E. S. Fortune, G. J. Rose, Short-term synaptic plasticity as a temporal filter, Trends in neurosciences 24 (7) (2001) 381–385.

[11] E. S. Fortune, G. J. Rose, Short-term synaptic plasticity contributes to the temporal filtering of electrosensory information, The Journal of Neuroscience 20 (18) (2000) 7122–7130.

[12] M. S. Goldman, P. Maldonado, L. Abbott, Redundancy reduction and sustained firing with stochastic depressing synapses, The Journal of neuroscience 22 (2) (2002) 584–591.

[13] S. Chung, X. Li, S. B. Nelson, Short-term depression at thalamocortical synapses contributes to rapid adaptation of cortical sensory responses in vivo, Neuron 34 (3) (2002) 437–446.

[14] Z. Rotman, P.-Y. Deng, V. A. Klyachko, Short-term plasticity optimizes synaptic information transmission, The Journal of Neuroscience 31 (41) (2011) 14800–14809.

[15] A. Zador, Impact of synaptic unreliability on the information transmitted by spiking neurons, Journal of Neurophysiology 79 (3) (1998) 1219–1229.

[16] M. London, A. Schreibman, M. Häusser, M. E. Larkum, I. Segev, The information efficacy of a synapse, Nature Neuroscience 5 (4) (2002) 332–340.

[17] P. Scott, A. I. Cowan, C. Stricker, Quantifying impacts of short-term plasticity on neuronal information transfer, Physical Review E 85 (4) (2012) 041921.

[18] A. Manwani, C. Koch, Detecting and estimating signals over noisy and unreliable synapses: information-theoretic analysis, Neural Computation 13 (1) (2001) 1–33.

[19] M. S. Goldman, Enhancement of information transmission efficiency by synaptic failures, Neural Computation 16 (6) (2004) 1137–1162.

[20] G. Fuhrmann, I. Segev, H. Markram, M. Tsodyks, Coding of temporal information by activity-dependent synapses, Journal of Neurophysiology 87 (1) (2002) 140–148.

[21] J. J. Harris, R. Jolivet, E. Engl, D. Attwell, Energy-efficient information transfer by visual pathway synapses, Current Biology 25 (24) (2015) 3151–3160.

[22] M. Salmasi, M. Stemmler, S. Glasauer, A. Loebel, Information rate analysis of a synaptic release site using a two-state model of short-term depression, Neural Computation 29 (2017) 1528–1560.

[23] W. J. Stewart, Probability, Markov chains, queues, and simulation: the mathematical basis of performance modeling, Princeton University Press, 2009.

[24] J. J. Harris, R. Jolivet, D. Attwell, Synaptic energy use and supply, Neuron 75 (5) (2012) 762–777.

[25] A. M. Walter, V. Haucke, S. J. Sigrist, Neurotransmission: spontaneous and evoked release filing for divorce, Current Biology 24 (5) (2014) R192–R194.

[26] J. E. Melom, Y. Akbergenova, J. P. Gavornik, J. T. Littleton, Spontaneous and evoked release are independently regulated at individual active zones, The Journal of Neuroscience 33 (44) (2013) 17253–17263.

[27] N. B. Fredj, J. Burrone, A resting pool of vesicles is responsible for spontaneous vesicle fusion at the synapse, Nature Neuroscience 12 (6) (2009) 751–758.

[28] T. Abrahamsson, C. Y. C. Chou, S. Y. Li, A. Mancino, R. P. Costa, J. A. Brock, E. Nuro, K. A. Buchanan, D. Elgar, A. V. Blackman, A. Tudor-Jones, J. Oyrer, W. T. Farmer, K. K. Murai, P. J. Sjstrm, Differential regulation of evoked and spontaneous release by presynaptic NMDA receptors, Neuron,doi:10.1016/j.neuron.2017.09.030.
URL `http://dx.doi.org/10.1016/j.neuron.2017.09.030`

[29] P. S. Kaeser, W. G. Regehr, Molecular mechanisms for synchronous, asynchronous, and spontaneous neurotransmitter release, Annual Review of Physiology 76 (2014) 333–363.

[30] G. Silberberg, C. Wu, H. Markram, Synaptic dynamics control the timing of neuronal excitation in the activated neocortical microcircuit, The Journal of Physiology 556 (1) (2004) 19–27.

[31] D. Attwell, S. B. Laughlin, An energy budget for signaling in the grey matter of the brain, Journal of Cerebral Blood Flow & Metabolism 21 (10) (2001) 1133–1145.

[32] C. Howarth, P. Gleeson, D. Attwell, Updated energy budgets for neural computation in the neocortex and cerebellum, Journal of Cerebral Blood Flow & Metabolism 32 (7) (2012) 1222–1232.

[33] K. Friston, The free-energy principle: a unified brain theory?, Nature Reviews Neuroscience 11 (2) (2010) 127–138.

[34] F. Nadim, Y. Manor, The role of short-term synaptic dynamics in motor control, Current Opinion in Neurobiology 10 (6) (2000) 683–690.

[35] R. F. Waldeck, A. Pereda, D. S. Faber, Properties and plasticity of paired-pulse depression at a central synapse, Journal

of Neuroscience 20 (14) (2000) 5312–5320.

[36] G. L. Clarke, J. Chen, H. Nishimune, Presynaptic active zone density during development and synaptic plasticity, Frontiers in Molecular Neuroscience 5.

[37] W. B. Levy, R. A. Baxter, Energy-efficient neuronal computation via quantal synaptic failures, The Journal of Neuroscience 22 (11) (2002) 4746–4755.

[38] T. Branco, K. Staras, The probability of neurotransmitter release: variability and feedback control at single synapses, Nature Reviews Neuroscience 10 (5) (2009) 373–383.

[39] L. Abbott, J. Varela, K. Sen, S. Nelson, Synaptic depression and cortical gain control, Science 275 (5297) (1997) 221–224.

[40] R. M. Evans, G. W. Zamponi, Presynaptic ca 2+ channels–integration centers for neuronal signaling pathways, Trends in Neurosciences 29 (11) (2006) 617–624.

[41] S. Z. Langer, Presynaptic autoreceptors regulating transmitter release, Neurochemistry International 52 (1) (2008) 26–30.

[42] C. Chen, D. M. Blitz, W. G. Regehr, Contributions of receptor desensitization and saturation to plasticity at the retinogeniculate synapse, Neuron 33 (5) (2002) 779–788.

[43] M. V. Jones, G. L. Westbrook, The impact of receptor desensitization on fast synaptic transmission, Trends in Neurosciences 19 (3) (1996) 96–101.

[44] J.-L. Gaiarsa, O. Caillard, Y. Ben-Ari, Long-term plasticity at gabaergic and glycinergic synapses: mechanisms and functional significance, Trends in Neurosciences 25 (11) (2002) 564–570.

[45] J. Jiao, H. H. Permuter, L. Zhao, Y.-H. Kim, T. Weissman, Universal estimation of directed information, IEEE Transactions on Information Theory 59 (10) (2013) 6220–6242, codes are available online at `http://web.stanford.edu/ tsachy/DIcode/index.htm`.

[46] T. M. Cover, J. A. Thomas, Elements of information theory, John Wiley & Sons, 2012.

[47] R. G. Gallager, Discrete stochastic processes, Vol. 321, Springer Science & Business Media, 2012.

Chapter 4

Spike detection using fractal dimension

4.1 Summary

Synaptic information efficacy quantifies the amount of information that is transferred through a synapse. In the previous chapters, we calculated the information efficacy of a model synapse during short-term depression. It is also possible to estimate information efficacy of a real synapse using experimental data. To have an accurate estimation of synaptic information efficacy, the precise timing of action potentials and release events is required. The spike timing is usually estimated from intracellular or extracellular signals. The low signal to noise ratio (SNR) of some extracellular recordings, however, makes the spike detection challenging.

We present a new spike detection algorithm to detect spikes in noisy recordings. Our algorithm is based on the fractal properties of the extracellular signals. Fractal dimension is a measure for the roughness and smoothness of the signals and is widely used in signal processing for pattern classification. We first show that the spike segments of the extracellular signal are smoother and consequently, have a lower fractal dimension than the noise segments. We then detect the spikes by thresholding the fractal dimension of the segments of the signal. The performance of our suggested algorithm is compared with four conventional spike detectors and it is shown that the fractal detector has a higher probability of spike detection in low SNR extracellular signals.

4.2 Contributions

The contributions of the authors Mehrdad Salmasi (MS), Ulrich Büttner (UB), and Stefan Glasauer (SG) are as follows: MS, UB and SG designed the study and developed the algorithm. MS analyzed the algorithm and performed the simulations. MS, UB and SG interpreted the results and wrote the manuscript.

The manuscript was published in the journal of Neural Engineering:

- M. Salmasi, U. Büttner, S. Glasauer, "Fractal Dimension Analysis for Spike Detection in Low SNR Extracellular Signals", Journal of Neural Engineering, 13(3), 36004-36022, 2016.

The preliminary results of this study were presented as abstract and poster in the Bernstein (2014) conference:

- M. Salmasi, U. Büttner, S. Glasauer, "Application of Fractal Geometry to the Detection of Spikes in Low SNR Extracellular Signals", Bernstein Conference on Computational Neuroscience (BCCN), Göttingen, September 2014.

IOP Publishing Journal of Neural Engineering
J. Neural Eng. 13 (2016) 036004 (19pp) doi:10.1088/1741-2560/13/3/036004

Fractal dimension analysis for spike detection in low SNR extracellular signals

Mehdrad Salmasi[1,3,4], **Ulrich Büttner**[1,3] **and Stefan Glasauer**[1,2,3,4]

[1] Center for Sensorimotor Research, Ludwig-Maximilian University, Munich, Germany
[2] Bernstein Center for Computational Neuroscience, Munich, Germany
[3] German Center for Vertigo and Balance Disorders, Ludwig-Maximilian University, Munich, Germany
[4] Graduate School of Systemic Neurosciences, Ludwig-Maximilian University, Munich, Germany

E-mail: mehrdad.salmasi@lrz.uni-muenchen.de

Received 12 November 2014, revised 23 February 2016
Accepted for publication 10 March 2016
Published 11 April 2016

Abstract

Objective. Many algorithms have been suggested for detection and sorting of spikes in extracellular recording. Nevertheless, it is still challenging to detect spikes in low signal-to-noise ratios (SNR). We propose a spike detection algorithm that is based on the fractal properties of extracellular signals and can detect spikes in low SNR regimes. Semi-intact spikes are low-amplitude spikes whose shapes are almost preserved. The detection of these spikes can significantly enhance the performance of multi-electrode recording systems. *Approach.* Semi-intact spikes are simulated by adding three noise components to a spike train: thermal noise, inter-spike noise, and spike-level noise. We show that simulated signals have fractal properties which make them proper candidates for fractal analysis. Then we use fractal dimension as the main core of our spike detection algorithm and call it *fractal detector*. The performance of the fractal detector is compared with three frequently used spike detectors. *Main results.* We demonstrate that in low SNR, the fractal detector has the best performance and results in the highest detection probability. It is shown that, in contrast to the other three detectors, the performance of the fractal detector is independent of inter-spike noise power and that variations in spike shape do not alter its performance. Finally, we use the fractal detector for spike detection in experimental data and similar to simulations, it is shown that the fractal detector has the best performance in low SNR regimes. *Significance.* The detection of low-amplitude spikes provides more information about the neural activity in the vicinity of the recording electrodes. Our results suggest using the fractal detector as a reliable and robust method for detecting semi-intact spikes in low SNR extracellular signals.

Keywords: fractal dimension, spike detection, extracellular signal, low SNR, box-counting, semi-intact spikes

(Some figures may appear in colour only in the online journal)

1. Introduction

Extracellular recordings are a rich source of information for analyzing the activity of different brain regions at the neuronal level. The generation of a spike in a neuron alters the extracellular field potential, which can be recorded through an electrode inserted into the extracellular area. Therefore, the recorded extracellular signal reflects the activity of all the neurons that are in the neighborhood of the electrode.

In order to analyze the information content of extracellular signals, several processing steps are required. One of the main processing steps is spike detection through which spike timing is estimated. The detected spikes are used as the inputs to a spike sorting algorithm where they are classified into different clusters. Each cluster is supposed to contain the spikes of one of the neighboring neurons.

There are various methods for spike detection and spike sorting in extracellular signals [1]. The most common spike detection method is the *threshold detector* which is widely used in different implementations. In this method, a threshold is applied to the signal and the segments of the signal that cross the threshold are recognized as spikes [2, 3]. The threshold detector has a simple structure, but it does not perform well in low signal to noise ratios (SNR). This is considered as main drawback of the threshold detector. Despite the limitations of the threshold detector, it is widely used in combination with other algorithms for spike sorting. In such combined methods, first the spikes are detected using a loose threshold and then the detected spikes, which may also include some false positives, are classified into different clusters. If the sorting algorithm works well, the false positive spikes are detected in this stage. Therefore, spike sorting algorithms can also work as spike detector.

Template matching is one of the methods that is used alone or in combination with a threshold for spike detection and spike sorting [4–6]. A well-known realization of template matching is based on linear filters and is called *average matched filter detector* [7]. In addition to template matching, there are some spike sorting algorithms that employ principal component analysis (PCA) [8, 9]. PCA can also be applied to the wavelet coefficients of the signals [10, 11]. The combination of wavelet transform and PCA for extracellular signals results in a powerful spike detector which is called *wavelet-PCA detector*.

Despite these various algorithms for spike detection, it is still a demanding task to detect spikes in low SNR signals. Here, we propose a new spike detector which exploits fractal properties of the signals and is able to detect spikes in low SNR regimes.

The term *fractal* was first used by Mandelbrot to address complicated geometric shapes [12]. Although mathematicians have not reached to a unique definition for fractals yet, their characteristics are studied extensively in fractal geometry. One of the characteristics of fractals is self-similarity, like a cauliflower. Another property of a fractal is related to its dimension. Fractal dimension is an extension of the Euclidean dimension and measures the irregularity and complexity of the fractal. Therefore, the fractal dimension of a smooth curve like a sine wave is less than the fractal dimension of a complex curve like the Koch curve [13].

Fractal dimension has found numerous applications in signal processing. The applications range from target detection in radar systems [14] to tumor detection in MRI images [15, 16]. Fractal dimension has also been used in the following neuroscientific research areas: reliable detection of epileptic seizures in patients [17], analysis of sleep cycles [18], estimation of the consciousness level in patients under anesthesia [19], emotion detection from EEG signals [20], detection of changes in white matter structure [21], and detection of transient effects in EEG signals [22, 23].

In this paper, we use fractal dimension to distinguish between spike and noise segments in extracellular signals. We design a spike detection algorithm based on fractal dimension and call it *fractal detector*. Since the structure of extracellular signals differs from other previously analyzed signals such as EEG [22, 23], we need to design a fractal detector suitable for extracellular signals. For evaluating the performance of spike detectors, we require prior knowledge of spike timing. Therefore, in the following, we simulate extracellular recordings and use the simulated signal together with the known spike timing to derive performance measures of various detection algorithms.

We confine ourselves in this paper to the detection of a specific category of spikes to which we refer as *semi-intact spikes*. These spikes have small amplitude in comparison with the level of surrounding noise signal. Nevertheless, they are not highly distorted with the activity of near neighboring neurons and their shape is preserved to some extent.

Detection of semi-intact spikes provides us with more information about the neuronal activity in the neighborhood of the electrode(s). Especially in multi-electrode recordings, the detection of semi-intact spikes in one electrode can enhance detection and decomposition of the compound spikes in the other electrodes.

We first present an algorithm for modeling extracellular signals with this category of spikes. The algorithm generates a sequence of spikes using a data-set of spike shapes. A typical sequence is shown in figure 1(a). The spike train is deteriorated with three noise components to which we refer as *thermal noise*, *inter-spike noise* and *spike-level noise*. A typical noisy spike train is shown in figure 1(b). The simulated extracellular signal is utilized for analyzing the performance of the spike detection algorithms. As a typical example, figure 1(c) shows the performance of the threshold detector. Since the signal to noise ratio is low, the threshold detector can only detect two out of five spikes. In contrast to the threshold detector, our suggested fractal detector is capable of detecting all five spikes (figure 1(d)). Finally we extend our analysis to experimental data to study the performance of the fractal detector for spike detection in real datasets.

The main contributions of this paper are summarized in the following:

- It is demonstrated that both the spike segments and noise segments of the simulated signal have fractal properties and are good candidates for fractal analysis (section 3.1.1).
- We show that the fractal dimension of the spike segments is smaller than the fractal dimension of the noise segments. Thus, a running fractal dimension is used for spike detection. We name our proposed method *fractal detector* (section 3.1.2).
- We compare the performance of the fractal detector to the threshold detector, the average matched filter detector, and the wavelet-PCA detector. We show that for low SNR signals, the fractal detector has the best performance and produces the highest detection probability (section 3.2.1).
- We show that the performance of the fractal detector, in contrast to the other three spike detectors, is independent of inter-spike noise power (section 3.2.1) and is reliably invariant to variations of spike shapes (section 3.2.3).

2. Methods

In this section, we explain in detail the structure of the fractal detector. Also, we present our suggested method for simulating signals containing semi-intact spikes. The simulated

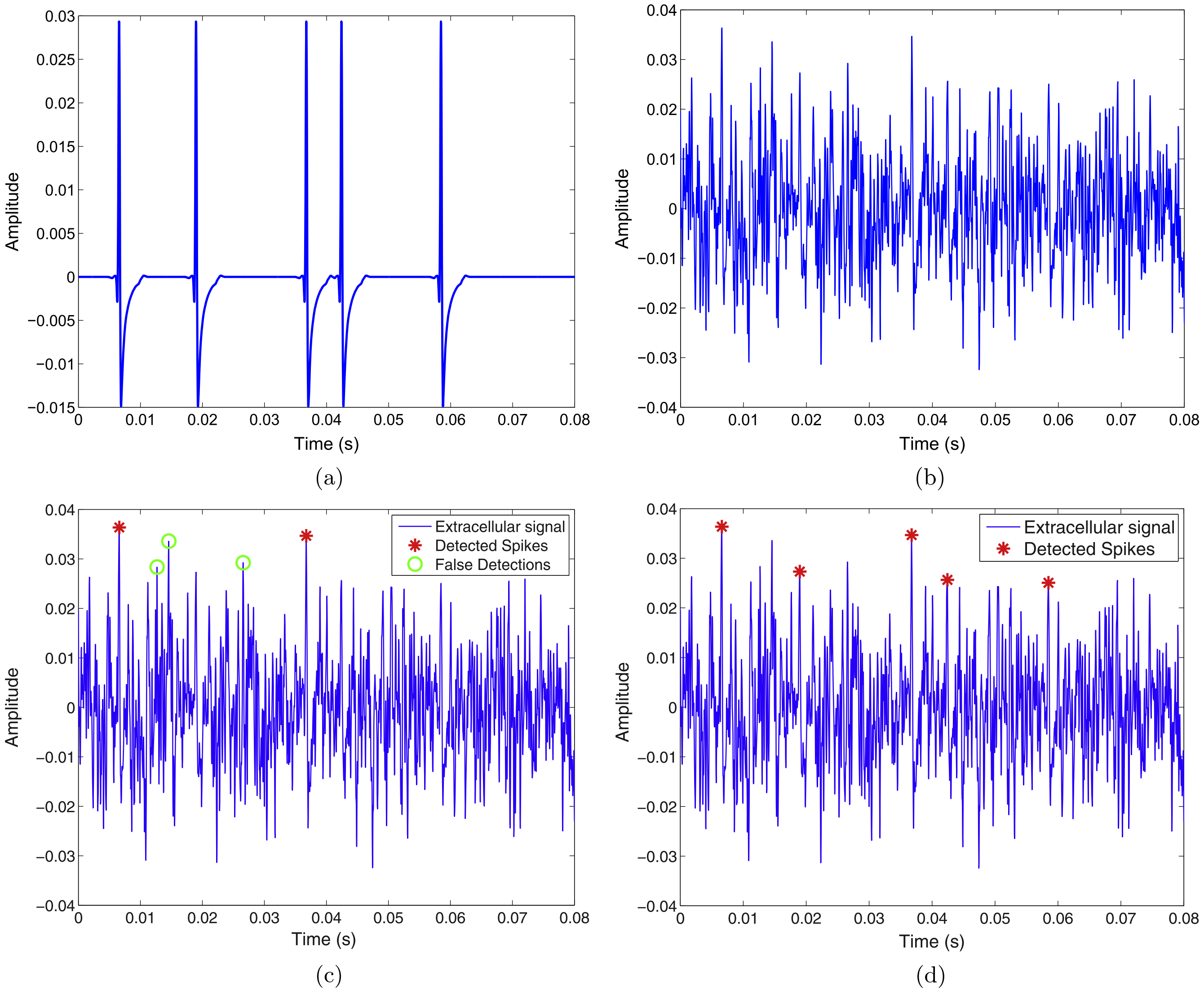

(a)

(b)

(c)

(d)

Figure 1. Simulation of extracellular signals and the performance of threshold and fractal detector ($\sigma_{\mathrm{TN}} = 0.02$ and $\sigma_{\mathrm{ISN}} = 0.04$). (a) Sequence of spikes. The spike shape is selected from the data set and is inserted at time points determined by a Poisson random process. (b) Simulated extracellular signal. The spike sequence is deteriorated with thermal noise, inter-spike noise and spike-level noise. (c) Spikes detected by the threshold detector. The red stars show correctly detected spikes and the green circles show false detections. (d) Spikes detected by the fractal detector. The red stars show the correctly detected spikes. All five spikes are detected.

signals are used to compare the performance of our fractal detector with three other detectors: threshold detector, wavelet-PCA detector and average matched filter detector. Since there are different realizations for these detectors, we briefly describe their implementation for our simulations.

2.1. Simulation of semi-intact spikes

The spike detection algorithms recognize some segments of the signal as spikes. But detection probability can be derived by comparing the timing of these detected spikes with the correct timing of spikes. Hence, for analyzing the performance of spike detectors, we require to know the spike timing in advance. This limitation enforces us to simulate extracellular signals. The simulation provides us with the extracellular signal together with the spike timing. Another advantage of simulation is that we can investigate the influence of different features of the signal, e.g. noise level and noise bandwidth, on the performance of spike detection algorithms.

Simulation of extracellular signals has been the topic of several researches. One of the simplest models is presented in [4]. In this model, the spike shapes are modeled by a continuous piece-wise linear function and white Gaussian noise is added to them in order to simulate extracellular signals. This model does not consider biophysical features of neurons. Also the geometry of neurons and the place of the electrode relative to the neurons are not included in this model. Some extensions are suggested for this model. For example, the shape of extracellular action potentials is estimated through cable theory and volume conductor theory [24]. Moreover, the effect of neighboring neurons on extracellular signals is modeled through various approaches [25, 26].

When biophysical properties are added to the model, the computational complexity of the model is highly increased. In

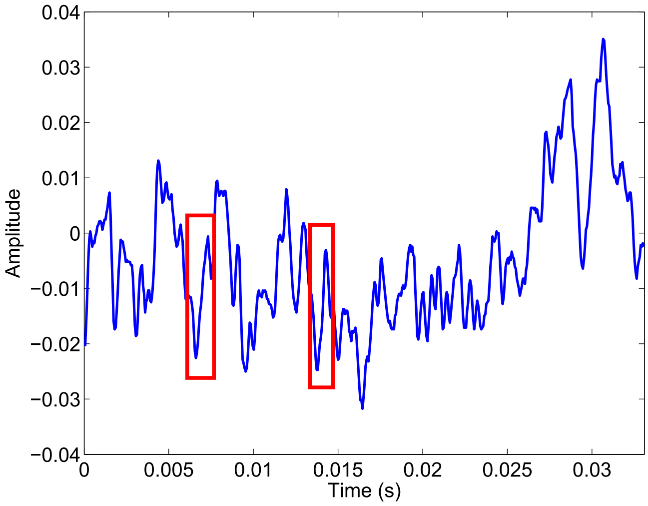

Figure 2. Recording from frontal eye field neurons of a macaque monkey. Semi-intact spikes are indicated by boxes.

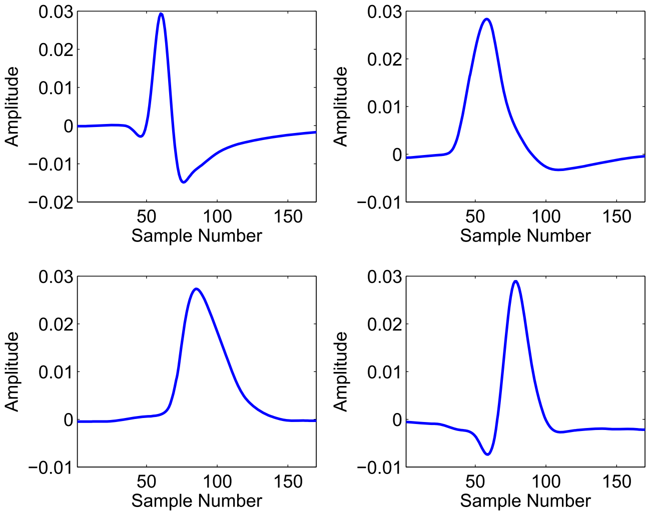

Figure 3. Some of the typical extracellular spike shapes of the data set.

order to solve this limitation, some computationally efficient algorithm are suggested which are based on model simplifications [27, 28]. There is also a Matlab toolbox, namely Neurocube, which generates extracellular signals. The toolbox simulates a given population of neurons inside a cube. Neurons are categorized into near and far neurons and the signal is simulated using a data set of extracellular spike shapes [28].

In this paper, we are interested in the detection of a particular category of spikes which are called *semi-intact spikes*. Let the target neuron be surrounded by a dense cluster of neurons. Based on the interaction between the spikes of the target neuron and the neural activity of near neighboring neurons, we can classify the spikes of target neuron into two categories. The first category consists of those spikes that are mixed with spikes of near neighboring neurons. These spikes are called compound spikes and their shapes are remarkably disfigured. The second category includes spikes that are not significantly distorted by the activity of near neurons. We call this category of spikes semi-intact spikes. Although the spikes of this category are not interfered by near neurons, they are still degraded by thermal noise and the activity of far neurons. Nevertheless, the shape of semi-intact spikes is moderately preserved and they can be found abundantly in experimental signals. Figure 2 shows a recording from frontal eye field neurons of a macaque monkey. Some semi-intact spikes are indicated with boxes. Although these spikes have low amplitudes, their shapes are almost preserved.

The detection of the semi-intact spikes increases the amount of information that can be extracted from neural recordings. Moreover, multi-electrode recording techniques can benefit from the detection of semi-intact spikes. Since there is a correlation between the recorded signals of electrodes, the detection of semi-intact spikes in one electrode will help enhancing the detection in other electrodes. Therefore, it is desirable and worthwhile to detect semi-intact spikes.

Since we confine ourselves to semi-intact spikes and exclude compound spikes, it is required to design a specific algorithm for simulating extracellular signals. Our algorithm is a simplified form of the model used in [28]. It preserves the important features of semi-intact spikes and the signal is generated very fast, which is suitable for repetitive simulations. The steps of our suggested algorithm are explained in the following.

2.1.1. Generation of spike train. We want to generate an extracellular signal of duration T and a sampling frequency of f_s. We generate the vector of spike timing through a Poisson random process with rate r. Also, we consider a refractory period so that a reasonable time interval exists between spikes. Instead of modeling the shapes of extracellular action potentials, we use a data set from the Neurocube toolbox, which contains hundreds of extracellular spike shapes. Thereby we can significantly reduce the amount of time that is needed for signal generation. Some typical spike shapes of the data set are shown in figure 3. The spike amplitude is plotted against the sample number (instead of time), because the temporal width of the spikes is a parameter that is selected based on the type of the simulated spikes. The parameters used in our simulations are $T = 1$ s, $f_s = 50$ kHz and $r = 100$. We choose a typical spike shape and insert it in the time points that are determined by the vector of spike timing. Figure 1(a) shows a part of the noise-free signal after substituting the spike shape.

2.1.2. Simulation of noise. There are different methods for simulating noise in extracellular signals. In the simplest case, it is modeled as white Gaussian noise added to the noise-free signal [4]. In more realistic simulations, noise consists of two components. The first component is thermal noise modeled by white Gaussian noise and the second component is a noise signal caused by the activity of neighboring neurons [28]. In order to simulate this second component, an imaginary electrode is considered at a position near the target neuron.

Then, extracellular action potentials of neighboring neurons are attenuated based on their distance to the electrode and their sum is used as the second component of noise.

In the present paper, we deal with semi-intact spikes and the suggested model needs to reflect the properties of these spikes. We simulate the signal by adding three noise components to the sequence of spike shapes:

Component 1: *Thermal noise*. This component is modeled as white Gaussian noise added to the whole signal [4]. It is used to model the two phenomena that underlie the distortion of semi-intact spikes:

(a) Electronic noise (Johnson noise).
(b) The activity of the neurons that are far from the target neuron.

If we denote the thermal noise by X_{TN}

$$X_{\mathrm{TN}}(n) = \sigma_{\mathrm{TN}} Z(n); \tag{1}$$

where Z is an i.i.d process with standard Gaussian distribution (zero mean and unit variance) and σ_{TN} is the level (power) of the thermal noise. We use the terms 'level' and 'power' interchangeably in this paper.

Component 2: *Inter-spike noise*. We generate this noise component by passing white Gaussian noise through a low-pass filter [29, 30]. The output of the filter is a colored-noise which is added only to inter-spike intervals. We represent this noise component by X_{ISN} and

$$X_{\mathrm{ISN}}(n) = \sigma_{\mathrm{ISN}} Z(n) * h(n); \tag{2}$$

where $h(n)$ is the impulse response of the low-pass filter and σ_{ISN} is the power of the inter-spike noise.

The inter-spike noise component is used to model the activity of neurons that are in near neighborhood of the target neuron. Since we want to evaluate the detection performance for semi-intact spikes, compound spikes are not included in our simulations and all spikes are semi-intact spikes. For this reason, we limit the second noise component to inter-spike intervals.

Component 3: *Spike-level noise*. We defined semi-intact spikes as the spikes whose shapes are not significantly distorted with the spikes of near neurons. However, the activity of near neighboring neurons still can shift the amplitude of semi-intact spikes without changing their shapes. Also the displacements of the electrode can result in a change in the amplitude of these spikes. We use this noise component to model these two aspects. The component shifts the spikes of the target neuron with a random value. For each spike, the shift value is selected randomly from a Gaussian distribution with zero mean and a variance which is represented by σ_{SLN}.

As an example, we generate a typical noise signal using these 3 components and add it to the noise-free signal of figure 1(a). The resulted signal is shown in figure 1(b). As one can see, the spikes are almost buried in noise. We represent the simulated extracellular signal by $S(n)$, $n = 1, 2, .., N$, where $N = T \times f_s$. We denote the index letter by n to indicate the discrete nature of the simulated signal.

2.2. Performance measures for spike detection algorithms

Before discussing the spike detection algorithms, we present the measures through which we can quantify the performance of these algorithms. In this paper, we use two measures.

Detection probability (True positive rate): this is the probability that the algorithm can detect spikes. We denote it by P_{d} and it is calculated by dividing the number of detected spikes by the total number of spikes.

False-alarm probability (False positive rate): for evaluating the false-alarm probability, we count the number of times that a noise segment is detected incorrectly as a spike and divide it by the total number of spikes. This quantity is also known as false positive rate and we represent it by P_{fa}. Note that generally, P_{fa} is derived by dividing the number of false detections by the total number of segments. But in our case, since the number of segments and the number of spikes are both fixed, it does not change the interpretation of the results. Here, we prefer to quantify P_{fa} as a fraction of the number of spikes and thus we divide the number of false detections by the number of spikes. For example, if $P_{\mathrm{fa}} = 0.1$ and the number of spikes is 100, then it means that 10 noise segments of the signal have been detected as spikes.

In order to assess the performance of a spike detection algorithm, we first set a value for P_{fa} and then calculate P_{d} for each instance of extracellular signal. Finally, the average of P_{d} is evaluated over all generated extracellular signals. The average of P_{d} is the main feature that is used in this paper for the performance analysis of spike detectors.

2.3. Threshold detector

Thresholding is the most common method for spike detection. A threshold is set for the extracellular signal and the segments of the signal that cross the threshold are considered as spikes [2, 3]. In low SNR, the performance of threshold detector is not convenient.

As an example, we use threshold detector for the signal in figure 1(b). The performance of the threshold detector is shown in figure 1(c). Red stars represent the correctly detected spikes and green circles show the false detections. It can be seen that threshold detector has a weak performance and only two out of five spikes can be detected. However, some extensions have been suggested for improving the performance of threshold detector in low SNR signals [31, 32]. Here, we employ the standard threshold detector, which is based on a fixed threshold.

2.4. Average matched filter detector

Template matching is one of the first methods that was used in spike sorting algorithms [4–6]. In this method, spike templates are utilized for classification of spikes in the extracellular recordings. For each template, the distances between the template and the segments of the signal are calculated and used for detecting and sorting the spikes. Template matching can be implemented by linear filters. The signal is passed through a linear filter in order to increase the spike power in comparison with the noise power. We want to find the optimal linear filter that results in the maximum signal to noise ratio at its output. If the noise of the signal is additive white Gaussian noise, it is proved in signal processing that the optimal linear filter is the one that correlates its input with the spike shape. This filter is called *matched filter* because the impulse response of the filter is the vertically flipped form of the spike shape.

Matched filters are a conventional method for detecting and extracting different features of neural signals [33, 34]. Specifically, matched filter provide an effective way for spike detection. First the noisy signal is passed through the matched filter and then the spikes are detected using a threshold on the output of the filter.

In supervised methods, the spike templates are selected by a pre-scanning of the signal. In unsupervised algorithms, some predefined templates are used. A typical template is derived by averaging over a set of possible spike shapes and the resulted template is used for spike detection. This spike detector is called *average matched filter detector* [7].

2.5. Wavelet-PCA detector

There are some algorithms that employ PCA for spike sorting. PCA is a technique for dimensionality reduction of data sets, which is widely used in the processing of neuronal activity [35, 36]. The first component of the PCA gives the direction of maximum variance in the data and can be used as the main feature for classification. We can use more components of PCA for including more variations of the data in the classification algorithm. The number of components is selected depending on the application and the data set. Sometimes the first component is sufficient for classification and sometimes more components are required.

For spike sorting, spikes are first detected with a threshold and then PCA is used to extract a feature from the spike shapes. Finally, spikes are classified into clusters using the extracted feature [8, 9, 37].

While these algorithms work in time domain, there are some other approaches that detect and sort the spikes in frequency or time-scale domains. Wavelet transform is one of the tools that can be used for processing neural signals in the time-scale domain for spike detection [30, 38] and for spike sorting [39–41]. In order to use wavelet transform for spike sorting, spikes are first detected by thresholding. Then the wavelet coefficients of detected spikes are evaluated and spikes are sorted based on the features extracted from the wavelet coefficients. It has been shown that wavelet transform can outperform PCA in spike sorting [39, 42]. Wavelet transform is also used in combination with PCA in different applications [11, 43]. Here, we use the combination of wavelet transform and PCA for spike detection.

In the first step of this method, we find the segments of the signal that cross a threshold and then the wavelet transform of each segment is evaluated using the Haar wavelet with four levels of decomposition. Our goal is to distinguish between spike segments and noise segments based on their wavelet coefficients. Hence, we need to extract a feature from wavelet coefficients that can classify the signals accurately. The required feature is extracted using PCA. This spike detection algorithm is called *wavelet-PCA detector*. In appendix A, it is shown that the extracted feature can separate spike and noise segments efficiently. Also we demonstrate that the first principle component is sufficient for the spike detection.

2.6. Fractal detector

In this part, we explain our suggested new method for spike detection, which is based on fractal dimension. There are different definitions for fractal dimension and we describe a well-known algorithm for calculating box-counting fractal dimension. However, before calculating the fractal dimension of extracellular signals, it is necessary to evaluate whether these signals have fractal properties or not. After that, the capability of fractal dimension in classifying spike and noise segments is investigated. Finally, we describe the windowing method that is used for fractal analysis of extracellular signals and discuss about the main parameters of the fractal detector and how to estimate them.

2.6.1. Evaluation of fractal dimension.

Fractal dimension can be considered as a measure of roughness for sets. There are different definitions for fractal dimension among which the Haussdorf dimension is the oldest and may be the most important one. The main advantage of the Haussdorf dimension is that it can be defined for each set. However, in many cases, it is very hard to calculate the Haussdorf dimension [13]. Limitations of Haussdorf dimension together with different insights about the concept of dimension have resulted in other definitions for fractal dimension. For example, the Packing dimension is considered as a dual concept to the Haussdorf dimension [44] and has been used for investigating the dimension of some geometrical sets [45, 46]. However, it is also difficult to calculate it for arbitrary sets and signals. Other definitions of the fractal dimension are more convenient for numerical calculations and signal processing, e.g. correlation dimension [47–50] and information dimension [51, 52]. However, in signal processing, the most frequently used fractal dimension is the box-counting dimension, also known as Minkowski dimension.

Box-counting dimension is computationally efficient and as a result of this, has found numerous applications in signal processing [53–56]. For defining box-counting dimension, we need some preliminary definitions.

Let L be an arbitrary subset of $\mathbb{R}^n$. The diameter of L, represented by D_L, is defined by the largest distance between the points of L

$$D_L = \sup\{\|x - y\| : x, y \in L\}, \qquad (3)$$

where $\|\cdot\|$ is the Euclidean metric function in $\mathbb{R}^n$.

Now, consider a set $F \subset \mathbb{R}^n$. If there are some subsets of $\mathbb{R}^n$ like $L_1, L_2, \ldots, L_k$ with the following two properties

$$\forall\, i \in \{1, 2, \ldots, k\},\ D_{L_i} < \delta, \qquad (4)$$

$$F \subset \bigcup_{i=1}^{k} L_i, \tag{5}$$

then $L_1, L_2, ..., L_k$ are called a δ-cover for F.

For each $\delta > 0$, we find the smallest number of sets that can make a δ-cover for F, and represent it by $M_\delta(F)$.

The box-counting fractal dimensions is defined by

$$D_{\text{Box}}(F) = \lim_{\delta \to 0} \frac{\log(M_\delta)}{-\log(\delta)}, \tag{6}$$

provided that the limit exists.

For a time series, denoted by $S(t)$, we can use a simplified algorithm for evaluating the box-counting dimension [13]. In this algorithm, first $S(t)$ is normalized to fit into the unit square. For each $0 < \delta < 1$, the unit square is transformed to a grid with a size of δ. Then we count the number of grid cells that intersect with the signal and represent this number by N_δ. The grid-based box-counting fractal dimension is denoted by $D'_{\text{Box}}(S(t))$ and is defined by

$$D'_{\text{Box}}(S(t)) = \lim_{\delta \to 0} \frac{\log(N_\delta)}{-\log(\delta)} \tag{7}$$

provided that the limit exists.

Equation (7) can be used for estimating the fractal dimension of time series, like $S(t)$. However, we can also consider $S(t)$ as a subset of $\mathbb{R}^2$. If we denote the two dimensional representation of $S(t)$ by $F(S(t))$

$$F(S(t)) = \{(t, S(t)) : t \in \text{Domain}(S(.))\} \tag{8}$$

Now we can use (6) for estimating the fractal dimension of $F(S(t))$. It is proved in [13] that

$$D'_{\text{Box}}(S(t)) = D_{\text{Box}}(F(S(t))). \tag{9}$$

Therefore, instead of using δ-covers, we can simply employ grids for estimating the box-counting fractal dimension of time series.

In practice, signals have a finite number of samples and it is not meaningful that the grid size tends to zero. In this case, we use an algorithm which works on a finite set of δ values [57]. We have previously used this algorithm in order to enhance the target detection of radar systems [54]. Here, we use it for estimating the fractal dimension of an extracellular signal, $S(n)$. The steps of the algorithm are as follows:

Step 1: Normalize the signal $S(n)$, such that it fits into the unit square.

In this step not only the amplitude of the signal is normalized but also the maximum time index of the signal is set to one.

Step 2: Select a set of grid sizes $\Delta = \{\delta_1, \delta_2, \ldots, \delta_k\}$ such that $\delta_i < \delta_j$ for all $1 \leqslant i < j \leqslant k$.

Step 3: For each i, $i = 1, 2, \ldots, k$, transform the unit square to a grid of size δ_i.

Step 4: Count the number of cells that overlap with the signal and denote this number by N_{δ_i} (figure 4).

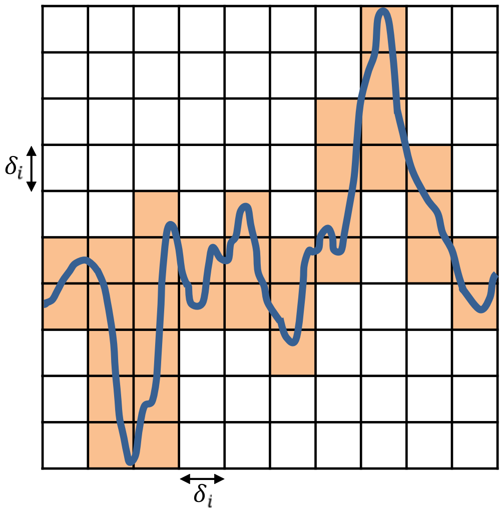

Figure 4. Box counting method. For each δ_i, a grid of size δ_i is constructed and N_{δ_i} is computed by counting the number of cells that overlap with the signal.

Step 5: Consider the set of points P

$$P = \{(-\log(\delta_i), \log(N_{\delta_i})) : i = 1, \ldots, k\}. \tag{10}$$

Using regression analysis, find the optimal line that passes through the points of P. The slope of this line is an estimation of the fractal dimension of $S(n)$.

2.6.2. Fractal property of signals. Although fractal analysis is a strong tool in signal processing, it cannot be utilized for all signals. Thus, we first assess if the signals are good candidates for fractal analysis or not. To do so, the linearity of the plot $\log(N_\delta)$ versus $-\log(\delta)$ is evaluated. If the points are aligned along a straight line, then the signal is a suitable candidate for fractal analysis.

We perform a linear regression analysis on the points and use the coefficient of determination, R^2, as an index for goodness of fit. The index R^2 takes values between 0 and 1 and if its value is close to one, the linear regression is considered as a good fit to the points [58].

In section 3.1.1, we show that both noise segments and spike segments have fractal properties and therefore are good candidates for fractal analysis.

2.6.3. Classification property of fractal dimension. The first motivation for using fractal dimension in spike detection algorithms comes from our intuitive idea that the fractal dimension of a spike segment is different from the fractal dimension of a noise segment. Since the shape of a spike is smoother comparing to the shape of a noise signal, we expect to get a smaller value for the fractal dimension of spike segments relative to the fractal dimension of noise segments. In order to assess our intuitive idea, we calculate the fractal dimension of 10 000 simulated spike and noise segments and compare the histograms of fractal dimensions. In this way, we

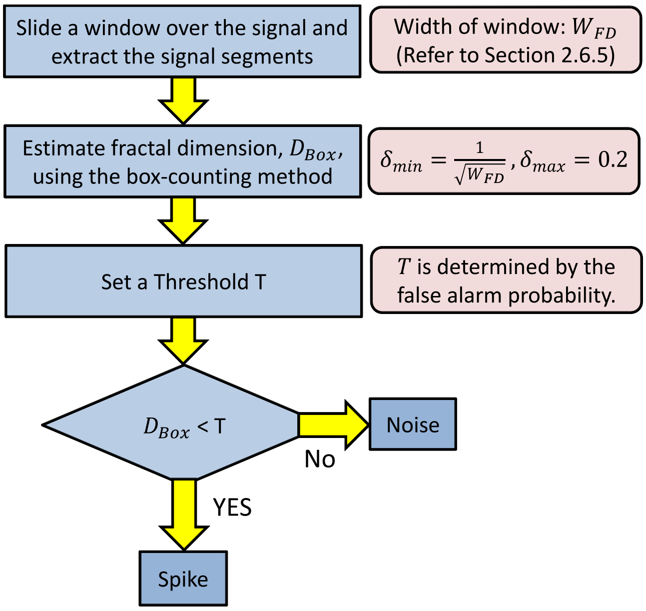

Figure 5. A schematic of the fractal detector.

can assess whether the fractal dimension is a good feature for distinguishing between noise and spikes segments.

The results of the simulation are detailed in section 3.1.2. As we expected, the average fractal dimension of spike segments is smaller than the average fractal dimension of noise segments. We will use this property as the main core of our detection algorithm.

2.6.4. Structure of fractal detector. We have already explained the application of fractal dimension for classification of noise and spike segments. In this part, we will use this feature in order to design our fractal detector.

We scan the signal with a sliding window and extract the segments of the signal for fractal analysis and spike detection. In the following, we describe the steps of the algorithm that we use for the fractal detector:

Step 1: Use a sliding window over the signal for extracting the signal segments. We use a rectangular window of width W_{FD} samples and extract the part of the signal that overlaps with the window. The window slides with a sliding step equal to n_{FD}. Usually, the sliding step is one sample. However, for faster calculations, one may prefer to use a larger sliding step.

Step 2: Calculate the fractal dimension of the extracted segment and record it in a vector of fractal dimensions. We use the algorithm of section 2.6.1 for calculating the box-counting fractal dimension.

Step 3: Use a threshold over the vector of fractal dimensions. The entries of the vector whose values are *less* than the threshold are detected as spikes.

A schematic of the fractal detector is shown in figure 5. We should also mention that the temporal accuracy of the fractal detector is almost half of the width of a spike, i.e. around 0.5–0.7 ms. As an example, we use our suggested fractal detector for the signal in figure 1(b). The efficient performance of fractal detector is shown in figure 1(d) where all five spikes are detected by the fractal detector.

Fractal dimension has been used in combination with a sliding window in different applications [17, 23, 54, 59]. Depending on the stage of normalization, there are two categories of algorithms:

(a) In the first case, we slide the window over the signal and extract a segment of the signal. Then we use the algorithm of section 2.6.1 for evaluating the fractal dimension. Therefore, each segment is normalized independent of the other segments.
(b) In the second case, the whole signal is first normalized and then the window slides over the signal and fractal dimension is estimated without renormalization [23]. In other words, for each extracted segment, the algorithm of section 2.6.1 starts from step 2.

These two categories of algorithms result in very different performance. The selection of the algorithm depends on the nature of the signal and the type of the signal processing task. It is clear from the description that our fractal detector is in the first category.

2.6.5. Parameters of fractal detector. Several parameters should be selected for implementing the fractal detector. In the following, we discuss selection of parameters.

The width of sliding window, W_{FD}, plays an important role in the performance of the fractal detector. On the one hand, for small values of W_{FD}, it is not possible to distinguish between the smoothness differences of spike and noise segments and on the other hand, the time resolution of fractal detector is reduced when W_{FD} is increased. Therefore, it is very important to find the optimal value for the width of sliding window. We evaluate the detection probability of fractal detector for different values of W_{FD}. This evaluation is performed for different powers of thermal noise and inter-spike noise. Using these simulations, we show that for $W_{\mathrm{FD}} = 220$ samples, the fractal detector has an efficient performance in different noise powers. In appendix B, you can find the results of these simulations.

Since the fractal detector uses the algorithm of section 2.6.1, the set of grid sizes, Δ, should be determined. We define,

$$\Delta = \{\delta_{\min}, \delta_{\min} + d, \delta_{\min} + 2d, \ldots, \delta_{\max}\}. \tag{11}$$

For the smallest grid size, $\delta_{\min}$, there should be $\frac{1}{\delta_{\min}}$ samples in each column of the grid so that the signal can potentially cover the whole grid optimally, i.e. one sample for each cell of the grid. In order to satisfy this goal, we assign

$$\delta_{\min} = \frac{1}{\sqrt{W_{\mathrm{FD}}}}. \tag{12}$$

For the upper bound of δ, we can simply set

$$\delta_{\max} = 0.2, \tag{13}$$

which is a typical upper bound for the grid and results in a 5 × 5 grid. The step size of the grid set, d, can be specified by

$$d = \frac{\delta_{\max} - \delta_{\min}}{10}. \tag{14}$$

Another parameter of the fractal detector is the step size of sliding window. This parameter highly affects the computational speed. When we double the step size, the running time is halved. However, when the window slides with larger step sizes, the detection probability is reduced. Therefore, there is a trade-off between computational speed and detection probability. We simulate the effect of step size on detection probability in appendix B. Using the simulation results, one can select a proper value for step size. All the simulations are done in MATLAB on a quad-core computer with 2.4 GHz CPU and 4 GB RAM.

3. Results

In this section, we first investigate the fractal properties of the spike and noise segments in the simulated signal. Then, the efficiency of the fractal dimension as a classifier between the spike and noise segments is analyzed and the performance of the fractal detector is compared with the other detectors.

3.1. Spike detection with the fractal dimension

Here, we show that extracellular signals have fractal properties and therefore, we can use fractal geometry to process them. Also, it is shown that fractal dimension can classify noise and spike segments efficiently.

3.1.1. Fractal properties of extracellular signals. The first step in fractal analysis is to assess if the signals possess fractal properties or not. As mentioned in section 2.6.2, a signal is suitable for fractal analysis if the points

$$P = \{(-\log(\delta_i), \log(N_{\delta_i})) : i = 1, \ldots, k\}, \tag{15}$$

are well fitted by a straight line.

We need to study the fractal properties of the noise and spike segments separately. In figure 6, we plot $\log(N_\delta)$ against $-\log(\delta)$ for typical spike and noise segments. It is seen in both cases that the linear regression (the red dashed line) fits the points very well. The coefficient of determination, R^2, equals to 0.92 and 0.976 for the spike and noise segment respectively. This proves that both spike and noise segments of the simulated extracellular signal have fractal properties, and the signal can be used for fractal analysis.

3.1.2. Classification capability of fractal dimension. We study the distribution of fractal dimension for noise and spike segments in low and high noise regimes. The noise parameters for the low noise regime are $\sigma_{\mathrm{ISN}} = 0.02$ and $\sigma_{\mathrm{TN}} = 0.002$ and for the case of high noise regime, $\sigma_{\mathrm{ISN}} = 0.035$ and $\sigma_{\mathrm{TN}} = 0.005$.

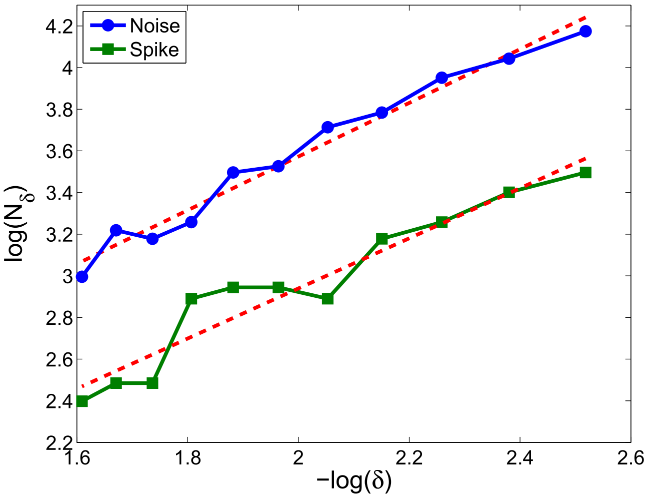

Figure 6. Fractal property of the simulated signal. We plot $\log(N_\delta)$ as a function of $-\log(\delta)$ for a typical spike and noise segment. The red dashed lines are fitted to the data using linear regression.

We generate 10 000 spike and noise segments and calculate the fractal dimension of each segment. Then, the histogram of fractal dimension is evaluated for spike and noise segments. In figure 7(a), we show the histograms for low noise regime. The mean and variance of the fractal dimension of noise segments are $\mu_{\mathrm{noise}} = 1.46$ and $\sigma_{\mathrm{noise}} = 0.046$. For spike segments, the mean and variance of the fractal dimension are $\mu_{\mathrm{spike}} = 1.24$ and $\sigma_{\mathrm{spike}} = 0.035$. We repeat the same procedure for high noise regime. The histograms of fractal dimension are shown in figure 7(b). In this case, we have $\mu_{\mathrm{noise}} = 1.46$, $\sigma_{\mathrm{noise}} = 0.046$, $\mu_{\mathrm{spike}} = 1.32$ and $\sigma_{\mathrm{spike}} = 0.041$.

The significant difference between μ_{noise} and μ_{spike} approves our hypothesis that the average fractal dimension of spike segments is smaller than the average fractal dimension of noise segments. The fractal detector uses this difference to detect spikes in extracellular signals.

3.2. Performance analysis of the fractal detector

In this part, we present the main results of the paper. The performance of our suggested fractal detector is compared with the performance of the threshold detector, the average matched-filter detector and the wavelet-PCA detector. Since there are some free parameters in the wavelet-PCA detector and the fractal detector, we need to find the optimal values of these variables (see appendix).

We consider the detection probability as a function of the noise power, the false alarm probability and some other parameters and in each case, compare the performance of the detectors.

3.2.1. Detection probability against noise power. Here, we fix the false alarm probability and compare the performance of the detectors for different noise powers. To analyze the effect

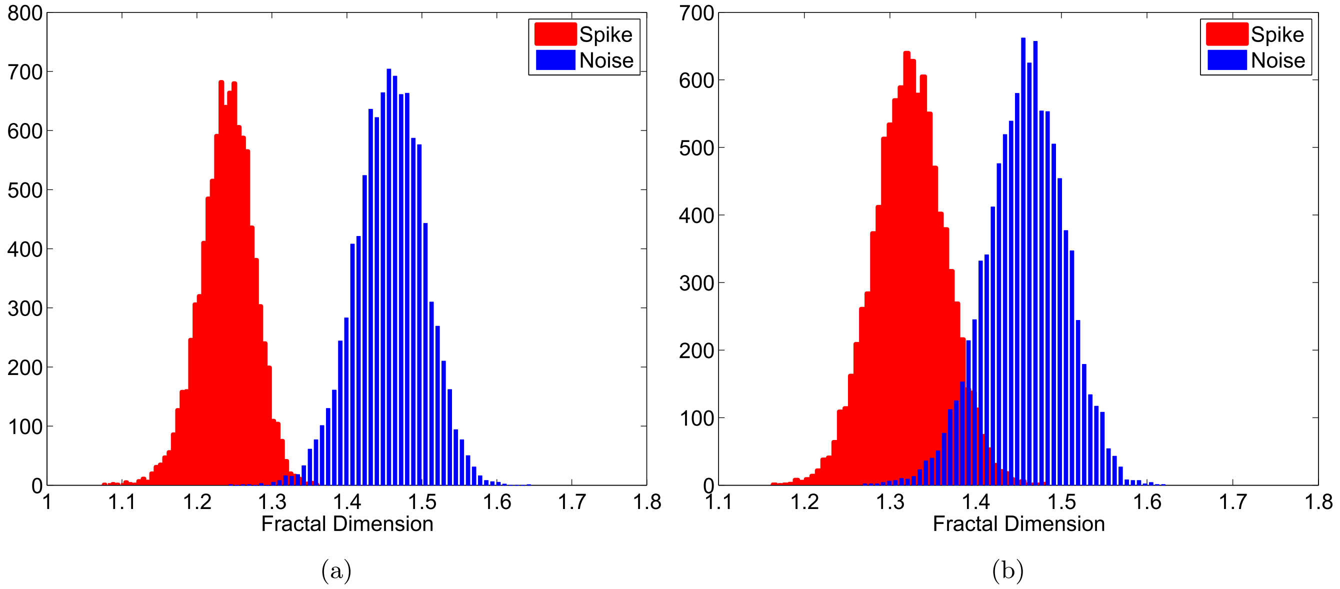

Figure 7. Histogram of fractal dimension for spike and noise segments. (a) Low noise regime: inter-spike noise level $\sigma_{\mathrm{ISN}} = 0.02$ and thermal noise level $\sigma_{\mathrm{TN}} = 0.002$, (b) High noise regime: inter-spike noise level $\sigma_{\mathrm{ISN}} = 0.035$ and thermal noise level $\sigma_{\mathrm{TN}} = 0.005$.

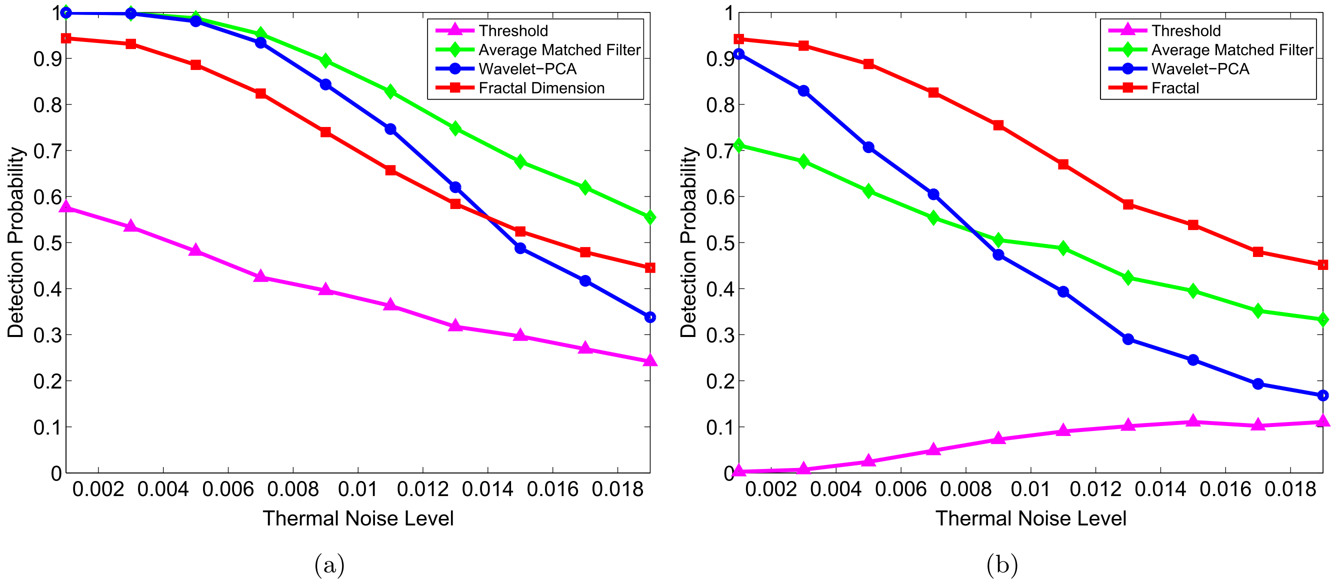

Figure 8. Detection probability as a function of thermal noise power for different spike detectors. The level of inter-spike noise is set to (a) $\sigma_{\mathrm{ISN}} = 0.030$, (b) $\sigma_{\mathrm{ISN}} = 0.035$.

of inter-spike noise and thermal noise independently, we simulate two different cases. In the first case, detection probability is calculated for different thermal noise powers, keeping the inter-spike noise power constant. For the second case, detection probability is plotted against inter-spike noise power for a constant thermal noise power. In the following, we present the simulation results for these two cases.

For simulating the first case, we set the false alarm probability to $P_{\mathrm{fa}} = 0.2$ and inter-spike noise power is fixed at $\sigma_{\mathrm{ISN}} = 0.03$. In figure 8(a), the detection probability, P_{d}, is shown as a function of thermal noise power. The performance of the average matched filter detector is better than the other detectors. However, the orders are changed when we increase the level of inter-spike noise to $\sigma_{\mathrm{ISN}} = 0.035$. In figure 8(b), we have plotted detection probability as a function of thermal noise level for $\sigma_{\mathrm{ISN}} = 0.035$. The superiority of fractal detector for high noise levels is clearly demonstrated in this Figure.

Moreover, we see that the wavelet-PCA detector and average matched filter detector both have a better performance than the threshold detector. Also, the performance of wavelet-PCA detector is better than the performance of average matched filter in lower noise levels, but when noise power increases, their order is reversed.

We should also explain the unusual behavior of threshold detector in these simulations. For threshold detector, the

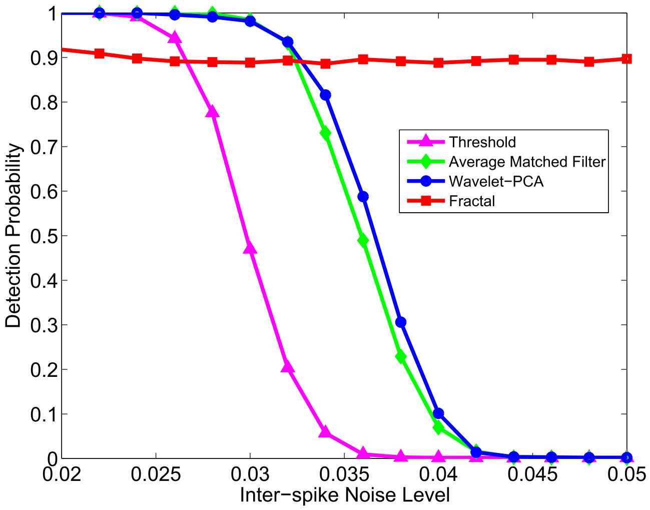

Figure 9. Detection probability as a function of the level of inter-spike noise for different spike detectors. Thermal noise level is fixed at $\sigma_{\mathrm{TN}} = 0.005$.

detection probability is increased by increasing the level of thermal noise. Since inter-spike noise level is high, the detection probability of the threshold detector is around zero for small thermal noise levels. However, when we increase the level of thermal noise, the added noise can help some of the buried spikes to cross the threshold and this results in a slight increase of detection probability.

For simulating the second case, we evaluate the detection probability of detectors as a function of inter-spike noise power (figure 9). In this simulation, false alarm probability is $P_{\mathrm{fa}} = 0.2$ and the level of thermal noise is fixed at $\sigma_{\mathrm{TN}} = 0.005$.

The plot shows two main advantages of fractal detector:

(1) The performance of the fractal detector is much better than the other detectors in high inter-spike noise powers (low SNR signals).
(2) The performance of the fractal detector is almost independent of the inter-spike noise power.

Compared to the other three detectors, this is a unique characteristic of fractal detector. The reason is that the fractal detector is based on the fractal dimension of normalized signal segments. Therefore, when the inter-spike noise power is increased, the fractal dimension does not change significantly and as a result of this, the performance of the fractal detector does not degrade notably. In contrast to the fractal detector, the increase of the inter-spike noise power influences the wavelet coefficients and the output of the average-matched filter and results in a decline in the performance of these detectors.

3.2.2. Detection probability against false alarm probability.

In our simulations, the false alarm probability is varied between 0.01 and 0.4 and detection probability is evaluated for each detector. We derive detection probability as a function of false alarm probability for two different inter-spike noise powers that correspond to the values used in figures 8(a) and (b).

In the first case, we set $\sigma_{\mathrm{TN}} = 0.008$ and $\sigma_{\mathrm{ISN}} = 0.030$. The performance of the four detectors is shown in figure 10(a). When we decrease the false alarm probability, we can see the superiority of the fractal detector.

In the second case, we keep thermal noise power at the same level, $\sigma_{\mathrm{TN}} = 0.008$, and increase inter-spike noise power to $\sigma_{\mathrm{ISN}} = 0.035$. For all values of false alarm probability, the fractal detector has the best performance among the four detectors. Also, the performance difference is higher for smaller values of false alarm probability.

3.2.3. The effect of noise bandwidth.

Since fractal detector is based on the irregularity of noise, the bandwidth of noise is a critical parameter for the performance of fractal detector. In the following, we assess the effect of noise bandwidth.

In section 2.1, we explained that inter-spike noise is modeled by passing a white Gaussian noise through a low-pass filter. The bandwidth of this filter is the parameter that is used in our simulations. Inter-spike noise is a model for spiking activity of close neighboring neurons. Hence, the bandwidth of inter-spike noise corresponds to the density of neurons that are around the main neuron. When the density is high, the bandwidth and irregularity of inter-spike noise is higher. Conversely, if the density of surrounding neurons is low, the neuronal activity is smoother and the bandwidth of the inter-spike noise is lower.

We investigate the effect of bandwidth by calculating detection probability as a function of inter-spike noise bandwidth. The noise levels are fixed at $\sigma_{\mathrm{TN}} = 0.005$ and $\sigma_{\mathrm{ISN}} = 0.035$. The simulation result is shown in figure 11. We find that noise bandwidth has reverse effects on the fractal detector and the other detectors. When we increase the bandwidth of inter-spike noise, the performance of fractal detector is enhanced while for the other detectors, the performance declines.

This result is consistent with the nature of fractal detector. When we increase the inter-spike noise bandwidth, the fractal dimension of noise segments is elevated and it gets easier to classify spike segments and noise segments. This leads to a higher performance for fractal detector.

3.2.4. The influence of spike shapes.

In the following, we analyze the dependence of spike detection algorithms on the shape of spikes. We consider a set of 16 extracellular spikes with different shapes and normalize them so that all of them have the same power. The normalized spike shapes are shown in figure 12(a).

For this analysis, it is more reasonable to normalize the performance of all detectors. We fix thermal noise power at $\sigma_{\mathrm{TN}} = 0.005$ and use the first spike shape for normalization. We change the value of σ_{ISN} in order to reach the same detection probability for all detectors. From figure 9, it is found that by setting $\sigma_{\mathrm{ISN}} = 0.033$, the fractal detector has almost the same detection probability as the wavelet-PCA detector and the average matched filter detector. A value of

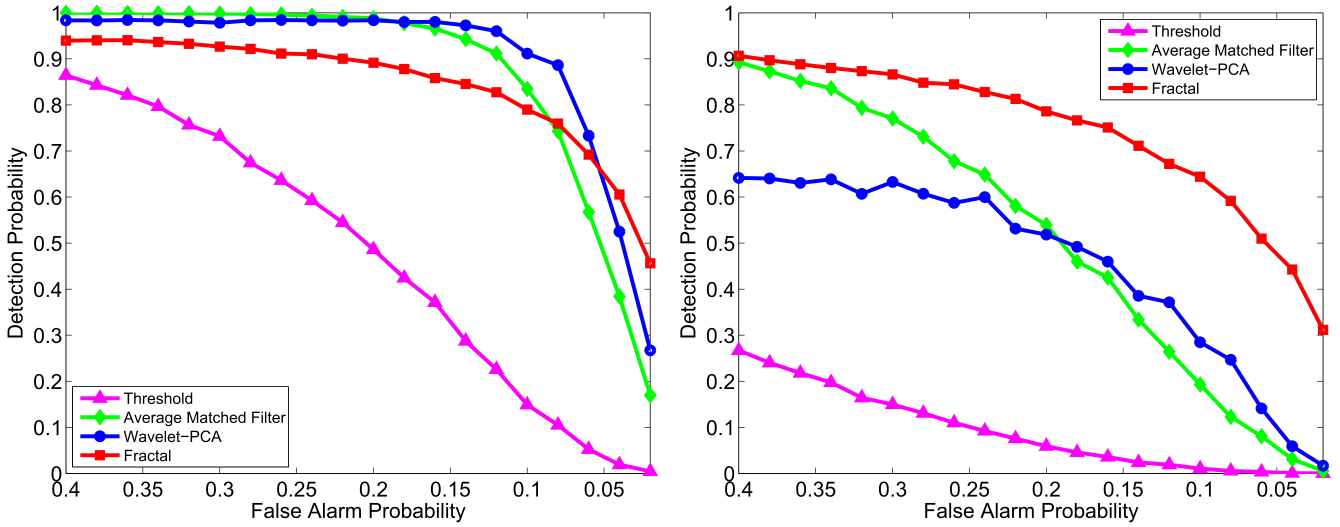

(a) (b)

Figure 10. Detection probability versus false alarm probability for different spike detectors. The level of thermal noise is fixed at $\sigma_{\mathrm{TN}} = 0.008$ and the level of inter-spike noise is set to (a) $\sigma_{\mathrm{ISN}} = 0.030$, (b) $\sigma_{\mathrm{ISN}} = 0.035$.

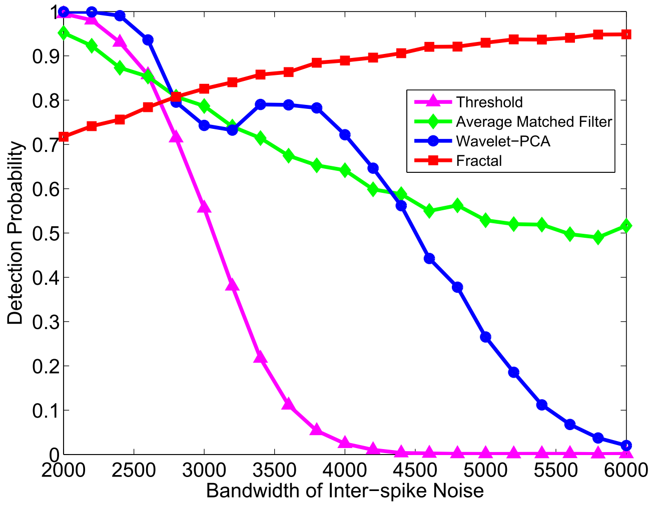

Figure 11. Detection probability of spike detectors as a function of the bandwidth of inter-spike noise for thermal noise level $\sigma_{\mathrm{TN}} = 0.005$ and inter-spike noise level $\sigma_{\mathrm{ISN}} = 0.035$.

$\sigma_{\mathrm{ISN}} = 0.028$ is used for the threshold detector in order to achieve the same detection probability.

Now, for each of the 16 spike shapes, we estimate the detection probability of spike detectors. The detection probability as a function of spike shape index is shown in figure 12(b). The performance of fractal detector is almost independent of the spike shapes, but the other detectors are highly dependent on the index of spike shape and for some spike shapes, there is a large decline in their performance. This simulation proves another important advantage of fractal detector.

3.2.5. Performance analysis on experimental data. We use a publicly available dataset from the Buzsaki Lab (Dataset number: d533101) [60]. The dataset contains simultaneous intracellular and extracellular recordings in the hippocampus of anesthetized rats [37]. The intracellular channel is used to evaluate the accuracy of the algorithms that are employed for spike detection in the extracellular channel.

First we assess the fractal properties of the noise and spike segments of the experimental data. The spikes are specified using the spike timing information in the intracellular channel, and the noise segments are distinguished by their amplitudes. In figure 13, we plot $\log(N_\delta)$ as a function of $-\log(\delta)$ for a typical spike and noise segment of the experimental signal. The dashed red lines show the fitted regression lines to the data. The coefficient of determination, R^2, for the spike segment and the noise segment is equal to 0.96 and 0.99 respectively. This proves that the spike and noise segments are fractal signals. Moreover, the fractal dimension of the spike segment is 1.16 while the fractal dimension of the noise segment is 1.39. We conclude that the experimental signal is a fractal, and the fractal detector can be used for spike detection.

The SNR of the original recording is high (5 dB) and all spikes can be detected by a threshold. We attenuate the power of spike segments of the extracellular channel in order to study the performance of the algorithms for different values of SNR. First, the spike segments are determined using the intracellular channel, and then the corresponding spike segments of the extracellular channel are multiplied by an attenuation coefficient. We can create different levels of signal to noise ratio in the extracellular signal by changing the value of the coefficient.

Figure 14 shows the detection probability of the detectors as a function of SNR. It is demonstrated that the fractal detector has the best performance for low SNR regimes. Also, we see that the performance of the fractal detector does not vary a lot by decreasing the SNR. By comparing this figure with figure 9, we conclude that the performance results of experimental data are consistent with the simulation results.

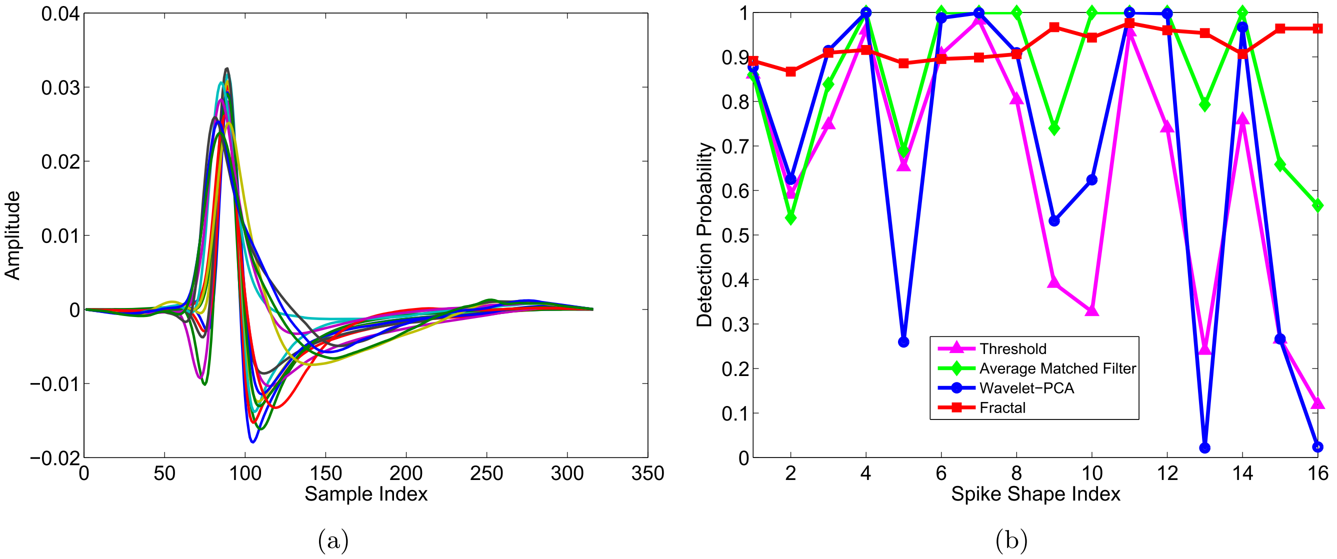

Figure 12. The effect of different spike shapes on the performance of spike detectors. (a) Selected spike shapes after power normalization. (b) Detection probability as a function of spike shape index for different spike detectors. Different inter-spike noise powers have been used for detectors in order to normalize the performances for the first index of spike shapes.

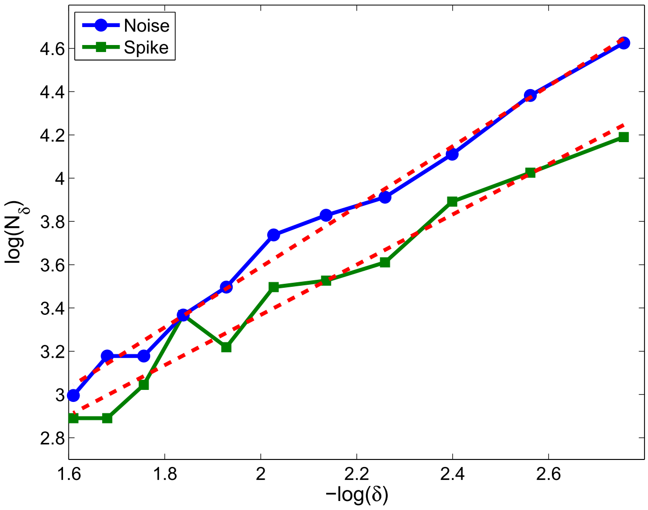

Figure 13. Fractal property of the experimental data. We plot $\log(N_\delta)$ as a function of $-\log(\delta)$ for a typical spike and noise segment. The red dashed lines are fitted to the data using linear regression.

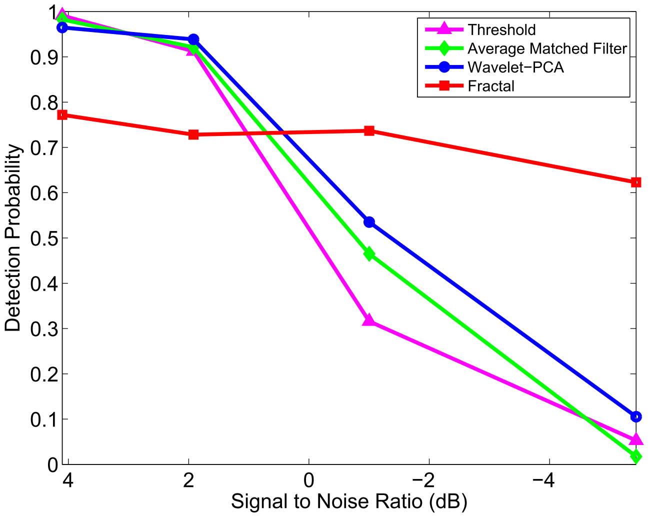

Figure 14. Performance analysis of spike detection algorithms for experimental data. Detection probability is plotted as a function of SNR for different spike detection algorithms.

4. Discussion

We presented a new spike detection algorithm based on fractal dimension to detect spikes in extracellular recordings. We were interested in a specific category of spikes to which we referred as semi-intact spikes. We suggested an algorithm to simulate extracellular signals with this category of spikes and employed the simulated signal to evaluate the performance of spike detectors.

First, we demonstrated that extracellular recordings have fractal properties and are proper candidates for fractal analysis. Fractal dimension of spike and noise segments was calculated and it was shown that spike segments have a smaller fractal dimension than noise segments. This feature was used as the core of fractal detector.

We confined comparison of the fractal detector to three of the most common detection algorithms (threshold detector, average matched filter detector, and wavelet-PCA detector), while being aware of the others in the literature [61–63]. For low SNR signals, we showed that the fractal detector has the best performance among these detectors. We repeated the same study on experimental datasets and demonstrated that the results are consistent with simulation results. Another important feature of the fractal detector is that its performance is independent of inter-spike noise power. This characteristic distinguishes the fractal detector from other detectors.

We conclude that the fractal detector is an efficient method for detecting semi-intact spikes in extracellular recordings. However, more elaborate algorithms are needed for detecting compound spikes (refer to appendix C). The fractal detector is not necessarily a stand-alone detector. It is a processing block that can be combined easily with other spike detection and spike sorting algorithms.

Fractal dimension has been used for detection of changing patterns, including spikes, in EEG signals [22, 23]. But our approach is different from these papers in several aspects. In these papers, fractal dimension is used for analyzing recorded EEG data. It is shown that the spikes that are detectable by an expert can also be detected by fractal dimension analysis. However precise spike timing is not known for real data and as a result of this, the detection performance of the method cannot be evaluated accurately. Without a good estimate of detection probability, it is also impractical to compare fractal analysis with other detection algorithms. The other distinction is in the stage of normalization. As we mentioned in section 2.6.4, our fractal detector belongs to the category of algorithms in which each extracted segment is normalized independent of the other segments. However, detectors described in [22, 23] are based on normalizing the whole signal before applying the sliding window. Using our suggested method, we can detect low-amplitude spikes without the false detection of silent periods. Moreover, we use box-counting method for estimating the fractal dimension, while in [22], fractal dimension is calculated using the Katz method which is based on the length of the curve. In the Katz method, the successive samples are connected with a straight line and the length of the curve is estimated by adding up the length of the lines. The advantage of box-counting method is that there is no prior assumption about the behavior of the signal between two successive samples. Finally, we should note that EEG signals have a completely different nature from extracellular signals and specific detectors should be designed for each case.

Although in low SNR the fractal detector has the best performance among the four detectors, it needs more computational time. We suggested to increase the step size of sliding window in order to reduce the running time and showed that the sliding step can be increased by a factor of 10 without a tangible degradation of performance (see figure 18 in appendix).

There are also some algorithms for fast calculation of fractal dimension [64, 65]. However, for using these algorithms, it is necessary to verify that these algorithms do not reduce the performance of the fractal detector.

We also analyzed the effect of the noise bandwidth on the performance of spike detectors. While increasing the noise bandwidth enhances the performance of the fractal detector, the performance of other spike detectors is degraded. A lesson from this simulation is that the interfering effect of noise is not a sufficient reason for filtering the noise. When we use a low-pass filter, the noise power is reduced but at the same time, the noise segments get smoother. This makes the distinction between spike and noise segments more difficult for the fractal detector. Without filtering, the rough and irregular structure of noise segments results in a larger fractal dimension and improves spike detection.

Filtering is an important issue in extracellular recordings. In most cases, the recorded data is filtered in the first stage of processing, but from the point of view of fractal analysis, valuable information is lost with low-pass filtering. In fractal analysis, instead of removing noise as a source of interference, we use the properties of noise to detect spikes. Therefore it is strongly recommended to use the raw data for fractal analysis and avoid the pre-processed and filtered data.

Acknowledgments

This work was supported by grant 01EO0901 of German Center for Vertigo and Balance Disorders, Ludwig-Maximilian University of Munich.

Appendix

A. Optimization of wavelet-PCA detector

Here, we find the optimal threshold for the wavelet-PCA detector and study the efficiency of the extracted feature from the wavelet-PCA algorithm. Also the influence of adding more PCA components on the performance of the detector is analyzed.

A.1. Estimation of threshold

In the first stage of the wavelet-PCA detector, we need to set a threshold for the signal. The value of this threshold plays an important role in the performance of the detector. We define the threshold, A, using the standard deviation of signal, σ_S. In simplest case

$$A = k \times \sigma_S, \tag{16}$$

where k is called the *threshold coefficient*.

In order to find the optimal value of threshold coefficient, we calculate the detection probability of wavelet-PCA algorithm as a function of threshold coefficient in two cases:

(1) We fix the thermal noise power ($\sigma_{TN} = 0.015$) and for some inter-spike noise powers, evaluate the detection probability as a function of threshold coefficient (figure 15(a)). In this figure, the dashed line connects the maximum values of the curves.

(2) In this case, the power of inter-spike noise is fixed ($\sigma_{ISN} = 0.02$) and for some power values of thermal noise, detection probability is evaluated for different threshold coefficients (figure 15(b)). Again, the maximum values of the curves are connected by a dashed line.

From figures 15(a) and (b), we find that a good choice for threshold coefficient is $k = 2.5$.

A.2. Efficiency of extracted feature

In the wavelet-PCA detector, we use PCA to extract a feature from wavelet coefficient of signal segments. As mentioned before, the feature is the first component of the PCA. We demonstrate the performance of the extracted feature by

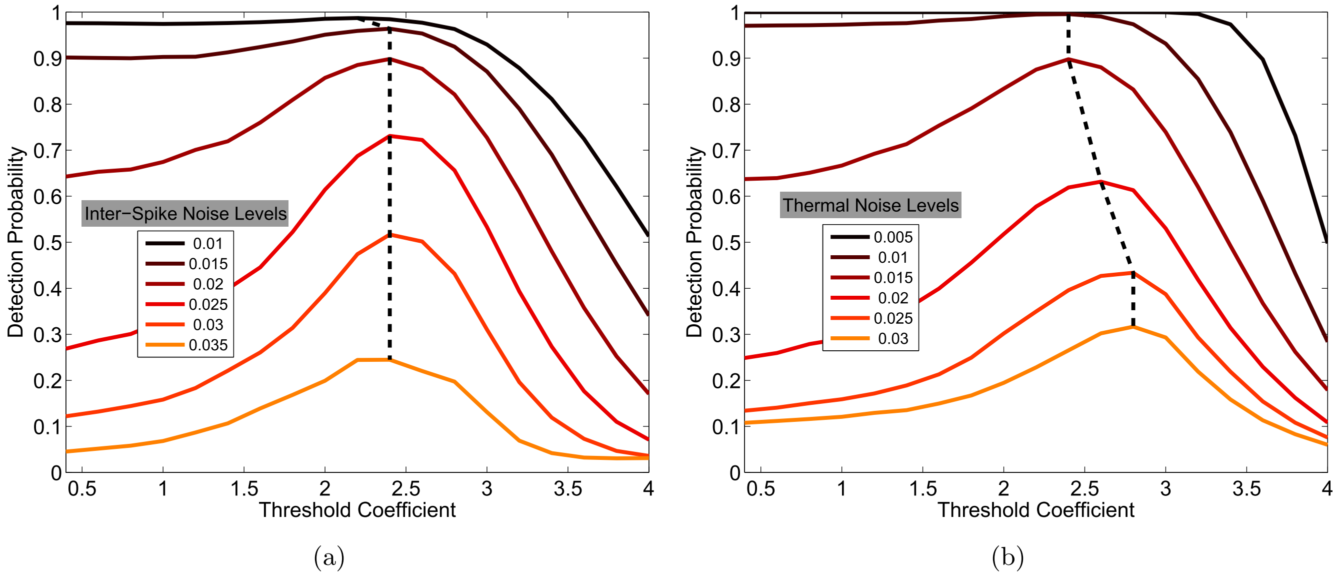

Figure 15. Detection probability as a function of threshold coefficient. (a) Power of thermal noise is fixed at $\sigma_{\mathrm{TN}} = 0.015$ and different inter-spike noise powers are simulated. (b) Power of inter-spike noise is fixed at $\sigma_{\mathrm{ISN}} = 0.02$ and the simulation is done for some thermal noise powers. The dashed line connects the maximum values of the curves.

comparing the histogram of feature values for spike and noise segments. We consider two different noise regimes: a low noise regime in which $\sigma_{\mathrm{ISN}} = 0.02$ and $\sigma_{\mathrm{TN}} = 0.002$ and a high noise regime with $\sigma_{\mathrm{ISN}} = 0.035$ and $\sigma_{\mathrm{TN}} = 0.005$.

In figure 16(a), we analyze the first component of PCA for the low noise regime. The histogram of feature values for spike and noise segments are shown in red and blue colors respectively. Then we repeat the same simulation for the high noise regime and the result is shown in figure 16(b). The extracted feature (first component of PCA) separates spike and noise segments efficiently.

A.3. Sufficiency of the first component of PCA

One way of improving the detection probability might be using more components of the PCA. However, we show graphically that this is not the case in our model and increasing the number of components does not necessarily enhance the performance.

We include the second component of PCA into the classification algorithm which produces a two dimensional feature. Each segment of the signal is represented by two numbers corresponding to the first and second coordinates of the segment in the PCA space. Therefore, we can represent each segment by a point in two-dimensional space. As before we perform the simulations for two different noise regimes. Figures 16(c) and (d) show the segments of the signal in this space for low and high noise powers. The horizontal axis corresponds to the first PCA component (main extracted feature) and the vertical axis shows the second PCA component of the segments (extra feature).

In both cases, a vertical line is the best classifier between spike and noise segments. In other words, the second component of PCA (extra feature) does not provide more information for enhancing the classification. Therefore, we use only the first component of PCA as the classification feature.

B. Optimization of the fractal detector

The width of the sliding window, W_{FD}, plays an important role in the performance of fractal detector. In order to choose a proper value for W_{FD}, we calculate the detection probability as a function of W_{FD} for different noise powers.

First we fix the power of thermal noise at $\sigma_{\mathrm{TN}} = 0.005$ and calculate detection probability as a function of W_{FD} for some inter-spike noise powers (figure 17(a)). The dashed line connects the maximum values of the curves.

Then the inter-spike noise power is kept constant at $\sigma_{\mathrm{ISN}} = 0.01$. In figure 17(b), we plot detection probability as a function of W_{FD} for different levels of thermal noise. Again we connect the maximum values of the curves by a dashed line.

From figures 17(a) and (b), we deduce that $W_{\mathrm{FD}} = 220$ is a convenient value for the width of the sliding window.

Another parameter of the fractal detector is the step size of sliding window. It is clear that the highest detection probability is achieved when the step size is equal to one sample. If computational speed matters, we can consider larger step sizes. This parameter changes the processing time significantly. For example, changing the step size from 1 to 10 divides the computing time by 10. However, the fractal detector still needs more running time comparing with the other three detectors. If we run the spike detection algorithm for a signal with a duration of 1 s and sampling frequency of 50 kHz, then the running time for different algorithms is as follows: Threshold detector: 0.05 s. Average matched filter: 0.1 s, Wavelet-PCA detector: 0.5 s, Fractal detector (with a slide step of 10) = 3 s.

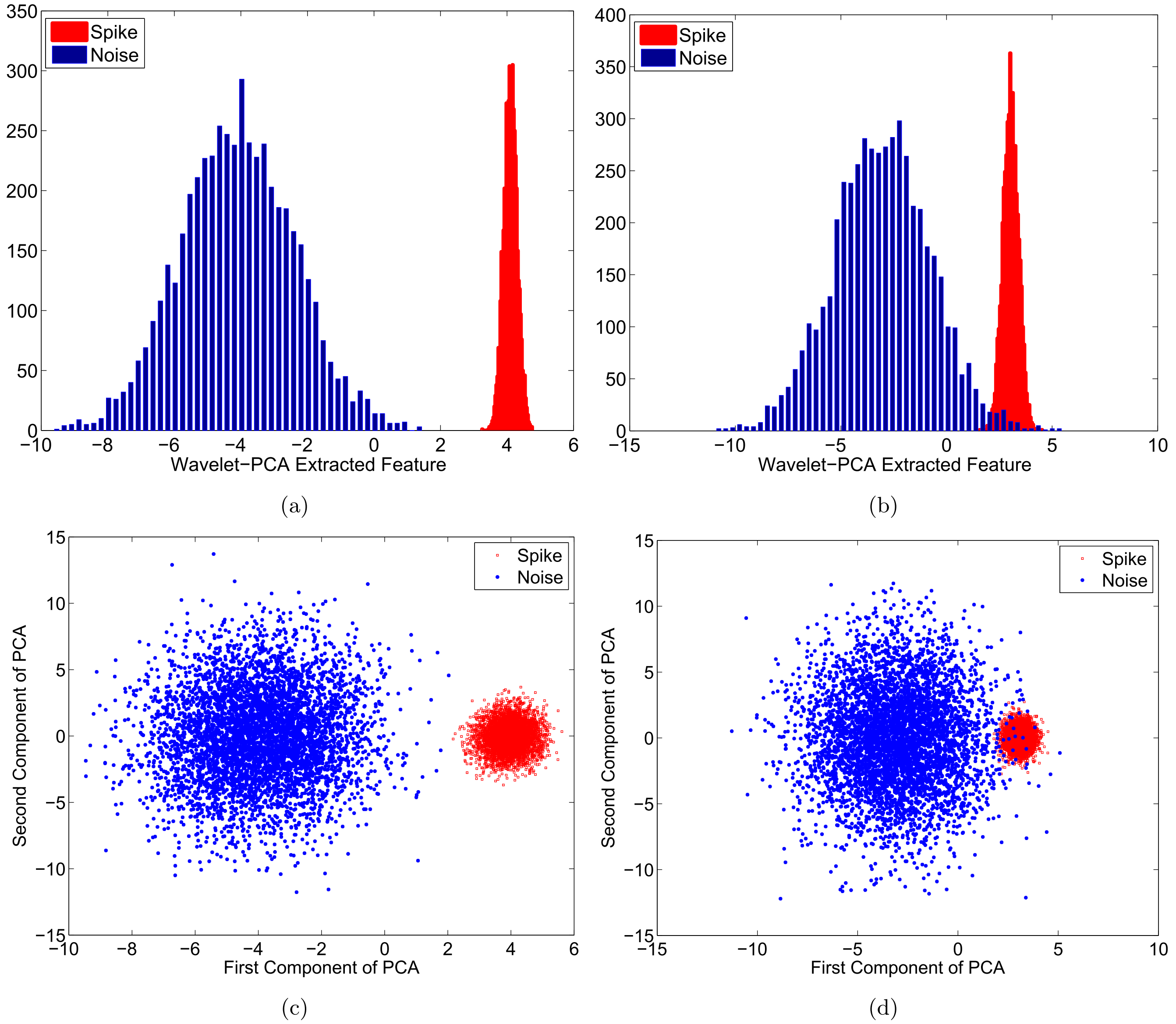

(a) (b)

(c) (d)

Figure 16. The effect of selecting one component or two components of PCA in low noise and high noise regimes. The low noise regime corresponds to inter-spike noise level $\sigma_{\mathrm{ISN}} = 0.02$ and thermal noise level $\sigma_{\mathrm{TN}} = 0.002$ and for high noise regime, inter-spike noise level $\sigma_{\mathrm{ISN}} = 0.035$ and thermal noise level $\sigma_{\mathrm{TN}} = 0.005$. (a) One Component (low noise regime): the histogram of the main component for spike and noise segments is shown. (b) One component (high noise regime). (c) Two Components (low noise regime): segments of the signal are shown in two-dimensional PCA space. The horizontal axis is the first component of PCA and the vertical axis is the second component. (d) Two Components (high noise regime).

To analyze the effect of larger step sizes on the performance of fractal detector, we calculate detection probability as a function of step size. In figure 18, we show the result of simulation for different levels of thermal noise. The power of inter-spike noise is kept constant at $\sigma_{\mathrm{ISN}} = 0.03$

This simulation demonstrates the compromise between detection probability and the running time of the algorithm. Also, it is seen that we can select a sliding step of size 10 without a significant decrease of detection probability.

C. Detection of compound spikes

When the neuronal activity of neighboring neurons arrives at the extracellular electrode simultaneously, the signals interfere with each other, and the extracellular spike shapes are distorted. These spikes are known as compound spikes. The detection of compound spikes needs more elaborate algorithms and is not the topic of this paper. However, we can compare the performance of the fractal detector with the other three detectors in detecting compound spikes. In figure 19, the detection probability of compound spikes is plotted as a function of the interference level. When the level of interference is increased, the spike shapes are more distorted and it is harder to distinguish between the geometric shapes of spike and noise segments. Although the performance of the detectors is not satisfactory in this case, still we can see that the fractal detector has the best performance for high levels of interference.

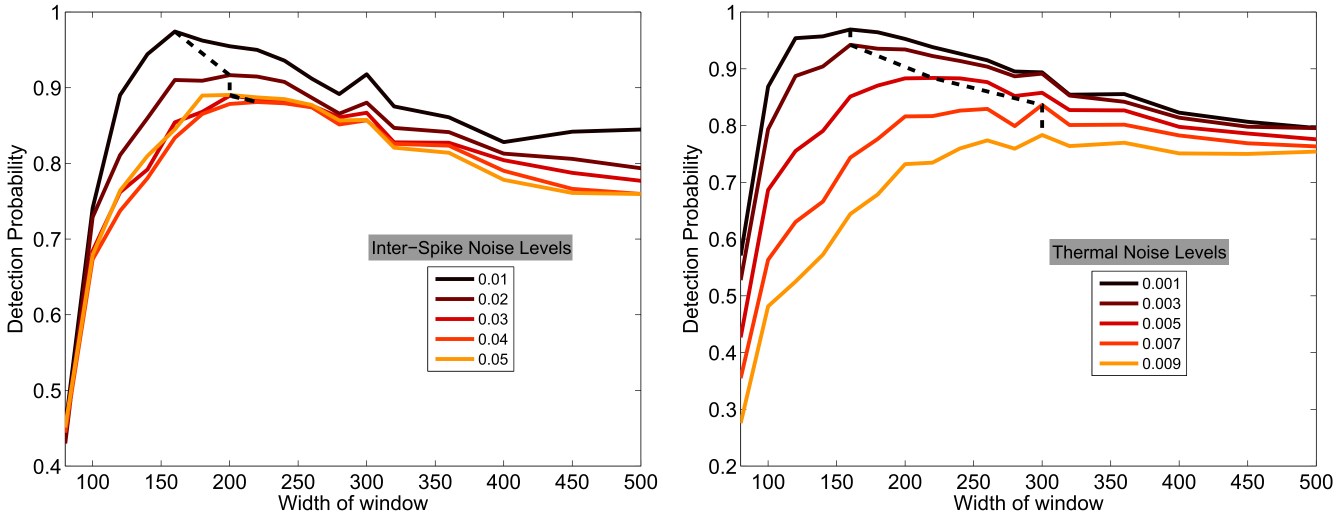

(a) (b)

Figure 17. Detection probability against the width of sliding window, (a) for different levels of inter-spike noise, (b) for different levels of thermal noise. The dashed line connects the maximum values of curves.

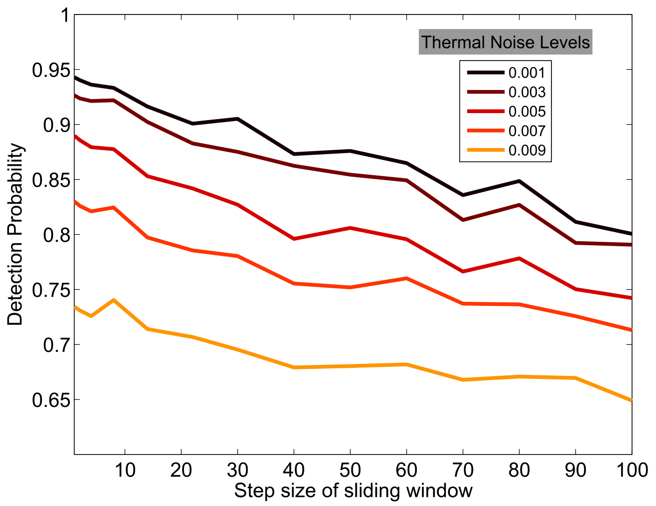

Figure 18. The effect of the step size of sliding window on the detection probability, for different levels of thermal noise.

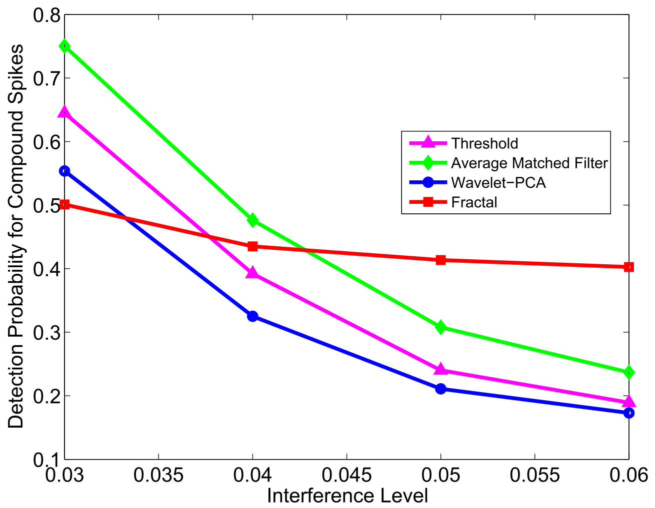

Figure 19. Performance analysis of spike detection algorithms for compound spikes. Detection probability is plotted as a function of interference level for different spike detection algorithms.

References

[1] Lewicki M S 1998 A review of methods for spike sorting: the detection and classification of neural action potentials *Netw., Comput. Neural Syst.* **9** R53–78

[2] Guillory K and Normann R 1999 A 100-channel system for real time detection and storage of extracellular spike waveforms *J. Neurosci. Methods* **91** 21–9

[3] Takahashi S, Anzai Y and Sakurai Y 2003 Automatic sorting for multi-neuronal activity recorded with tetrodes in the presence of overlapping spikes *J. Neurophysiol.* **89** 2245–58

[4] Lewicki M S 1994 Bayesian modeling and classification of neural signals *Neural Comput.* **6** 1005–30

[5] Nicolelis M A 2007 *Methods for Neural Ensemble Recordings* (Boca Raton, FL: CRC Press)

[6] Kim S and McNames J 2007 Automatic spike detection based on adaptive template matching for extracellular neural recordings *J. Neurosci. Methods* **165** 165–74

[7] Obeid I and Wolf P D 2004 Evaluation of spike-detection algorithms for a brain–machine interface application *IEEE Trans. Biomed. Eng.* **51** 905–11

[8] Adamos D A, Kosmidis E K and Theophilidis G 2008 Performance evaluation of PCA-based spike sorting algorithms *Comput. Methods Programs Biomed.* **91** 232–44

[9] Abeles M and Goldstein M H Jr 1977 Multispike train analysis *Proc. IEEE* **65** 762–73

[10] Chitaliya N G and Trivedi A 2010 Feature extraction using wavelet-PCA and neural network for application of object classification and face recognition *2nd Int. Conf. on Computer Engineering and Applications (ICCEA)* vol 1 (Piscataway, NJ: IEEE) pp 510–4

[11] Gupta M R and Jacobson N P 2006 Wavelet principal component analysis and its application to hyperspectral images *IEEE Int. Conf. on Image Processing* (Piscataway, NJ: IEEE) pp 1585–8

[12] Mandelbrot B B 1983 *The Fractal Geometry of Nature* (London: Macmillan)

[13] Falconer K 2013 *Fractal Geometry Mathematical Foundations and Applications* (New York: Wiley)

[14] Lo T, Leung H, Litva J and Haykin S 1993 Fractal characterisation of sea-scattered signals and detection of sea-surface targets *IEE Proc. Radar and Signal Processing (IET)* vol 140, pp 243–50

[15] Baish J W and Jain R K 2000 Fractals and cancer *Cancer Res.* **60** 3683–8

[16] Wardlaw G, Wong R and Noseworthy M D 2008 Identification of intratumour low frequency microvascular components via bold signal fractal dimension mapping *Phys. Medica* **24** 87–91

[17] Esteller R, Vachtsevanos G, Echauz J, Henry T, Pennell P, Epstein C, Bakay R, Bowen C and Litt B 1999 Fractal dimension characterizes seizure onset in epileptic patients *IEEE Int. Conf. on Acoustics, Speech, and Signal Processing* vol 4 (Piscataway, NJ: IEEE) pp 2343–6

[18] Acharya R U, Faust O, Kannathal N, Chua T and Laxminarayan S 2005 Nonlinear analysis of EEG signals at various sleep stages *Comput. Methods Programs Biomed.* **80** 37–45

[19] Klonowski W, Olejarczyk E, Stepien R, Jalowiecki P and Rudner R 2006 Monitoring the depth of anaesthesia using fractal complexity method *Complexus Mundi Emergent Patterns in Nature* pp 333–42

[20] Liu Y, Sourina O and Nguyen M K 2010 Real-time EEG-based human emotion recognition and visualization *Int. Conf. on Cyberworlds (CW)* (Piscataway, NJ: IEEE) pp 262–9

[21] Zhang L, Liu J Z, Dean D, Sahgal V and Yue G H 2006 A three-dimensional fractal analysis method for quantifying white matter structure in human brain *J. Neurosci. Methods* **150** 242–53

[22] Pradhan N and Narayana Dutt D 1993 Use of running fractal dimension for the analysis of changing patterns in electroencephalograms *Comput. Biol. Med.* **23** 381–8

[23] Arle J E and Simon R H 1990 An application of fractal dimension to the detection of transients in the electroencephalogram *Electroencephalogr. Clin. Neurophysiol.* **75** 296–305

[24] Holt G R and Koch C 1999 Electrical interactions via the extracellular potential near cell bodies *J. Comput. Neurosci.* **6** 169–84

[25] Pettersen K H, Hagen E and Einevoll G T 2008 Estimation of population firing rates and current source densities from laminar electrode recordings *J. Comput. Neurosci.* **24** 291–313

[26] Smith L S and Mtetwa N 2007 A tool for synthesizing spike trains with realistic interference *J. Neurosci. Methods* **159** 170–80

[27] Thorbergsson P T, Garwicz M, Schouenborg J and Johansson A J 2012 Computationally efficient simulation of extracellular recordings with multielectrode arrays *J. Neurosci. Methods* **211** 133–44

[28] Camuñas-Mesa L A and Quiroga R Q 2013 A detailed and fast model of extracellular recordings *Neural Comput.* **25** 1191–212

[29] Nakatani H *et al* 2001 Detection of nerve action potentials under low signal-to-noise ratio condition *IEEE Trans. Biomed. Eng.* **48** 845–9

[30] Nenadic Z and Burdick J W 2005 Spike detection using the continuous wavelet transform *IEEE Trans. Biomed. Eng.* **52** 74–87

[31] Rutishauser U, Schuman E M and Mamelak A N 2006 Online detection and sorting of extracellularly recorded action potentials in human medial temporal lobe recordings, in vivo *J. Neurosci. Methods* **154** 204–24

[32] Borghi T, Gusmeroli R, Spinelli A and Baranauskas G 2007 A simple method for efficient spike detection in multiunit recordings *J. Neurosci. Methods* **163** 176–80

[33] Deng S, Srinivasan R, Lappas T and D'Zmura M 2010 EEG classification of imagined syllable rhythm using hilbert spectrum methods *J. Neural Eng.* **7** 046006

[34] Fatourechi M, Ward R and Birch G 2008 A self-paced brain–computer interface system with a low false positive rate *J. Neural Eng.* **5** 9

[35] Jolliffe I 2005 *Principal Component Analysis* (New York: Wiley)

[36] Bashashati A, Fatourechi M, Ward R K and Birch G E 2007 A survey of signal processing algorithms in brain–computer interfaces based on electrical brain signals *J. Neural Eng.* **4** R32

[37] Harris K D, Henze D A, Csicsvari J, Hirase H and Buzsáki G 2000 Accuracy of tetrode spike separation as determined by simultaneous intracellular and extracellular measurements *J. Neurophysiol.* **84** 401–14

[38] Quotb A, Bornat Y and Renaud S 2011 Wavelet transform for real-time detection of action potentials in neural signals *Frontiers Neuroeng.* **4** 1–0

[39] Quiroga R Q, Nadasdy Z and Ben-Shaul Y 2004 Unsupervised spike detection and sorting with wavelets and superparamagnetic clustering *Neural Comput.* **16** 1661–87

[40] Letelier J C and Weber P P 2000 Spike sorting based on discrete wavelet transform coefficients *J. Neurosci. Methods* **101** 93–106

[41] Hulata E, Segev R, Shapira Y, Benveniste M and Ben-Jacob E 2000 Detection and sorting of neural spikes using wavelet packets *Phys. Rev. Lett.* **85** 4637–40

[42] Pavlov A, Makarov V A, Makarova I and Panetsos F 2007 Sorting of neural spikes: when wavelet based methods outperform principal component analysis *Nat. Comput.* **6** 269–81

[43] Feng G-C, Yuen P C and Dai D-Q 2000 Human face recognition using PCA on wavelet subband *J. Electron. Imaging* **9** 226–33

[44] Falconer K and Howroyd J 1997 Packing dimensions of projections and dimension profiles *Mathematical Proc. Cambridge Philosophical Society* vol 121 (Cambridge: Cambridge University Press) pp 269–86

[45] Su H and Wenxia L 1996 Packing dimension of generalized moran sets *Prog. Nat. Sci.* **6** 148–52

[46] Talagrand M and Xiao Y 1996 Fractional brownian motion and packing dimension *J. Theor. Probab.* **9** 579–93

[47] Ding M, Grebogi C, Ott E, Sauer T and Yorke J A 1993 Estimating correlation dimension from a chaotic time series: when does plateau onset occur? *Physica* D **69** 404–24

[48] Carvajal R, Wessel N, Vallverdú M, Caminal P and Voss A 2005 Correlation dimension analysis of heart rate variability in patients with dilated cardiomyopathy *Comput. Methods Programs Biomed.* **78** 133–40

[49] Wang W, Wu Z and Chen J 2001 Fault identification in rotating machinery using the correlation dimension and bispectra *Nonlinear Dyn.* **25** 383–93

[50] Camastra F and Vinciarelli A 2002 Estimating the intrinsic dimension of data with a fractal-based method *IEEE Trans. Pattern Anal. Mach. Intell.* **24** 1404–7

[51] Lam L 2003 *Introduction to Nonlinear Physics* (Berlin: Springer)

[52] Li X, Jiang J, Zhu W, Yu C, Sui M, Wang Y and Jiang T 2007 Asymmetry of prefrontal cortical convolution complexity in males with attention-deficit/hyperactivity disorder using fractal information dimension *Brain Dev.* **29** 649–55

[53] Yu L, Zhang D, Wang K and Yang W 2005 Coarse iris classification using box-counting to estimate fractal dimensions *Pattern Recognit.* **38** 1791–8

[54] Salmasi M and Modarres-Hashemi M 2009 Design and analysis of fractal detector for high resolution radars *Chaos Solitons Fractals* **40** 2133–45

[55] Ercolini E, Valle F, Adamcik J, Witz G, Metzler R, De Los Rios P, Roca J and Dietler G 2007 Fractal dimension and localization of DNA knots *Phys. Rev. Lett.* **98** 058102

[56] Bruno O M, de Oliveira Plotze R, Falvo M and de Castro M 2008 Fractal dimension applied to plant identification *Inf. Sci.* **178** 2722–33

[57] Dubuc B, Quiniou J, Roques-Carmes C, Tricot C and Zucker S 1989 Evaluating the fractal dimension of profiles *Phys. Rev.* A **39** 1500

[58] Glidden D V, Shiboski S C and McCulloch C E 2011 *Regression Methods in Biostatistics: Linear, Logistic, Survival, and Repeated Measures Models* (Berlin: Springer)

[59] Gnitecki J and Moussavi Z 2005 The fractality of lung sounds: a comparison of three waveform fractal dimension algorithms *Chaos Solitons Fractals* **26** 1065–72

[60] Henze D, Harris K, Borhegyi Z, Csicsvari J, Mamiya A, Hirase H, Sirota A and Buzsáki G Simultaneous intracellular and extracellular recordings from hippocampus region CA1 of anesthetized rats CRCNS.org DOI: http://dx.doi.org/10.6080/K02Z13FP

[61] Zviagintsev A, Perelman Y and Ginosar R 2006 Algorithms and architectures for low power spike detection and alignment *J. Neural Eng.* **3** 35

[62] Yang C, Olson B and Si J 2011 A multiscale correlation of wavelet coefficients approach to spike detection *Neural Comput.* **23** 215–50

[63] Shahid S and Smith L S 2008 A novel technique for spike detection in extracellular neurophysiological recordings using cepstrum of bispectrum *Proc. European Signal Processing Conf.*

[64] Grassberger P 1993 On efficient box counting algorithms *Int. J. Mod. Phys.* C **4** 515–23

[65] Hou X-J, Gilmore R, Mindlin G B and Solari H G 1990 An efficient algorithm for fast $O(N^{*}\ln(N))$ box counting *Phys. Lett.* A **151** 43–6

Chapter 5

Discussion

We studied information efficacy of a synapse during short-term depression. We used a binary asymmetric channel to model the synapse and captured the two synaptic release mechanisms, namely spike-evoked release and spontaneous release. We introduced a two-state model of short-term depression and derived the mutual information rate of the depressing synapse analytically. In addition to the information rate, a new measure was proposed to investigate the trade-off between energy consumption and the rate of information transmission in the synapse. The new measure, called energy-normalized information rate, was calculated by normalizing the information rate of the synapse by the energy cost of synaptic release. The simplicity of the two-state model of depression allowed us to determine the regimes of synaptic parameters in which short-term depression enhances or degrades synaptic information efficacy.

In the two-state model of depression, the state-space is reduced to two states, and the gradual depression and exponential recovery of the synapse are not included in the analysis. We extended the model of the synapse to a binary asymmetric channel with a memory of release outcomes. It was demonstrated that for a large enough memory, the model precisely follows the dynamics of short-term depression. We proved that the mutual information rate of the synapse under short-term depression is equal to the statistical average over the mutual information rates of all the possible states of the synapse. In other word, the mutual information rate is a linear function of the mutual information rates of the consistent states of the release site.

We demonstrated that the functional role of short-term depression depends on the characteristics and dynamics of the synapse. If spontaneous release and spike-evoked release are depressed equally, then short-term depression reduces both the mutual information and energy-normalized information rate of the synapse. However, if spontaneous release is depressed more than spike-evoked release, then depression can

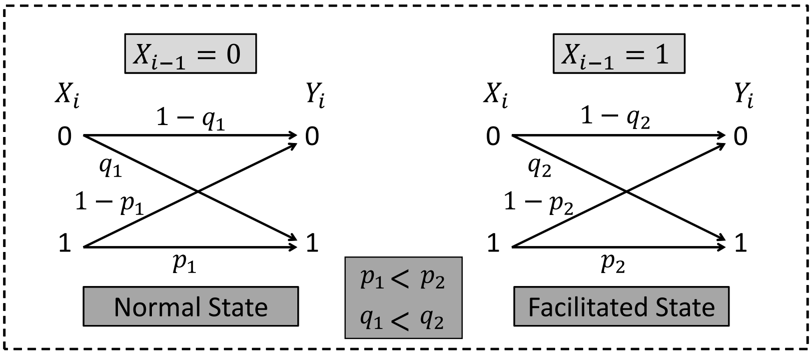

Figure 5.1: The two-state model of facilitation. The state of the release site at time i is determined by the previous input spike event, X_{i-1}. If there was a spike in the previous time interval, then the release site goes to the facilitated state in which the release probabilities are higher.

enhance synaptic information efficacy. Our information-theoretic analysis, revealed three functional classes for depressing synapses.

5.1 Linearity of mutual information rate

The linearity of the mutual information rate of the synapse is an intrinsic property of short-term depression and does not hold necessarily for other forms of plasticity. Here, we show that in the case of short-term facilitation, the mutual information rate of the synapse is no longer a linear function.

We consider a simple model of facilitation in which the synapse is modeled by two states, the normal state and the facilitated state. The arrival of an action potential at the presynaptic neuron increases the concentration of the intracellular calcium and takes the synapse to the facilitated state with higher release probabilities. In the absence of an action potential, the synapse returns to the normal state (Fig. 5.1). Although this model looks simpler than the two-state model of depression, we will show in the following that the mutual information rate of the two-state model of facilitation is still an open problem.

Let $X = \{X_i\}_{i=1}^{\infty}$ be a first-order binary Markov process (Fig. 5.2A). If X_i is the input of a binary symmetric channel, then the output of the channel, Y_i, generates a random process, $Y = \{Y_i\}_{i=1}^{\infty}$, which is called a hidden Markov process (Fig. 5.2B). Although the hidden Markov process, Y, has a simple definition, its entropy rate is still an open problem in information theory (Jacquet et al., 2008; Han and Marcus, 2006; Zuk et al., 2005).

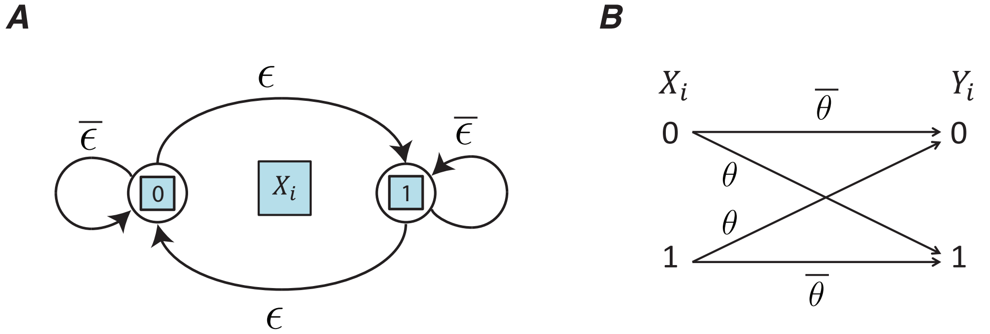

Figure 5.2: Hidden Markov process. (A) A binary Markov process, $X = \{X_i\}_{i=1}^{\infty}$. (B) A binary channel with the input X. The output of the channel, Y, is a hidden Markov process

We now show that the two-state model of facilitation is equivalent to a hidden Markov model. Let X_{i-1}, X_i be the state of the model at time i. Since the presynaptic input spike process X is an i.i.d. process with $P(X_i = 1) = \alpha$, the state transitions of the two-state model of facilitation can be modeled by a 4-state Markov chain (Fig. 5.3A). Moreover, the release outcome, Y_i, in the two-state model of facilitation is identical to the output of the asymmetric channel in Fig. 5.3B. Therefore, Y_i is also a hidden Markov process (and even more complex than the process in Fig. 5.2). This equivalency implies that the entropy rate of the release outcome and the mutual information rate of the two-state model of facilitation are still open problems.

Although the mutual information rate of the two-state model of facilitation is an open problem, we derived some lower bounds and upper bounds for the information rate of the synapse under short-term facilitation. We proved that the statistical average over the mutual information rates of the normal state and the facilitated state is just a lower bound for the mutual information rate of facilitation. Our preliminary results were presented in FENS 2016:

- M. Salmasi, A. Loebel, S. Glasauer, M. Stemmler, "Short-Term Facilitation Improves the Information Rate of a Two-State Synapse", 10th FENS Forum of Neuroscience, Copenhagen, July 2016.

5.2 Towards synaptic information efficacy

Information efficacy of a synapse is the mutual information rate between the input spike process and the postsynaptic potential. Numerical and analytical methods have been used to calculate the mutual information rate of the synapse.

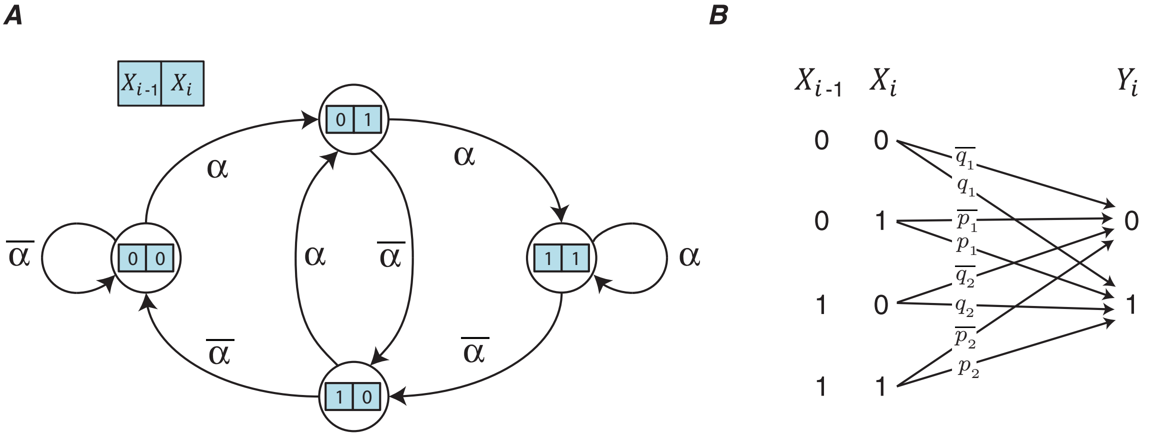

Figure 5.3: The equivalent hidden Markov model for the two-state model of facilitation. (A) A 4-state Markov chain as a model for the state transitions in short-term facilitation. (B) The release outcome, modeled as the output of a communication channel.

In numerical methods, the spike train of the presynaptic neuron and the activity of the postsynaptic neuron are converted to binary sequences. The entropy estimation algorithms are then used to calculate synaptic information efficacy. The main advantage of numerical methods is that more realistic models of synaptic transmission can be studied (London et al., 2002; Neymotin et al., 2011; Arleo et al., 2010; London et al., 2008). Nevertheless, numerical methods are subject to estimation bias or error, and require new sampling or simulation for every change of model parameters. Statistical bias in entropy and information estimation has spawned an entire literature in the field on bias correction (Paninski, 2003). To avoid these limitations, analytical methods have been suggested for studying synaptic information efficacy (Fuhrmann et al., 2002; Goldman, 2004).

In (Fuhrmann et al., 2002), the mutual information is calculated between the 'current' postsynaptic potential and the presynaptic input spike train. The information of the past postsynaptic potentials are neglected to make the calculations mathematically tractable. The transmission and noise entropies are calculated by numerical estimation of probability distribution functions, and an upper bound is presented for the mutual information between the postsynaptic potential and input spike train. In contrast to this paper, we calculated the mutual information rate between 'all' the release events and the presynaptic spike train. Our analytical approach did not require any numerical estimation of probability distributions and the bias error was avoided entirely.

The analysis in (Goldman, 2004) is done through modeling the presynaptic spike train and vesicular release outcome by two point processes. The mutual information 'per vesicle release' is calculated between the occurrence times of the input spikes and the vesicle releases. The input spike train is modeled by renewal processes which is more general than Poisson processes and captures the correlation between the successive spikes of the presynaptic neuron. To simplify the calculations, it is assumed that the synapse either transmits with probability one (provided that a vesicle is ready to release), or does not release at all until a vesicle is recovered. The probability distribution of the output process is derived using the inverse of the Laplace transform and the entropy functions are estimated by numerical simulations. In contrast to (Goldman, 2004), the release of a vesicle is probabilistic in our model and the release probability is regulated by the release history profile of the synapse. Moreover, our model includes the spontaneous release of the synapse which is shown to be a critical mechanism in determining synaptic information efficacy. By modeling the release site with a binary asymmetric channel with memory, we achieved a suitable framework to derive a closed form expression for the mutual information rate of the release site. Also, we calculated the mutual information rate 'per unit time' which does not have the limitations of the information rate per vesicle release in low release probabilities (Goldman, 2004).

5.3 Information efficacy and energy consumption

The human brain comprises 2% of the body's weight. However, it consumes 20% of the oxygen that is used by the whole body (Attwell and Laughlin, 2001). The energy cost of synaptic transmission is estimated to be around 41% of the total metabolism of the cortex, indicating that synaptic transmission is the highest energy-demanding mechanism of the brain (Harris et al., 2012).

The high energy cost of synaptic transmission forces the brain to compromise between the rate of information transmission and its energy consumption. In our study, we assumed that the synapse consumes one unit of energy for each release and calculated the energy-normalized information rate of the synapse. We assessed the effect of short-term depression on the energy-efficient information transmission through the synapse. The other energy expenses of the neuron were not included in our analysis. The reason was that in our study, we were interested in the energy-rate trade-off of a single synapse. Therefore, the energy cost of the presynaptic action potentials, which trigger the synaptic release in *all* of the synapses of the neuron, were not included in our calculations. In the future studies, we will extend the information rate analysis from one synapse to multiple synapses. The energy cost of the action potential is then added to the total energy expenditure of the synapses, and the notion of energy-normalized information rate is updated.

5.4 Spontaneous release

An ideal synapse, releases a vesicle in response to a presynaptic action potential and stops releasing in the inter-spike intervals. Real synapses, however, deviate from the ideal synapse in two ways. Firstly, the spike-evoked release probability of a real synapse is usually smaller than one, which means that the synapse does not respond to every action potential, and secondly, the synapse may release a vesicle spontaneously even in the absence of an action potential.

Spontaneous release contributes to the acute regulation of synaptic homeostasis (Jakawich et al., 2010). There are several hypothesis about the mechanisms underlying spontaneous release (Kavalali, 2015). One suggested mechanism for spontaneous release is the subthreshold elevations of presynaptic calcium concentration which causes fluctuations in the release machinery and leads to a vesicle release. Some studies have suggested a divergent release machinery, e.g. different SNARE proteins, for spontaneous release and spike-evoked release. There are also some evidence for an isolated pool of vesicles for spontaneous release (Sara et al., 2005; Fredj and Burrone, 2009). The segregation of transmission mechanisms has been also observed on the postsynaptic site. It has been shown that distinct sets of AMPA and NMDA receptors are activated in response to the spike-evoked and spontaneous release (Atasoy et al., 2008; Sara et al., 2011). Another hypothetical mechanism is the spatial segregation of synaptic release sites. It has been proposed that there are specialized release sites, or even distinct synapses for spike-evoked and spontaneous release (Kavalali, 2015).

These findings support the idea that distinct mechanisms govern spontaneous and spike-evoked release. To implement this segregation of mechanisms in our model, we assigned separate depression coefficients and recovery time constants to spike-evoked and spontaneous release.

5.5 Interpretation of mutual information

Mutual information is widely used to calculate the amount of information that a signal contains about another signal. Although mutual information is a powerful tool in signal processing, its values should be interpreted cautiously. Here we describe the

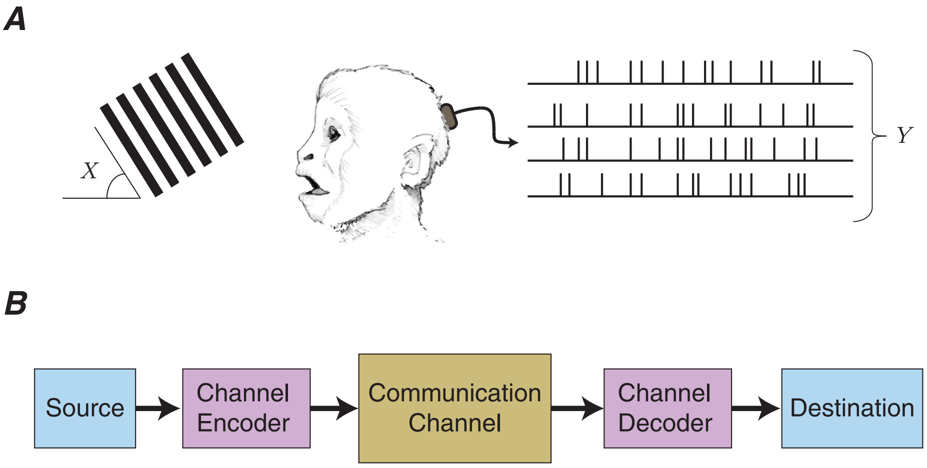

Figure 5.4: (A) A monkey views gratings with different orientations, while the spiking activity of N neurons in V1 is recorded. The image of the monkey's head is from https://backyardbrains.com. (B) The optimal scheme for information transmission in communication systems. A source is connected to a destination node through a communication channel. The channel's capacity C is defined as the maximum of the mutual information between the input and output of the communication channel. In channel coding theorem, Shannon proves that for every information rate R, $R < C$, there exists an optimal channel encoder and an optimal channel decoder for which the source can send the information to the destination with an arbitrary low probability of error.

strengths and limitations of information-theoretic analysis through a hypothetical experiment.

Assume that gratings with different orientations are presented to a monkey and a population of V1 neurons are recorded (Fig. 5.4A). The orientation of the grating is represented by the random variable X. The vector $Y = (Y^{(1)}, Y^{(2)}, ..., Y^{(N)})$ denotes the random processes corresponding to the activity of a population of N neurons in V1 during the task.

The mutual information between X and Y, $I(X;Y)$, gives the amount of information that can be extracted from the population of neurons, Y, about the orientation of the grating, X. For example, if $I(X;Y) = 7$, then we infer that the population of neurons carries 7 bits of information about X. In other words, given the recording of the population (and with the uniformity assumption), we can estimate the orientation of the input by a precision of $\frac{180}{2^7} = 1.4$ degrees. However, the monkey's performance in determining the orientation of the grating may be much lower than the precision that is estimated from the mutual information, $I(X;Y)$.

The mutual information is a measure of the amount of information that can be potentially extracted from the signal, provided that optimal encoding and decoding schemes are used (Fig. 5.4B). However, the encoding and decoding of information is suboptimal in the brain, due to the limited resources of the brain, the restricted connectivity between the neurons, and the constraints on the range of synaptic computations. Therefore, the mutual information, $I(X;Y)$, should be considered as an upper bound for the 'accessible' information.

5.6 Input spike correlations

The Poisson process is a common model for spiking activity of the neurons. The inter-spike intervals in a Poisson process are independent random variables with exponential distribution. The Poisson spike trains have the memoryless property, that is, the probability of having a spike in the next t milliseconds is independent of the occurrence time of the previous spike.

Poisson processes do not capture some basic properties of neuronal spike trains, such as refractory period. Following an action potential, the neuron goes to a state of unresponsiveness, known as the refractory period, and does not elicit another action potential for 3-4 ms. The memoryless property of the Poisson process does not allow the spike timing of the next spike to depend on the timing of the previous spike (Rieke, 1999). Renewal processes are an extension of Poisson processes that are used for modeling refractoriness and some other characteristics of spike trains (Johnson, 1996). The inter-spike intervals of a renewal process are independent, but the distribution of the intervals is not necessarily exponential. In renewal processes, the refractory period can be modeled by choosing a proper distribution for the inter-spike intervals.

Spike frequency adaptation has been reported in several types of neurons (Ratnam and Nelson, 2000; Chacron et al., 2000). The spiking activity of a neuron with spike frequency adaptation depends not only on the timing of the previous spike but also on the ones before that (Johnson, 1996). The statistical analysis of these neurons reveals a negative correlation of inter-spike intervals (Ratnam and Nelson, 2000; Chacron et al., 2000). Markov point processes and autoregressive processes have been proposed for modeling the correlations of inter-spike intervals (Farkhooi et al., 2009)

In our future studies, we will extend the model of presynaptic spike train to correlated processes and investigate how short-term depression modulates the information efficacy of a synapse stimulated by a correlated spike train.

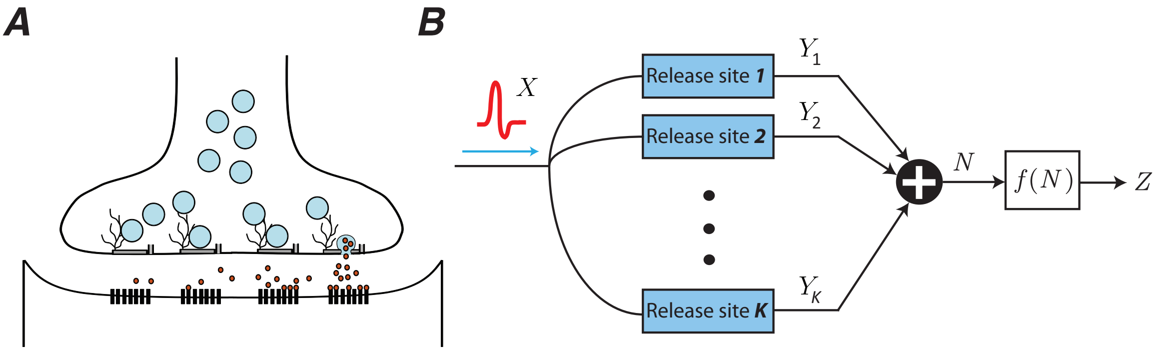

Figure 5.5: (A) A synapse with multiple release site. The neurotransmitter content of a released vesicle may spill over into the receptors of neighboring sites. (B) A model for a synapse with multiple release sites.

5.7 Multiple release sites

The number of release sites in a synapse varies from one to hundreds (Fig. 5.5A) (Clarke et al., 2012). We present a model to study the information efficacy of a synapse with multiple release sites. The input spike process, X, triggers vesicular release in K independent release sites of the synapse (Fig. 5.5B). Each release site is modeled as a binary asymmetric channel with memory. The content of the memory is the previous release outcomes of the release site and determines the channel's release probabilities based on the dynamics of short-term depression.

The exact relationship between the number of released vesicles and the amplitude of the postsynaptic potential has not been established yet (function f in Fig. 5.5B). We will study three potential realizations of this function:

1- The contents of a single vesicle is enough to saturate all the receptors on the postsynaptic site (Fig. 5.6A). It is assumed that the number of neurotransmitter molecules inside a vesicle is much larger than the total number of receptors on the postsynaptic site. In addition, the diffusion coefficient of the neurotransmitter and the distance between the active zones should permit the molecules to spill over and activate all the receptors.

2- The postsynaptic potential is a linear function of the number of released vesicles (Fig. 5.6B). The underlying assumption for this linearity is that the released vesicle from an active zone can only activate the postsynaptic receptors that locate opposite to the active zone, and there is no spill-over of the neurotransmitter.

3- The postsynaptic potential first increases linearly as a function of the number of released vesicles and then saturates (Fig. 5.6C). By proper choice of the linearity threshold N_T and the saturation time constant, this function is likely to describe the

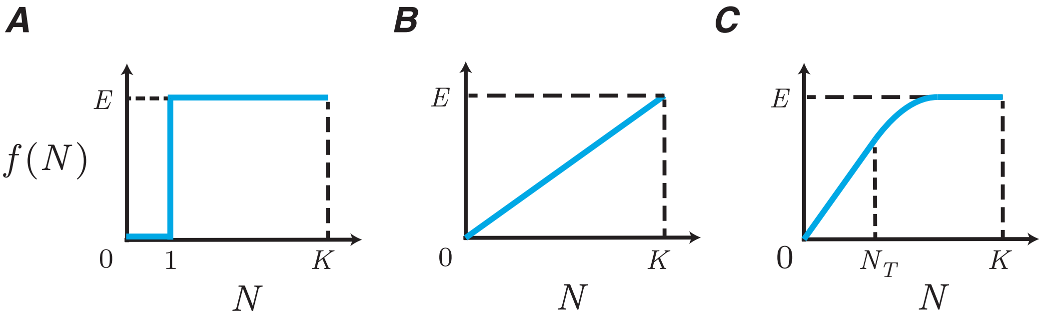

Figure 5.6: The relationship between the postsynaptic potential and the number of released vesicles from multiple release sites of a single synapse. (A) One single vesicle activates all the receptors. (B) A released vesicle activates only the local postsynaptic receptors that are opposite to its release site. (C) The contribution of vesicles to the postsynaptic potential is linear if the number of released vesicles is less than a threshold, N_T; the postsynaptic potential converges exponentially if more vesicles are released.

relationship between the postsynaptic potential and the number of released vesicles in most of the synapses.

The information-theoretic analysis of this model will help us to understand how the number of release sites affects the information efficacy of the synapse. Moreover, by studying different saturation models, we can evaluate the impact of neurotransmitter spill-over and diffusion coefficient on the rate of information transmission.

5.8 Information rate between two neurons

A neuron transfers information to the other neurons through thousands of synapses. A natural progression of this thesis is to analyze the information rate between two neurons. We can use our model of a single release site to build a model for the information transmission between neurons. We assume that the two neurons are connected through L synapses. The number of release sites of the synapse i, $1 \leq i \leq L$, is denoted by K_i. Each release site is modeled by a binary asymmetric channel with memory. The postsynaptic potential corresponding to the synapse i is determined by the function $f_i(N_i)$, where N_i is the number of released vesicles from the K_i release sites of the synapse (Fig. 5.7). If the summation of postsynaptic potentials of the L synapses is larger than a threshold T, then an action potential is elicited in the postsynaptic neuron.

The information efficacy of the synaptic connections between the two neurons is defined by the mutual information between the spiking activity of the presynaptic

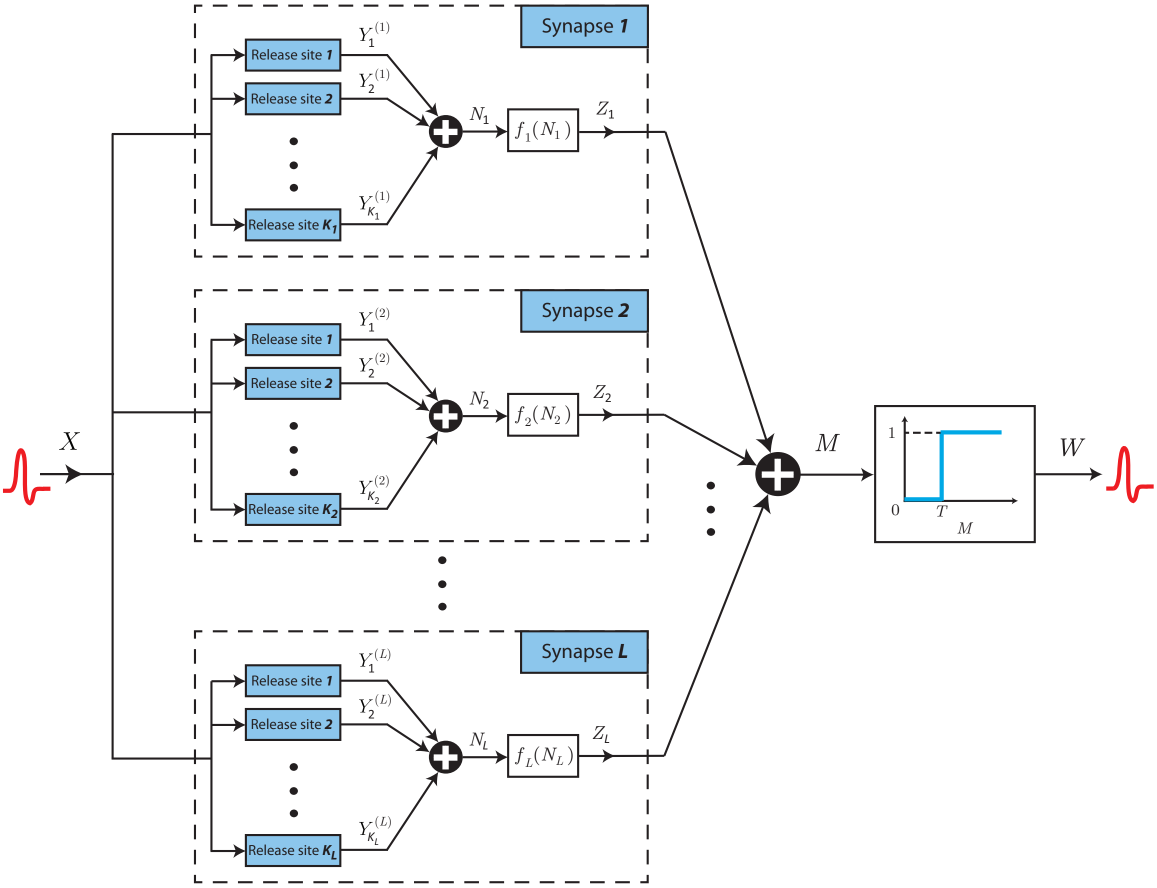

Figure 5.7: A model for information transmission between two neurons. The neurons are connected through L synapses. The synapse i has K_i release sites. Each release site is modeled by a binary asymmetric channel with memory.

neuron, X, and the generated train of action potentials in the postsynaptic neuron, W.

In our future research, we calculate the mutual information rate between the two neurons, $I(X;W)$, during short-term depression. We can then investigate how the number of synapses, the number of release sites in each synapse, and the dynamics of short-term depression affect information transmission between the two neuron.

5.9 Complexity of synaptic transmission

The model presented in this thesis is a phenomenological model that captures the basic properties of synaptic transmission and short-term depression. The release machinery of the synapse and the underlying mechanisms of short-term depression are, however, much more complicated. Here, we describe some of the features of synaptic transmission than can change the information efficacy of a synapse and should be included in future models.

5.9.1 Presynaptic terminal

The concentration of calcium plays an important role in the release machinery of the synapse. The dynamics of the calcium channels and the random fluctuations of calcium density in the presynaptic terminal governs the release probability and plasticity of the synapse (Zucker and Regehr, 2002).

The size of the vesicles varies from neuron to neuron (Hu et al., 2008). Also, the concentration of the neurotransmitter that is stored inside a vesicle depends on the type and dynamics of the neuron (Gasnier, 2000). These two key parameters determine the efficiency of a vesicle in activating postsynaptic receptors.

In presynaptic terminals, vesicles are clustered in three distinct pools (Rizzoli and Betz, 2005):

1- Readily releasable pool: The vesicles of this pool are docked to the active zones and are immediately available for release. This pool contains only 1% of the synaptic vesicles.

2- Recycle pool: The vesicles of the recycle pool are released withing a few seconds in response to a constant stimulation. The pool contains 10-20% of the vesicles and refills the readily releasable pool.

3- Reserve pool: Most of the vesicles of the synapse (80-90%) are located in this pool. It takes tens of seconds or minutes for the vesicles of this pool to migrate to the active zones and be released.

The number of vesicles in each pool and the rate of depletion and refill of the pools shapes the dynamics of synaptic plasticity.

The vesicles are released from some specialized parts of the membrane, known as active zones. The size and the shape of the active zones vary among synapses and alter the release properties of the synapse (Holderith et al., 2012; Zhai and Bellen, 2004).

In our model, we assumed that the active zone follows *one site-one vesicle hypothesis* (Auger and Marty, 2000). This means that the active zone can release at most one vesicle in response to an incoming action potential. Some studies have reported multivesicular release from a single active zone (Wadiche and Jahr, 2001). The multivesicular release changes synaptic information efficacy by increasing the reliability of the synapse.

5.9.2 Synaptic cleft

After the release of a vesicle, the neurotransmitter molecules diffuse in the synaptic cleft. The spatial distribution of the neurotransmitter molecules is determined by the location of the release, the width and morphology of the synaptic cleft, and the diffusion characteristics of the neurotransmitter. Some studies show that the molecules released from one release site can spill over to the other active zones of the synapse, or even further to the neighboring synapses (DiGregorio et al., 2002; Telgkamp et al., 2004). The distribution of the molecules and the amount of the spill-over changes the activation pattern of the receptors.

The synaptic cleft is cleaned from neurotransmitter molecules by reuptake mechanisms. The neuronal or glial transporters absorb the neurotransmitter molecules and terminate synaptic transmission. The distribution and location of transporters changes the concentration dynamics of the neurotransmitter and alters the postsynaptic potential (Danbolt, 2001).

5.9.3 Postsynaptic site

The type and the density of the receptors vary from one synapse to another (Auger and Marty, 2000). For example, in hippocampal synapses, the ratio of AMPA to NMDA receptors changes with the size of the postsynaptic density (Takumi et al., 1999). The shape of the postsynaptic potential is determined by the number of activated receptors of each type.

The postsynaptic potential may reduce by desensitization of the receptors. In desensitization, the ligand-gated channels are inactivated after being exposed to the neurotransmitter molecules. The receptors enter a non-responsive state and are not activated for tens of milliseconds to minutes (Zucker and Regehr, 2002). The recovery time constant of desensitization and the dynamics of the receptors affect the temporal profile of the postsynaptic current and significantly changes synaptic information efficacy.

The measurements show that the number of neurotransmitter molecules inside a vesicle is much larger than the number of receptors on the postsynaptic density. Based on this observation, it has been hypothesized that the release of a single vesicle can saturate all the receptors. Although several studies support receptor saturation (Clements et al., 1992; Tang et al., 1994; Tong and Jahr, 1994), there are increasing evidences for synapses in which the receptors are not saturated by a single vesicular release (Frerking and Wilson, 1996; McAllister and Stevens, 2000; Ishikawa et al., 2002). Computational models are used to study the proportion of activated receptors after the release of a single vesicle. The synaptic cleft, spatial distribution of the receptors, and the diffusion of the neurotransmitter molecules are modeled and the probability of receptor occupancy is studied for different concentrations of the neurotransmitter (Franks et al., 2002; Holmes, 1995; Tarusawa et al., 2009; Ventriglia and Di Maio, 2013). The incorporation of diffusion models of neurotransmitter into the synaptic model will help us to understand the effect of receptor saturation and neurotransmitter spill-over on the information efficacy of the synapse.

5.10 Conclusion

Short-term depression is a ubiquitous phenomenon in synapses. The functional role of short-term depression in filtering and decorrelation of the input has been established in several studies. It has been also hypothesized that short-term depression modulates the rate of information transmission at the synapse. To study this hypothesis, we modeled a synapse by a binary asymmetric channel with memory and calculated the information rate of the synapse analytically. Our analysis demonstrated how depression of spike-evoked release and spontaneous release alters the mutual information rate and energy-rate trade-off of the synapse.

Synaptic transmission is mediated through several presynaptic and postsynaptic mechanisms. Our model captures the basics of the synaptic release, but also relies on some simplifying assumptions that keep the model mathematically tractable. To have a more accurate estimation of synaptic information efficacy, the computational models of the synapse should include the other important aspects of the release mechanism, such as the size of the pools of vesicles, the depletion and refill rate of the pools, the concentration of vesicles, the diffusion characteristics of neurotransmitter, the saturation and desensitization properties of the receptors, and several other aspects of the release machinery.

Modeling a depressing synapse with a communication channel provides a natural framework for information-theoretic analysis of synaptic transmission. Our model can be used as a building block to construct more advanced models of information transmission between the neurons. The extension of this work will permit the evaluation of the rate of information transmission in an energy-constrained network of neurons.

Bibliography

Abbott, L. F. and Regehr, W. G. Synaptic computation. *Nature*, 431(7010):796–803, 2004.

Abolafia, J. M., Vergara, R., Arnold, M., Reig, R., and Sanchez-Vives, M. Cortical auditory adaptation in the awake rat and the role of potassium currents. *Cerebral Cortex*, 21(5):977–990, 2010.

Arleo, A., Nieus, T., Bezzi, M., D'Errico, A., D'Angelo, E., and Coenen, O. J.-M. How synaptic release probability shapes neuronal transmission: information-theoretic analysis in a cerebellar granule cell. *Neural Computation*, 22(8):2031–2058, 2010.

Atasoy, D., Ertunc, M., Moulder, K. L., Blackwell, J., Chung, C., Su, J., and Kavalali, E. T. Spontaneous and evoked glutamate release activates two populations of nmda receptors with limited overlap. *Journal of Neuroscience*, 28(40):10151–10166, 2008.

Attwell, D. and Laughlin, S. B. An energy budget for signaling in the grey matter of the brain. *Journal of Cerebral Blood Flow & Metabolism*, 21(10):1133–1145, 2001.

Auger, C. and Marty, A. Quantal currents at single-site central synapses. *The Journal of Physiology*, 526(1):3–11, 2000.

Baddeley, R., Abbott, L. F., Booth, M. C., Sengpiel, F., Freeman, T., Wakeman, E. A., and Rolls, E. T. Responses of neurons in primary and inferior temporal visual cortices to natural scenes. *Proceedings of the Royal Society of London B: Biological Sciences*, 264(1389):1775–1783, 1997.

Borst, A. and Theunissen, F. E. Information theory and neural coding. *Nature Neuroscience*, 2(11):947–957, 1999.

Brochini, L., Carelli, P. V., and Pinto, R. D. Single synapse information coding in intraburst spike patterns of central pattern generator motor neurons. *Journal of Neuroscience*, 31(34):12297–12306, 2011.

Brody, D. L. and Yue, D. T. Release-independent short-term synaptic depression in cultured hippocampal neurons. *Journal of Neuroscience*, 20(7):2480–2494, 2000.

Brostek, L., Eggert, T., Ono, S., Mustari, M. J., Büttner, U., and Glasauer, S. An information-theoretic approach for evaluating probabilistic tuning functions of single neurons. *Frontiers in Computational Neuroscience*, 5, 2011.

Brunel, N. and Nadal, J.-P. Mutual information, fisher information, and population coding. *Neural Computation*, 10(7):1731–1757, 1998.

Chacron, M. J., Longtin, A., St-Hilaire, M., and Maler, L. Suprathreshold stochastic firing dynamics with memory in p-type electroreceptors. *Physical Review Letters*, 85(7):1576, 2000.

Chance, F. S., Nelson, S. B., and Abbott, L. F. Synaptic depression and the temporal response characteristics of v1 cells. *Journal of Neuroscience*, 18(12):4785–4799, 1998.

Chung, S., Li, X., and Nelson, S. B. Short-term depression at thalamocortical synapses contributes to rapid adaptation of cortical sensory responses in vivo. *Neuron*, 34(3):437–446, 2002.

Clarke, G. L., Chen, J., and Nishimune, H. Presynaptic active zone density during development and synaptic plasticity. *Frontiers in Molecular Neuroscience*, 5, 2012.

Clements, J. D., Lester, R. A., Tong, G., Jahr, C. E., and Westbrook, G. L. The time course of glutamate in the synaptic cleft. *SCIENCE-NEW YORK THEN WASHINGTON-*, 258:1498–1498, 1992.

Clifford, C. W., Webster, M. A., Stanley, G. B., Stocker, A. A., Kohn, A., Sharpee, T. O., and Schwartz, O. Visual adaptation: Neural, psychological and computational aspects. *Vision research*, 47(25):3125–3131, 2007.

Cover, T. M. and Thomas, J. A. *Elements of information theory*. John Wiley & Sons, 2012.

Dan, Y., Atick, J. J., and Reid, R. C. Efficient coding of natural scenes in the lateral geniculate nucleus: experimental test of a computational theory. *Journal of Neuroscience*, 16(10):3351–3362, 1996.

Danbolt, N. C. Glutamate uptake. *Progress in Neurobiology*, 65(1):1–105, 2001.

DiGregorio, D. A., Nusser, Z., and Silver, R. A. Spillover of glutamate onto synaptic ampa receptors enhances fast transmission at a cerebellar synapse. *Neuron*, 35(3): 521–533, 2002.

Dimitrov, A. G., Lazar, A. A., and Victor, J. D. Information theory in neuroscience. *Journal of computational neuroscience*, 30(1):1–5, 2011.

Farkhooi, F., Strube-Bloss, M. F., and Nawrot, M. P. Serial correlation in neural spike trains: experimental evidence, stochastic modeling, and single neuron variability. *Physical Review E*, 79(2):021905, 2009.

Fioravante, D. and Regehr, W. G. Short-term forms of presynaptic plasticity. *Current Opinion in Neurobiology*, 21(2):269–274, 2011.

Fortune, E. S. and Rose, G. J. Short-term synaptic plasticity as a temporal filter. *Trends in neurosciences*, 24(7):381–385, 2001.

Franks, K. M., Bartol, T. M., and Sejnowski, T. J. A monte carlo model reveals independent signaling at central glutamatergic synapses. *Biophysical Journal*, 83 (5):2333–2348, 2002.

Fredj, N. B. and Burrone, J. A resting pool of vesicles is responsible for spontaneous vesicle fusion at the synapse. *Nature Neuroscience*, 12(6):751–758, 2009.

Frerking, M. and Wilson, M. Saturation of postsynaptic receptors at central synapses? *Current Opinion in Neurobiology*, 6(3):395–403, 1996.

Fuhrmann, G., Segev, I., Markram, H., and Tsodyks, M. Coding of temporal information by activity-dependent synapses. *Journal of Neurophysiology*, 87(1):140–148, 2002.

Gallager, R. G. *Information theory and reliable communication*, volume 2. Springer, 1968.

Gasnier, B. The loading of neurotransmitters into synaptic vesicles. *Biochimie*, 82 (4):327–337, 2000.

Goldman, M. S. Enhancement of information transmission efficiency by synaptic failures. *Neural Computation*, 16(6):1137–1162, 2004.

Goldman, M. S., Maldonado, P., and Abbott, L. F. Redundancy reduction and sustained firing with stochastic depressing synapses. *The Journal of neuroscience*, 22(2):584–591, 2002.

Gourévitch, B. and Eggermont, J. J. Evaluating information transfer between auditory cortical neurons. *Journal of Neurophysiology*, 97(3):2533–2543, 2007.

Han, G. and Marcus, B. Analyticity of entropy rate of hidden markov chains. *IEEE Transactions on Information Theory*, 52(12):5251–5266, 2006.

Harris, J. J., Jolivet, R., and Attwell, D. Synaptic energy use and supply. *Neuron*, 75(5):762–777, 2012.

Holderith, N., Lorincz, A., Katona, G., Rózsa, B., Kulik, A., Watanabe, M., and Nusser, Z. Release probability of hippocampal glutamatergic terminals scales with the size of the active zone. *Nature Neuroscience*, 15(7):988–997, 2012.

Holmes, W. R. Modeling the effect of glutamate diffusion and uptake on nmda and non-nmda receptor saturation. *Biophysical Journal*, 69(5):1734–1747, 1995.

Hosoi, N., Holt, M., and Sakaba, T. Calcium dependence of exo-and endocytotic coupling at a glutamatergic synapse. *Neuron*, 63(2):216–229, 2009.

Hu, Y., Qu, L., and Schikorski, T. Mean synaptic vesicle size varies among individual excitatory hippocampal synapses. *Synapse*, 62(12):953–957, 2008.

Ishikawa, T., Sahara, Y., and Takahashi, T. A single packet of transmitter does not saturate postsynaptic glutamate receptors. *Neuron*, 34(4):613–621, 2002.

Izhikevich, E. M., Desai, N. S., Walcott, E. C., and Hoppensteadt, F. C. Bursts as a unit of neural information: selective communication via resonance. *Trends in Neurosciences*, 26(3):161–167, 2003.

Jacquet, P., Seroussi, G., and Szpankowski, W. On the entropy of a hidden markov process. *Theoretical Computer Science*, 395(2-3):362–371, 2008. ISSN 0304-3975.

Jakawich, S. K., Nasser, H. B., Strong, M. J., McCartney, A. J., Perez, A. S., Rakesh, N., Carruthers, C. J., and Sutton, M. A. Local presynaptic activity gates homeostatic changes in presynaptic function driven by dendritic bdnf synthesis. *Neuron*, 68(6):1143–1158, 2010.

Johnson, D. H. Point process models of single-neuron discharges. *Journal of computational neuroscience*, 3(4):275–299, 1996.

Kandel, E. R., Schwartz, J. H., Jessell, T. M., et al. *Principles of neural science*, volume 4. McGraw-hill New York, 2000.

Kavalali, E. T. The mechanisms and functions of spontaneous neurotransmitter release. *Nature Reviews Neuroscience*, 16(1):5–16, 2015.

Kohn, A. Visual adaptation: physiology, mechanisms, and functional benefits. *Journal of Neurophysiology*, 97(5):3155–3164, 2007.

Levy, W. B. and Baxter, R. A. Energy-efficient neuronal computation via quantal synaptic failures. *The Journal of Neuroscience*, 22(11):4746–4755, 2002.

Lindner, B., Gangloff, D., Longtin, A., and Lewis, J. E. Broadband coding with dynamic synapses. *Journal of Neuroscience*, 29(7):2076–2087, 2009.

Lodish, H., Berk, A., Zipursky, S. L., Matsudaira, P., Baltimore, D., Darnell, J., et al. *Molecular cell biology*, volume 3. Scientific American Books New York, 1995.

London, M., Schreibman, A., Häusser, M., Larkum, M. E., and Segev, I. The information efficacy of a synapse. *Nature Neuroscience*, 5(4):332–340, 2002.

London, M., Larkum, M. E., and Häusser, M. Predicting the synaptic information efficacy in cortical layer 5 pyramidal neurons using a minimal integrate-and-fire model. *Biological Cybernetics*, 99(4-5):393–401, 2008.

McAllister, A. K. and Stevens, C. F. Nonsaturation of ampa and nmda receptors at hippocampal synapses. *Proceedings of the National Academy of Sciences*, 97(11): 6173–6178, 2000.

Merkel, M. and Lindner, B. Synaptic filtering of rate-coded information. *Physical Review E*, 81(4):041921, 2010.

Müller, J. R., Metha, A. B., Krauskopf, J., and Lennie, P. Rapid adaptation in visual cortex to the structure of images. *Science*, 285(5432):1405–1408, 1999.

Neher, E. and Sakaba, T. Multiple roles of calcium ions in the regulation of neurotransmitter release. *Neuron*, 59(6):861–872, 2008.

Neymotin, S. A., Jacobs, K. M., Fenton, A. A., and Lytton, W. W. Synaptic information transfer in computer models of neocortical columns. *Journal of Computational Neuroscience*, 30(1):69–84, 2011.

Nirenberg, S., Carcieri, S., Jacobs, A., and Latham, P. E. Retinal ganglion cells act largely as independent encoders. *Nature*, 411(6838):698–701, 2001.

Paninski, L. Estimation of entropy and mutual information. *Neural Computation*, 15 (6):1191–1253, 2003.

Purves, D., Augustine, G., Fitzpatrick, D., Hall, W., Lamantia, A.-S., and White, L. *Neuroscience*. Oxford University Press, 2012. ISBN 9780878936953.

Quiroga, R. Q. and Panzeri, S. Extracting information from neuronal populations: information theory and decoding approaches. *Nature Reviews Neuroscience*, 10(3): 173–185, 2009.

Ratnam, R. and Nelson, M. E. Nonrenewal statistics of electrosensory afferent spike trains: implications for the detection of weak sensory signals. *Journal of Neuroscience*, 20(17):6672–6683, 2000.

Reich, D. S., Mechler, F., and Victor, J. D. Independent and redundant information in nearby cortical neurons. *Science*, 294(5551):2566–2568, 2001.

Rieke, F. *Spikes: exploring the neural code*. MIT press, 1999.

Rizo, J. and Rosenmund, C. Synaptic vesicle fusion. *Nature Structural & Molecular Biology*, 15(7):665–674, 2008.

Rizzoli, S. O. and Betz, W. J. Synaptic vesicle pools. *Nature Reviews Neuroscience*, 6(1):57, 2005.

Rosenbaum, R., Rubin, J., and Doiron, B. Short term synaptic depression imposes a frequency dependent filter on synaptic information transfer. *PLoS Computational Biology*, 8:e1002557, 2012.

Rubinov, M. and Sporns, O. Complex network measures of brain connectivity: uses and interpretations. *Neuroimage*, 52(3):1059–1069, 2010.

Sara, Y., Virmani, T., Deák, F., Liu, X., and Kavalali, E. T. An isolated pool of vesicles recycles at rest and drives spontaneous neurotransmission. *Neuron*, 45(4): 563–573, 2005.

Sara, Y., Bal, M., Adachi, M., Monteggia, L. M., and Kavalali, E. T. Use-dependent ampa receptor block reveals segregation of spontaneous and evoked glutamatergic neurotransmission. *Journal of Neuroscience*, 31(14):5378–5382, 2011.

Scott, P., Cowan, A. I., and Stricker, C. Quantifying impacts of short-term plasticity on neuronal information transfer. *Physical Review E*, 85(4):041921, 2012.

Shannon, C. E. A mathematical theory of communication. *Bell System Technical Journal*, 27(4):623666, 1948.

Takumi, Y., Ramírez-León, V., Laake, P., Rinvik, E., and Ottersen, O. P. Different modes of expression of ampa and nmda receptors in hippocampal synapses. *Nature Neuroscience*, 2(7), 1999.

Tang, C.-M., Margulis, M., Shi, Q.-Y., and Fielding, A. Saturation of postsynaptic glutamate receptors after quantal release of transmitter. *Neuron*, 13(6):1385–1393, 1994.

Tarusawa, E., Matsui, K., Budisantoso, T., Molnár, E., Watanabe, M., Matsui, M., Fukazawa, Y., and Shigemoto, R. Input-specific intrasynaptic arrangements of ionotropic glutamate receptors and their impact on postsynaptic responses. *Journal of Neuroscience*, 29(41):12896–12908, 2009.

Telgkamp, P., Padgett, D. E., Ledoux, V. A., Woolley, C. S., and Raman, I. M. Maintenance of high-frequency transmission at purkinje to cerebellar nuclear synapses by spillover from boutons with multiple release sites. *Neuron*, 41(1):113–126, 2004.

Thomson, A. M. and Bannister, A. P. Release-independent depression at pyramidal inputs onto specific cell targets: dual recordings in slices of rat cortex. *The Journal of Physiology*, 519(1):57–70, 1999.

Todorov, E., Siapas, A., Somers, D., and Nelson, S. Modeling visual cortical contrast adaptation effects. In *Computational Neuroscience*, pages 525–531. Springer, 1997.

Tong, G. and Jahr, C. E. Multivesicular release from excitatory synapses of cultured hippocampal neurons. *Neuron*, 12(1):51–59, 1994.

Ulanovsky, N., Las, L., Farkas, D., and Nelken, I. Multiple time scales of adaptation in auditory cortex neurons. *Journal of Neuroscience*, 24(46):10440–10453, 2004.

van Steveninck, R. R. d. R., Lewen, G. D., Strong, S. P., Koberle, R., and Bialek, W. Reproducibility and variability in neural spike trains. *Science*, 275(5307): 1805–1808, 1997.

Vembu, S., Verdù, S., and Steinberg, Y. The source-channel separation theorem revisited. *IEEE Transactions on Information Theory*, 41(1):44–54, 1995.

Ventriglia, F. and Di Maio, V. Effects of ampars trafficking and glutamate-receptors binding probability on stochastic variability of epsc. *Biosystems*, 112(3):298–304, 2013.

Volynski, K. E., Rusakov, D. A., and Kullmann, D. M. Presynaptic fluctuations and release-independent depression. *Nature neuroscience*, 9(9):1091, 2006.

Wadiche, J. I. and Jahr, C. E. Multivesicular release at climbing fiber-purkinje cell synapses. *Neuron*, 32(2):301–313, 2001.

Xu, J. and Wu, L.-G. The decrease in the presynaptic calcium current is a major cause of short-term depression at a calyx-type synapse. *Neuron*, 46(4):633–645, 2005.

Zhai, R. G. and Bellen, H. J. The architecture of the active zone in the presynaptic nerve terminal. *Physiology*, 19(5):262–270, 2004.

Zucchini, W., MacDonald, I. L., and Langrock, R. *Hidden Markov models for time series: an introduction using R*, volume 150. CRC press, 2016.

Zucker, R. S. and Regehr, W. G. Short-term synaptic plasticity. *Annual Review of Physiology*, 64(1):355–405, 2002.

Zuk, O., Kanter, I., and Domany, E. The entropy of a binary hidden markov process. *Journal of Statistical Physics*, 121(3-4):343–360, 2005.

Author Contributions

The author contributions to the papers and the manuscript that were presented in this cumulative thesis are stated in the following:

- M. Salmasi, M. Stemmler, S. Glasauer, A. Loebel, "Information Rate Analysis of a Synaptic Release Site Using a Two-State Model of Short-Term Depression", Neural Computation, 29, 1528-1560, 2017.

  The contributions of the authors Mehrdad Salmasi (MS), Martin B. Stemmler (MBS), Stefan Glasauer (SG) and Alex Loebel (AL) are as follows: MS, MBS, SG and AL designed the study and developed the model. MS analyzed the model and performed the simulations. MS, MBS, SG and AL interpreted the results and wrote the manuscript.

- M. Salmasi, A. Loebel, S. Glasauer, M. Stemmler, "Short-Term Synaptic Depression Can Increase the Rate of Information Transfer at a Release Site", to be submitted.

  The contributions of the authors Mehrdad Salmasi (MS), Alex Loebel (AL), Stefan Glasauer (SG) and, Martin B. Stemmler (MBS) are as follows: MS, AL, SG and MBS designed the study and developed the model. MS analyzed the model and performed the simulations. MS, AL, SG and MBS interpreted the results and wrote the manuscript.

- M. Salmasi, U. Büttner, S. Glasauer, "Fractal Dimension Analysis for Spike Detection in Low SNR Extracellular Signals", Journal of Neural Engineering, 13(3), 36004-36022, 2016.

  The contributions of the authors Mehrdad Salmasi (MS), Ulrich Büttner (UB), and Stefan Glasauer (SG) are as follows: MS, UB and SG designed the study and developed the algorithm. MS analyzed the algorithm and performed the simulations. MS, UB and SG interpreted the results and wrote the manuscript.

We hereby confirm that the information above is correct and accurate.

Munich, 28th September 2017,

Mehrdad Salmasi

Professor Dr. Stefan Glasauer

Eidesstattliche Versicherung/Affidavit

Hiermit versichere ich an Eides statt, dass ich die vorliegende Dissertation “*Information Efficacy of a Dynamic Synapse*” selbstständig angefertigt habe, mich außer der angegebenen keiner weiteren Hilfsmittel bedient und alle Erkenntnisse, die aus dem Schrifttum ganz oder annähernd übernommen sind, als solche kenntlich gemacht und nach ihrer Herkunft unter Bezeichnung der Fundstelle einzeln nachgewiesen habe.

I hereby confirm that the dissertation “*Information Efficacy of a Dynamic Synapse*” is the result of my own work and that I have only used sources or materials listed and specified in the dissertation.

München, den 28 September 2017,
Munich, 28th September 2017,

Mehrdad Salmasi